UNIVERSITY OF CALIFORNIA
Santa Barbara

Development of Electrochemical Techniques for Nanoparticle Characterization and Biosensor Devices

A Dissertation submitted in partial satisfaction
of the requirements for the degree of

Doctor of Philosophy

in

Chemistry

by

Brian Roehrich

Committee in Charge:

Professor Lior Sepunaru, Chair

Professor Thuc-Quyen Nguyen

Professor Craig Hawker

Professor Raphaële Clement

September 2024

The Dissertation of
Brian Roehrich is approved:

Professor Thuc-Quyen Nguyen

Professor Craig Hawker

Professor Raphaële Clement

Professor Lior Sepunaru, Committee Chairperson

July 2024

Development of Electrochemical Techniques for Nanoparticle Characterization and Biosensor Devices

by

Brian Roehrich

Acknowledgements

First and foremost, I would like to thank Lior for being an outstanding mentor over these past five years. I really appreciate the guidance and direction you gave my projects while still allowing me to pursue my interests – even when I (occasionally) pushed back on your suggestions. I would also like to thank Professor Kevin Plaxco for facilitating an excellent and fruitful collaboration, which exposed me to a whole field of electrochemistry I would have never imagined at the start of my PhD. I would also like to thank my committee members, Professors Thuc-Quyen Nguyen, Raphaële Clement, and Craig Hawker. Each of you has given me very valuable advice over the course of my PhD which shaped its direction as well as my future goals. Thanks to everyone at Aptitude (especially Sheng-Ping for making the connection) as well, I learned a ton during my time there and really appreciated being a valued part of the team.

To everyone in the Sepunaru lab, you have all been great coworkers and friends over the past few years. I will truly miss our post-group meeting coffee runs (even if I won't miss all of the group meetings...) as well as all the other fun times we've had in lab, around Santa Barbara, and on vacations ("conferences"). Attending Pacifichem, ECS, and GRC were three of the big highlights of my time in grad school. Aside from those, I've had a great time riding bikes, hiking, camping, running, climbing, skiing, playing board games, and so much more with all of the great friends I've met in and out (but mostly in) of grad school. I feel I've made the most of my time in Santa Barbara, in no small part because of all of you.

Thanks to my family for their support throughout grad school, and thanks to Phoebe for being a wonderful partner and companion. You have made the last five years very special and I'm really looking forward to what comes next! Finally, I would like to thank our cat, Fig, who provides me intermittent affection and constant, mild, allergies.

Curriculum Vitæ

Brian Roehrich

Education

2024	Doctor of Philosophy in Chemistry University of California, Santa Barbara (Expected).
2019	Bachelor of Science in Chemistry University of California, Davis.

Professional Appointments

2019 – 2024	Graduate Research Fellow University of California, Santa Barbara.
2022 – 2023	Associate Scientist (Intern) Aptitude Medical Systems, Goleta, CA.
2016 – 2019	Undergraduate Research Assistance University of California, Davis.

Awards

2021	Graduate Research Fellowship, National Science Foundation.
2019	Departmental Citation for Outstanding Graduating Senior, University of California, Davis.
2018	Best Presentation in Physical/Analytical Chemistry, Richard Larock Conference.
2015	James and Leta Fulmor Scholarship, University of California, Davis.

Publications

1. Roehrich, B.; Sepunaru, L. Impedimetric Measurement of Exchange Currents and Ionic Diffusion Coefficients in Individual Pseudocapacitive Nanoparticles. *ACS Meas. Sci. Au* **2024**, 10.1021/acsmeasuresciau.4c00017.
2. Albanese, K.R.; Morris, P.T.; Roehrich, B., Read de Alaniz, J., Hawker, C.J., Bates, C.M. Selective Electrochemical Degradation of Bottlebrush Elastomers. *J. Polym. Sci.* **2024**, 10.1002/pol.20240393.
3. Liu, E. Z.; Rivalta Popescu, S.; Eden, A.; Chung, J.; Roehrich, B.; Sepunaru, L. The Role of Applied Potential on Particle Sizing Precision in Single-Entity Blocking Electrochemistry. *Electrochim. Acta* **2023**, 472 (October), 143397.

4. Roehrich, B.;† Leung, K. K.;† Gerson, J.; Kippin, T. E.; Plaxco, K. W.; Sepunaru, L. Calibration-Free, Seconds-Resolved In Vivo Molecular Measurements Using Fourier-Transform Impedance Spectroscopy Interrogation of Electrochemical Aptamer Sensors. *ACS Sens.* **2023**, 8 (8), 3051–3059.
5. Leung, K. K.; Gerson, J.; Emmons, N.; Roehrich, B.; Verrinder, E.; Fetter, L. C.; Kippin, T. E.; Plaxco, K. W. A Tight Squeeze: Geometric Effects on the Performance of Three-Electrode Electrochemical-Aptamer Based Sensors in Constrained, in Vivo Placements. *Analyst* **2023**, 148 (7), 1562–1569.
6. Quek, G.; Roehrich, B.; Su, Y.; Sepunaru, L.; Bazan, G. C. Conjugated Polyelectrolytes: Underexplored Materials for Pseudocapacitive Energy Storage. *Adv. Mater.* **2022**, 34 (22), 2104206.
7. Roehrich, B.; Liu, E. Z.; Silverstein, R.; Sepunaru, L. Detection and Characterization of Single Particles by Electrochemical Impedance Spectroscopy. *J. Phys. Chem. Lett.* **2021**, 12 (40), 9748–9753.
8. Roehrich, B.; Sepunaru, L. Nanoimpacts at Active and Partially Active Electrodes: Insights and Limitations. *Angew. Chemie Int. Ed.* **2020**, 59 (43), 19184–19192.
9. Roehrich, B. W.; Han, R.; Osterloh, F. E. Hydrogen Evolution with Fluorescein-Sensitized $Pt/SrTiO_3$ Nanocrystal Photocatalysts Is Limited by Dye Adsorption and Regeneration. *J. Photochem. Photobiol. A Chem.* **2020**, 400, 112705.

Presentations

1. Interrogation of Electrochemical Aptamer-Based Biosensors via Electrochemical Impedance Spectroscopy. Jan. 6, 2024, *Gordon Research Seminar (Electrochemistry)*, Ventura, CA.
2. Interrogation of Electrochemical Aptamer-Based Biosensors via Electrochemical Impedance Spectroscopy. Feb. 8, 2023, *Center for Polymers and Organic Solids Seminar*, Santa Barbara, CA.
3. Characterization of Single Particles by Electrochemical Impedance. May 31, 2022, 241^{st} *Meeting of the Electrochemical Society*, Vancouver, BC.
4. Characterizing Single Particles and Biosensors via Electrochemical Impedance. Mar. 9, 2022, *Center for Polymers and Organic Solids Seminar*, Santa Barbara, CA.
5. Characterization of Single Nanoparticles using Impedance Spectroscopy. Dec. 20, 2021, *Pacifichem*, Honolulu, HI.
6. Studying Electrochemical Properties of Individual Nanoparticles. Feb. 3, 2021, *Center for Polymers and Organic Solids Seminar*, Santa Barbara, CA.
7. Insights from Nano-Impacts at Partially Active Electrodes. Nov. 23, 2020, $ElecNano^9$ *– Electrochemistry in Nanoscience.* Paris, FR.

8. Studying Electrocatalytic Mechanisms via Nano-Impacts. May 7, 2020. *UCSB Catalysis Seminar Series*, Santa Barbara, CA.

Field of Study: Electrochemistry

Abstract

Development of Electrochemical Techniques for Nanoparticle Characterization and Biosensor Devices

by

Brian Roehrich

Electrochemistry is the study of the interface between chemical species and electrified surfaces. These interfaces, which use electrical current to drive chemical transformations or derive electrical energy from chemical reactions, are critically important in the context of climate change. Using electrochemistry, renewably-generated electricity can be stored in the form of chemical potential in the chemical bonds of a fuel (such as hydrogen) or in the energy of electrons in a battery. These reactions are often catalyzed by nanoparticles of various materials, chosen due to their high surface areas and ostensibly tunable proparties. However, a significant gap in our understanding of these nanoparticles remains: as nanoparticles are not atomically precise, each individual particle has different properties (e.g., size, shape, or catalytic performance). However, conventional analysis methods study ensembles of many particles and cannot deconvolute each individual's contribution. This means that the best-performing particles (compared to those which contributed little to the reaction) cannot be readily identified, and future syntheses cannot be tailored to target these particles.

The first three chapters of this dissertation describe my work to develop new methods and tools to study individual particles at the nanoscale, one particle at a time. First, I describe our efforts to understand the reactivity of platinum nanoparticles which catalyze the hydrogen evolution and oxygen reduction reactions. The broad distribution of catalytic activities we measured could not be explained simply by particle size, and our insights let us identify a possible mechanism degraded the particles' activity. In order to glean more information from each particle, I next developed a method to measure the electrochemical impedance of single nanoparticles. Electrochemical impedance spectroscopy has the ability to resolve different interfacial processes based on their timescales and was used to detect individual, insulating microparticles as they collided with an electrode; the time-resolved impedance spectra enabled accurate measurement of the particle-electrode contact areas. Finally, the single-particle impedance technique was applied to individual Prussian blue nanocubes, which reversibly intercalate sodium ions. In this case, spatially-resolved impedance spectra allowed us to measure the ionic and electronic conductivities of the particles as they stored sodium ions and electrons and revealed that these conductivities varied by up to an order of magnitude particle-to-particle.

The final chapter of this work extends the time-resolved impedance techniques developed for single particle analysis to the field of electrochemical biosensing. Biosensors aim to measure the presence or concentration of a particular species, and electrochemistry provides a natural way to translate between a chemical species and an electrical signal. Specifically, I describe the interrogation of a class of devices known as electrochemical

aptamer-based sensors using electrochemical impedance spectroscopy. This technique enabled us to measure the state of the sensors more precisely and more rapidly than comparable methods, allowing real-time measurements of an antibiotic and an amino acid, even in the blood stream of living animals.

Table of Contents

List of Figures

List of Tables

Chapter 1

Introduction

1.1 Why Electrochemistry?

The annals of electrochemistry date back to the 1780, when Luigi Galvani discovered "animal electricity" by coercing frogs' legs to twitch using two metal wires.[1] In fact, he had created a one of the first artificial electrochemical cells – the two different metals he used formed a circuit that spontaneously discharged across the frogs' legs (which moved as a side effect).[1] The physics explaining this experiment (amongst others) were finally established by Rudolph Marcus in 1956, who was later awarded the Nobel Prize in Chemistry for his eponymous theory of electron transfer reactions.[2] In the decades since, electrochemists have – to varying degrees of success – studied, applied and exploited the phenomena of electrochemistry in attempts to solve great societal challenges.

Fundamentally, electrochemistry deals with the interactions between electricity and chemical species. Electricity can be used to drive chemical reactions: – two conductive pieces of metal ("electrodes") can reduce and oxidize water to form hydrogen and oxygen,

respectively, if an appropriate voltage is applied between them. Conversely, chemical reactions can be used to generate electricity – if hydrogen and oxygen are introduced to a device which respectively oxidizes and reduces them, water and electrical power are produced. For these reasons, electrochemistry forms the heart of many of the technologies which enable the transition to renewable energy. Electrical energy, generated from wind or solar power, can be stored as chemical potential during peak power generation hours and reclaimed when needed later. Batteries, supercapacitors, and electrolyzers are just three examples of devices which rely on electrochemistry to store power.[3] Electrochemistry can be used to drive synthetic reactions, replacing toxic or fossil fuel-derived reagents with renewably-generated electrons.[4] Finally, the direct link electrochemistry provides between chemical species and electrical signal can be used to construct sensors which readily or quantify specific molecules - these devices will be discussed in further detail later in this chapter.[5]

The principles of electrochemistry are well described by many textbooks and will not be covered here, the interested reader is invited to consult Compton and Banks[6] or Bard and Faulkner,[7] amongst others. To introduce the topics discussed in this thesis, however, consider the electrolysis of water:

$$2H_2O \longrightarrow 2H_2 + O_2$$

This reaction is thermodynamically unfavorable ($\Delta G = 237kJ/mol$). Yet, it can be driven electrochemically by reducing water to form hydrogen at one electrode (the

cathode) and oxidizing water (or hydroxide) to form oxygen at a second electrode (the *anode*):

$$4H_2O + 4e^- \longrightarrow 2H_2 + 4OH^-$$

$$4OH^- \longrightarrow O_2 + 2H_2O + 4e^-$$

The potential needed to drive an electrochemical reaction is determined by its thermodynamics ($E^\circ = \frac{-\Delta G}{nF}$ where E° is the potential under standard conditions, n is the number of electrons transferred in the reaction, and $F = 96485\ C\ mol^{-1}$ is Faraday's constant. For the above reaction, $E^\circ = 1.23\ V$).[7] In practice, additional driving force (overpotential) is needed for the reaction to proceed at a desirable rate. Indeed, the current which flows through an electrochemical cell strongly depends on the potential applied across the cell. Fundamentally, this is because the activation energy barrier (which dictates the kinetics) of electron-transfer reactions scales with the difference in free energy between the reactant and product states.[2] This relationship, which is unique to electron-transfer reactions, means that the rate of an electrochemical reaction can be increased by making the reaction more thermodynamically favorable – conveniently, this can be achieved by simply applying a larger potential across the electrochemical cell.

However the scaling between reaction thermodynamics and kinetics is not always straightforward. While some simple electron-transfer reactions are agnostic towards the electrode which catalyzes them (outer sphere reactions), most energy-relevant reactions involve multiple electron-transfer and chemical reaction steps and feature intermediates bound to the electrode surface – electrodes made of certain materials are much more

effective catalysts of these reactions than a generic conductive metal would be.[7] Characterizing the performance of such materials is even more complicated because many electrocatalysts are comprised of nanoparticles[1] to maximize their specific surface area.[8] Critically and unlike molecules, these species are not atomically precise: two nanoparticles with the same elemental composition may adopt different morphologies, and thus, have different physical properties.[9] Ensemble measurements of a bulk electrode mask these particle-to-particle differences, and so features which give rise to the best electrode performance[2] may be hidden if they only occur in a small fraction of particles.

Single-entity electrochemistry seeks to unmask these differences by measuring the properties of individual nanoparticles, one at a time. Ultimately, this approach aims to quantify the differences between individual particles and identify the best-performing particles so that syntheses can be tuned to produce them, improving the efficiency of the entire ensemble. The bulk of this dissertation is devoted towards developing methods to measure the properties of individual nanoparticles.

[1] Solids which have at least one dimension with a length in the scale of nanometers.
[2] For example, activity, selectivity, or durability

1.2 Electrochemical Characterization of Single Nanoparticles

1.2.1 Introduction

Nanoparticles are ubiquitous in electrochemistry because they have extremely high specific surface areas and electrochemical reactions occur at the solid-liquid interface. The easiest way to increase the amount of product produced by an electrochemical reaction is to simply increase the surface area of the electrode.[3] However, the heterogenous nature of nanoparticles makes it difficult to analyze their properties based solely on bulk, ensemble measurements. In the following sections, I will briefly review existing electrochemical methods to detect and characterize individual nanoparticles.

1.2.2 Electrochemical Characterization of Individual Particles in Suspensions

The first prominent example of the electrochemical detection of single particles is the Coulter counter.[10] Invented in 1953, this device measures the ionic current between two reservoirs separated by a narrow channel. When a single particle passes through the channel, a discrete decrease in the current can be measured and used to estimate the size of the particle. While the Coulter counter still finds widespread use in cell counting (for

[3]Provided that the concentration of reactants in solution and their mass transport rates to the electrode are high enough that the reaction is not limited by diffusion.

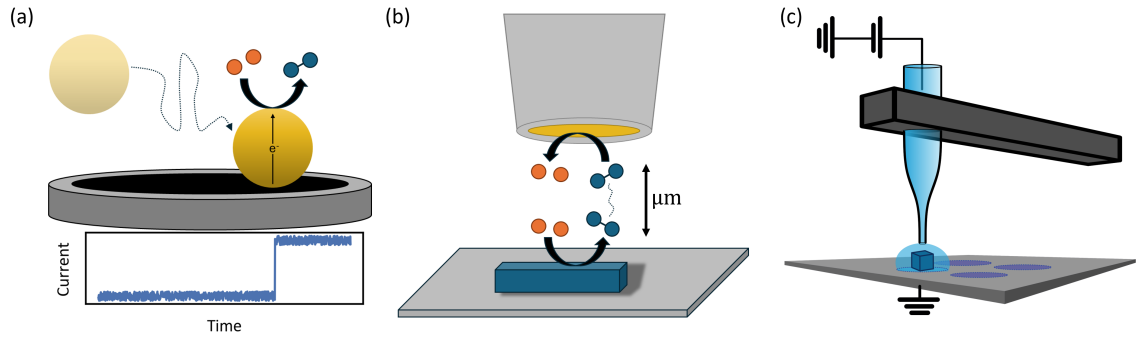

Figure 1.1: Three methods which enable electrochemical measurements of single nanoparticles. (a) The nano-impact method relies on a particle in solution stochastically colliding with a microelectrode. When in contact with the electrode, the particle catalyzes and electrochemical reaction and the resulting change in current informs on the catalytic properties of that particular nanoparticle. (b) Using scanning electrochemical microscopy, a microelectrode collects (oxidizes or reduces) the product of the electrochemical reaction occuring on an isolated, surface-bound particle. (c) The droplet used in scanning electrochemical cell microscopy can be used to isolate a single nanoparticle on the surface, forming a microscopic electrochemical cell which can be interrogated using conventional electrochemical techniques.

example, for blood counting in hospitals) and related particle sizing methods continue to attract research interest,[11, 12] insights beyond simply measuring the size of the particle require other electrochemical methods. One such method is the "nano-impact" technique, which examines the response of an electrode when individual particles stochastically collide with it. Early observations of current transients associated with particle collisions were reported by Micka[13] as well as Jones and Kaye[14]; recent interest in using such transients for single-particle analysis was driven by the 2007 report by Xiao and Bard who suggested that each transient would inform on the electrocatalytic properties of the individual nanoparticles.[15] In nano-impact measurements (Figure 1.1a), an ultramicroelectrode[4] which is a poor catalyst of the reaction of interest is immersed in a solution

[4]Typically a disk electrode with a radius between 1 and 10 μm.

that contains a low concentration of catalytic particles. A potential is applied to the electrode, chosen such that no reaction occurs on the bare electrode. As a particle diffuses through solution, it may randomly collide with the electrode and form an ohmic contact with the surface, adopting the electrode's potential. If this potential is sufficient to drive the electrochemical reaction on the particle, a discrete increase in current through the electrode is measured and can be correlated to that single particle.[16] Using this measurement technique, individual particles can be detected and their catalytic properties (relating to the size, shape, and duration of the current transient) can be examined.

The nano-impact technique has applied to a wide range of electrocatalytic nanomaterials in the past 15 years, as has been reviewed elsewhere.[17–19] However, the technique has several limitations which lower its potential. Most glaringly, despite measuring the response of a single particle, the stochastic nature of the technique makes it extremely difficult to identify *which specific* particle produced a particular electrochemical response. Nano-impact experiments typically collect many particles on the electrode surface, recording many current transients.[5] This makes it extremely difficult to link a particular particle to a particular current transient, which would be necessary to identify features of desirable particles. The depth of electrochemical characterization possible on a single particle is also limited – the vast majority of studies rely on chronoamperometry [20] (applying a constant potential and measuring current) which does not yield the thermodynamic or kinetic information offered by voltametry or impedance spectroscopy.[6]

[5] Additionally, in some cases, particles may desorb from the surface and return to solution.

[6] Several authors have reported measurements of single particles using, for example, fast-scan cyclic voltammetry[21] or impedance spectroscopy.[22]

Finally, rather than solely informing on the electrochemical reaction, the observed current transients are often convoluted by a variable particle-electrode contact[23] or even the electronics used to measure them.[24]

1.2.3 Electrochemical Characterization of Individual, Surface-Immobilized Particles

In contrast to the transient, stochastic nature of nano-impact experiments, single-particle studies can also be carried out by fabricating an electrode whose electroactive surface consists of a single particle. At the nanoscale, this has been accomplished by using a molecular linker to bind a single gold nanoparticle to the surface of a platinum nanoelectrode.[25] Because the size of the particle (15 nm) was commiserate with that of the electrode (10 nm) and the electrode had been passivated with a silane layer, the voltammetric response of the electrode was dictated by the properties of the single nanoparticle rather than the supporting electrode. However, the extreme difficulty of fabricating nanometer-scale electrodes and isolating single nanoparticles on them makes this method unfeasible for larger-scale studies.

Scanning probe techniques such as scanning electrochemical microscopy (SECM) can also be used to elucidate the electrochemical response of individual, electroactive nanoparticles. Single particle measurements are be performed in an SECM by immobilizing the particles on a conductive substrate which serves as a working electrode. A potential is applied so the particles catalyze an electrochemical reaction, a micro- or nanoelectrode

probe is positioned near the surface using piezoelectric positioners, and the probe is moved across the surface to scan a particular region. The probe can identify a particle on the surface by detecting the product of the reaction catalyzed on the particle's surface (Figure 1.1b). This approach offers unparalleled spatial resolution into the catalytic performance of a nanoparticle.[26] Collecting the reaction product on the SECM probe also enables selectivity in the measurement, as the probe potential can be tuned to only react with certain species.[27]

Scanning electrochemical cell microscopy (SECCM) is perhaps the most elegant method to accomplish single-particle measurements. While named similarly to the aforementioned SECM, SECCM operates by a very different modality: the probe in an SECCM experiment is an electrolyte-filled micro- or nanopipette which is equipped with a counter electrode and positioned near a conductive surface (the working electrode). A potential is applied across the two electrodes and the pipette is slowly lowered towards the substrate until its electrolyte wets the surface and current flows across the interface. This forms a microscopic droplet of solvent between the pipette and the substrate, and any electrochemical response measured is entirely attributable to that miniscule region of the substrate (Figure 1.1c).[28] For single particle studies, the SECCM pipette can be used to isolate individual nanoparticles (which were deposited onto the substrate prior to the experiment) within the droplet in order to probe their properties. The SECCM experiment is simple to set up, can interrogate many individual particles in a single experiment,[9] and the probe fabrication and experimental conditions are

highly adaptable with even measurements in inert atmospheres possible.[29] After the experiment, the *exact same* particles can be visualized by microscopy or analyzed by other co-localized techniques (*vide infra*).[30] Recent work has even introduced the chemical selectivity of SECM measurements by using dual-barrel pipettes.[31] Taken together, these capabilities make SECCM a natural and effective technique for single-entity electrochemistry.

1.2.4 Indirect Methods for Characterizing Individual, Electroactive Nanoparticles

Rather than directly measuring an electrochemical response, the presence and characteristics of single particles can be elucidated indirectly by optical methods. One approach leverages electrochemiluminescence, in which the product of an electrochemical reaction reacts with a sacrificial reagent to generate light. Modern cameras can be sensitive enough to detect single photons, giving this approach an ultrasensitive limit of detection. It has been coupled with nano-impact electrochemistry to detect individual particles,[32] and applied to surface-bound nanoparticles to study plasmonic effects.[33] A major limitation, however, is that the electrochemical reaction must generate a luminescent species. A more generally applicable approach is to monitor the change in optical properties of single particles in response to a changes in potential.[34] For example, the transmittance of many ion-intercalating materials changes significantly with the extent of intercala-

tion. Optical microscopy can track these changes at the single-particle level, yielding information on charging rates and capabilities with implications for ion batteries.[35]

1.2.5 Correlative Methods

Lastly, a growing push in single-particle electrochemistry is to correlate electrochemical and non-electrochemical measurements performed on *the same* particle, with the goal of uncovering structure-property relationships. This trend has largely been driven by two rapidly developing techniques: scanning electrochemical cell microscopy (SECCM) and liquid-phase transmission electron microscopy (TEM).

As discussed above, SECCM studies use the instrument's scanning droplet to isolate a small region of a surface. The droplet leaves behind a small residue of electrolyte at each location it contacts the surface, which, after the experiment, can be located by microscopy. For single-particle studies, the exact particle which produced a certain electrochemical response can be located. The particle morphology can be characterized by scanning or transmission electron microscopy (SEM or TEM) or atomic force microscopy (AFM), and further insights on the composition and structure of the particle can be gleaned from in-microscope techniques such as energy dispersive X-ray spectroscopy or electron diffraction.[36] Correlative methods in SECCM is an active area of research, with new methods using mass spectrometry and on TEM grids promising unprecedented insights at the single-particle level.[37, 38]

Finally, emerging techniques may allow for the *in-situ* measurement of the electrochemical and physical properties of a single nanoparticle. Using liquid cell transmission electron microscopy, particles of interest can be imaged by an electron beam while immersed in a liquid environment and undergoing concurrent electrochemical measurements. Such an approach allows observation of the dynamics of a material during an electrochemical reaction, for example, characterizing the structural changes a catalyst undergoes during electrolysis.[39] While major technical limitations remain to be overcome,[40] these measurements represent the ultimate frontier in single-entity electrochemistry.

1.3 Electrochemical Impedance Spectroscopy

1.3.1 Introduction

While most single-entity electrochemistry experiments rely on voltammetry, Chapters 3 and 4 of this thesis focus on developing single-entity methods based on electrochemical impedance spectroscopy. Electrochemical impedance spectroscopy (EIS) is a powerful electroanalytical technique which measures frequency-dependent response of an electrochemical cell. This frequency-dependent response can be used to unravel the (normally convoluted) interfacial processes which occur in the electrochemical cell – for example, the rapid charging of the electrochemical double layer (which occurs at short timescales and thus, high frequencies) can be studied independently of more sluggish mass transport (which can be probed at low frequencies). Impedance spectroscopy has widespread application in electrochemistry, including the elucidation of electrochemical reaction mechanisms and the characterization of batteries and electrolyzers.[41]

1.3.2 Principles of EIS

Impedance is the frequency-dependent analogue of resistance. It is defined by Equation 1.1, where $Z(\omega)$, $V(\omega)$, and $I(\omega)$ are the impedance, voltage, and current at a particular frequency ω. Perturbation of an electrochemical cell with a sinusoidal voltage given by Equation 1.2 will give rise to an oscillating current with a current magnitude

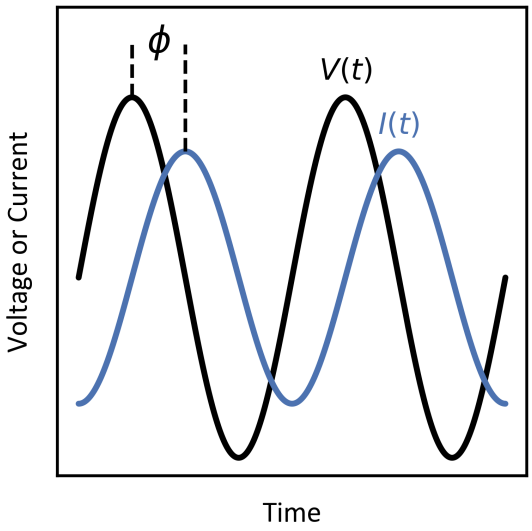

Figure 1.2: The current produced by a linear electrochemical cell in response to a sinusoidal voltage perturbation is a phase-shifted sine wave.

given by $|I| = \frac{|Z|}{|V|}$ and a phase shift ϕ (which quantifies the "delay" between the two sine waves) as shown in Figure 1.2.

$$Z(\omega) = \frac{V(\omega)}{I(\omega)} \tag{1.1}$$

$$V = V_0 \sin(\omega t) \tag{1.2}$$

$$I = I_0 \sin(\omega t + \phi) \tag{1.3}$$

Using Euler's formula,

$$Z(\omega) = \frac{V_0 \sin(\omega t)}{I_0 \sin(\omega t + \phi)} = \frac{V_0 e^{i\omega t}}{I_0 e^{i(\omega t + \phi)}} \tag{1.4}$$

$$Z(\omega) = |Z| e^{-i\phi} = |Z|(\cos\phi + i sin\phi) \tag{1.5}$$

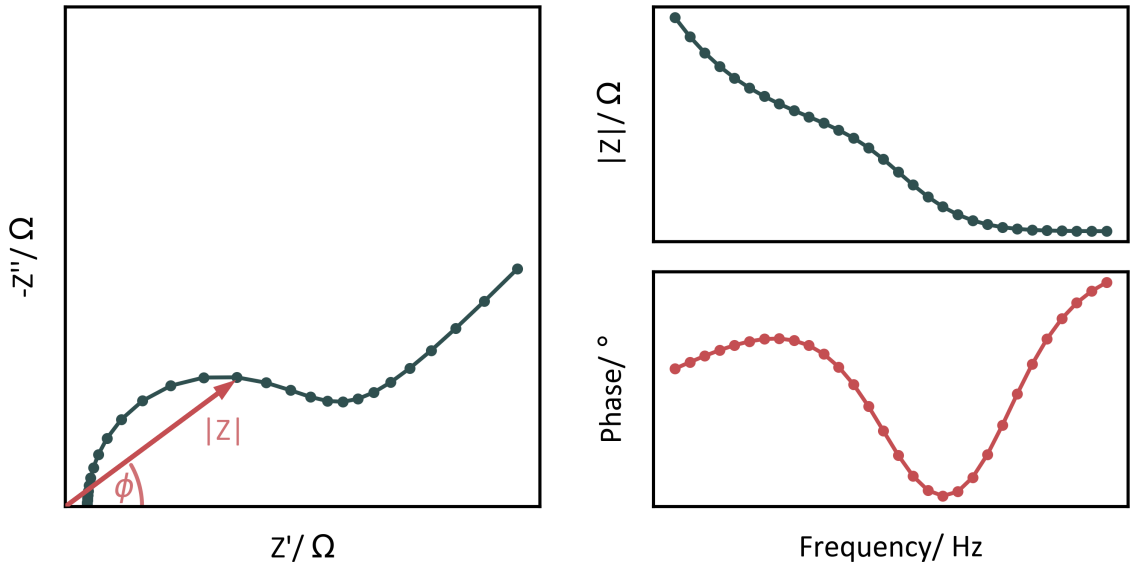

Figure 1.3: Impedance spectra can be represented on the complex plane as Nyquist plots (left) or plotted against frequency to form Bode plots (right).

Impedance spectra are commonly represented on the complex plane as Nyquist plots, where the magnitude ($|Z|$) and phase (ϕ) of the impedance at a certain frequency describe the vector from the origin. The frequency of each data point is not explicit in a Nyquist plot, however, for electrochemical cells, the high-frequency impedance is nearly always smaller than the low-frequency impedance. Alternatively, the magnitude and phase of the impedance can be plotted against frequency to form a Bode plot. Both representations of the impedance are shown in Figure 1.3 and will be used interchangeably throughout this dissertation.

The frequency-dependent response of an electrochemical impedance spectrum can be analyzed in terms of an electronic circuit model.[7] For example, the electrochemical dou-

[7]Critically, all electronic circuit elements must have a clear physical meaning in terms of the electrochemical phenomena at play for this approach to have any validity. Fitting can always be performed to large, arbitrary, but ultimately meaningless models.

ble layer forms when a charged electrode contacts an electrolyte solution.[8] Ions of the opposite charge are attracted to the electrode and, to a first approximation, this association of opposite charges is analogous to a parallel-plate capacitor. Remarkably, the electrochemical double layer behaves as a nearly ideal capacitor in many cases.[7] Likewise, the energetic barrier which must be overcome to drive an electron-transfer reaction is analogous to a resistor, with the kinetics of the electrochemical reaction dictating the magnitude of the resistance.[7] Because capacitance depends on frequency (Equation 1.6) while resistance does not (Equation 1.7), the frequency-dependent response of the cell can be used to deconvolute these two electrochemical phenomenon from one another.[7] Equivalent circuit elements can be added in series and in parallel to one another in order to build increasingly complex models of realistic electrified interfaces – several models for common electrochemical cells, and the impedance spectra they describe, are shown in Figure 1.4.

$$Z_C = \frac{1}{i\omega C} \tag{1.6}$$

$$Z_R = R \tag{1.7}$$

Some electrochemical phenomena do not have direct analogues to electronic circuit elements. For example, the constant phase element (CPE) is commonly used as an

[8]The charges surface attracts a strongly adsorbed layer of ions, known as the Helmholtz layer. This high concentration of a single (i.e., positive) charge very close to the electrode surface necessitates a balancing layer of the opposite (negative) charge, which attracts a layer of the original (positive) charge, and so on. Layers of charges become increasingly diffuse as the distance to the electrode grows, and are described by theories such as the Gouy-Chapman-Stern model.[7]

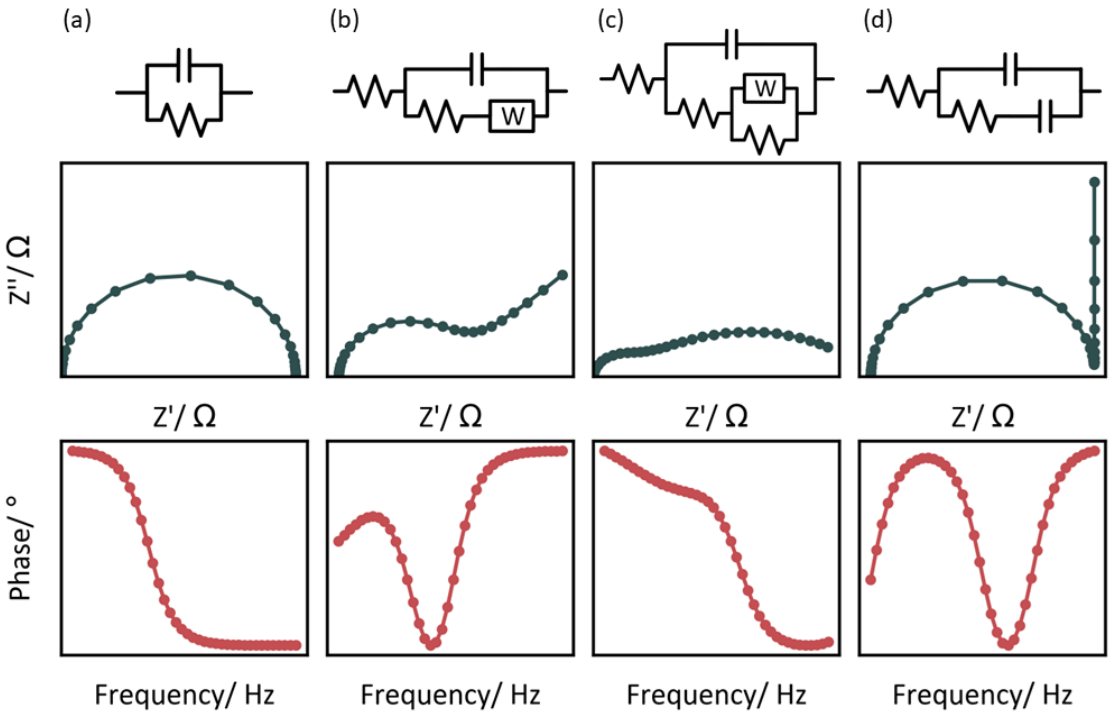

Figure 1.4: Characteristic impedance spectra produced by the equivalent circuits used to represent (a) a simple charge-transfer reaction and double layer capacitance, (b) a charge-transfer reaction with semi-infinite linear diffusion (as to a macroscopic disc electrode), (c) a charge-transfer reaction in the presence of hemispherical diffusion (as to a disc ultramicroelectrode), and (d) a charge-transfer reaction to a surface-bound redox species. In these schematics, "W" indicates the Warburg diffusion impedance.[42]

empirical model of non-ideal capacitance. While its origins remain a continuous source of debate,[43] it is used to account for the distribution of capacitances and associated energy losses at electrochemical interfaces. Mathematically, it is described as,[43]

$$Z_{CPE} = \frac{1}{(i\omega)^{\alpha}Q} \tag{1.8}$$

where α represents the phase of the CPE ($\phi_{CPE} = 90^{\circ} \times \alpha$) and Q is its magnitude.

Similarly, diffusion has no clear electrical circuit analogue yet plays a critical role in electrochemistry and must be accounted for in impedance models. In the case of a macroscopic disc electrode, the diffusion layer grows grows continuously with time[9] and the Faradaic current decays towards zero at long experimental times – the volume near the electrode surface becomes increasingly depleted of analyte.[7] Zero current at $t = \infty$ implies that $|Z| \longrightarrow \infty$ as $\omega \longrightarrow 0$. Indeed, the impedance of a macroscopic electrode catalyzing a simple electrochemical reaction trends towards large $|Z|$ and a 45° phase at low frequencies as shown in Figure 1.4b. This behavior can be derived directly from Fick's laws as originally shown by Warburg and Randles,[42, 44] for whom the respective diffusion model and net equivalent circuit are named. In some cases, simple, approximate models can be preferred over the analytical solution in order to simplify the interpretation of impedance data. For example, the analytical solution for the diffusional impedance of an ultramicroelectrode is known but .[45] An approximation consisting of the Warburg impedance in parallel with a resistor, while imprecise, captures the same features of

[9] More precisely, the flux of redox species to the electrode is proportional to $1/\sqrt{t}$.

the impedance spectrum and can enable the interpretation of the ultramicroelectrode impedance.[10][46]

1.3.3 Experimental Considerations for Impedance Measurements

All impedance data must satisfy several criteria:[41, 47]

(i) **Linearity**. The input (voltage) and output (current) must be linearly proportional to one another. This is not generally true for electrochemical systems, however, electrochemical interfaces are approximately linear across small voltage ranges. Because of this, EIS is typically measured by applying small (tens of millivolts) AC voltage perturbations. Within the linear regime, the measured impedance is independent of the applied AC voltage.

(ii) **Causality**. The output (current) is entirely caused by the input (voltage). This condition may not be met if, for example, a temperature increase causes a change in current which was not caused by the voltage perturbation.

(iii) **Stability**. The state of the system must not vary over time independently of the applied perturbation. Repeated measurements of a stable system will yield identical impedance spectra.

[10] At an ultramicroelectrode, $I \longrightarrow i_{ss}$ as $t \longrightarrow \infty$. Thus, in the associated impedance spectrum, $|Z| \longrightarrow Z_0$ as $\omega \longrightarrow 0$, where Z_0 is a constant (real) value proportional to $1/i_{ss}$.

Impedance spectra are typically measured using a frequency response analyzer (FRA).[11] A sinusoidal voltage of a set frequency is applied to the electrochemical cell, and the current response is recorded. To build a complete impedance spectrum, the responses at many different frequencies (often spanning mHz to tens or hundreds of kHz) are recorded sequentially. With this approach, filters, sampling rates, and signal integration strategies can be optimized for each individual frequency in order to maximize signal and minimize noise. However, long measurement durations and susceptibility to system instability are two key disadvantages of FRA measurements.

A multi-frequency perturbation can surpass these limitations. This approach, known as Fourier-transform EIS (FT-EIS), was introduced by Popkirov and Schindler with the goal of significantly shortening the measurement time of a single impedance spectrum and enabling time-resolved impedance spectroscopy.[48] In FT-EIS, the perturbation voltage is a summation of sine waves at the N different frequencies to be interrogated, such that,

$$v(t) = \sum_{j}^{N} v_j \sin\left(\omega_j t + \Phi_j\right) \tag{1.9}$$

where the phase Φ_j of each sine wave is either optimized to minimize constructive interference between different frequencies, or simply randomized.[49] If the electrochemical cell responds linearly to each frequency, the current response is given by,

$$i(t) = \sum_{j}^{N} i_j \sin\left(\omega_j t + \phi_j\right) \tag{1.10}$$

[11] Modern potentiostats calculate the impedance digitally by Fourier transforming the recorded voltage and current rather than incorporating a lock-in amplifier.

The impedance is then calculated by Fourier transforming the recorded voltage and current. As both the voltage and current contain all of the frequencies of interest, the full impedance spectrum is obtained in a single measurement. Using this technique, a spectrum can be measured in the time needed to measure its lowest frequency ($t_{spectrum} = 1/f_{min}$).

While FT-EIS can significantly shorten the time required for an impedance measurement, the technique comes with several drawbacks and necessary considerations before a measurement can be made. For example, the widest frequency range feasible in a FT-EIS measurement is limited compared to an FRA measurement. This is because a single bandwidth and amplifier gain must be used to measure the whole frequency spectrum in the FT measurement – choice of appropriate measurement conditions which capture both very large currents at high frequencies and very low currents at low frequencies can be unfeasible. This limitation can be partially mitigated via optimization of the perturbation voltage. If a relatively higher voltage is applied at low frequencies (which produce a small current response) than at high frequencies, the output current is similar at each measured frequency.[49] As in FRA measurements, nonlinear current-voltage characteristics must be avoided in FT-EIS. This is made more difficult, however, due to the possibility of constructive interference between sine waves of different frequencies. To minimize the chance of a nonlinear response, the phase of each sine wave in the FT-EIS voltage perturbation are chosen to minimize constructive interference, 2^{nd} harmonics of each frequency are avoided, and the waveform is scaled to have a small peak-to-peak

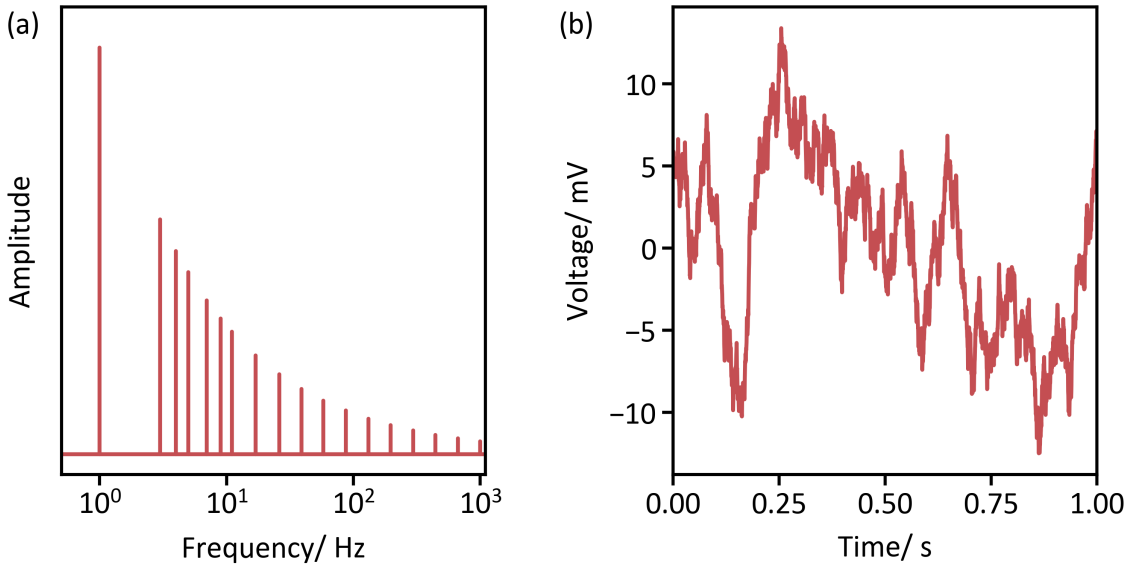

Figure 1.5: Example of a typical waveform used as a voltage perturbation in FT-EIS in the (a) frequency and (b) time domains.

amplitude in the time domain.[49] An example of an appropriate waveform for FT-EIS measurements is shown in Figure 1.5

1.4 Electrochemical Biosensing

1.4.1 Introduction

Biosensors are devices which detect or quantify specific molecular species in complex media. They do this by linking a biological recognition element (for example, an enzyme) with a signal transduction element which produces a quantifiable output signal. Electrochemistry is an excellent signal transducer in this context due to the direct link it provides between chemical species and electrical currents.[5]

To date, the most prevalent and successful example of an electrochemical biosensor is the glucose sensor.[50] These devices typically rely on the enzyme glucose oxidase, which catalyzes the oxidation of glucose in the presence of an electron acceptor (oxygen or an oxidized redox mediator such as the ferrocinium cation). The reduced product of this reaction (hydrogen peroxide or ferrocene, respectively) is quantified electrochemically and used to determine the concentration of glucose in the sample. Based on this technology, continuous, real-time glucose monitors have been commercially available since 2000 and have revolutionized our understanding and treatment of diabetes.[51]

Electrochemical biosensors can similarly enable therapeutic drug monitoring for non-glucose targets. Real-time monitoring is highly desirable for drugs such as antibiotics and chemotherapeutics which have a narrow therapeutic range, highly individual pharmacokinetics, or known adverse effects as it can enable patient-specific dosing regimes.[52] However, the reaction scheme which underlies electrochemical glucose sensors is not gen-

eralizable to many target molecules. This is because it relies on glucose oxidase, which serves two critical functions: (i) selective recognition of the target molecule and (ii) rapid conversion of the target molecule into an electrochemically-detectable product. This combination is extremely rare and similar enzymes for arbitrary target molecules do not usually exist.

Alternate approaches to this problem seek to decouple the recognition and detection elements of the sensor. In particular, electrochemical aptamer-based (EAB) sensors link target-specific oligonucleotides (*aptamers*) to redox-active labels. The electrochemical reactivity of the label is independent of the target and of the specific aptamer, making detection of a wide range of target molecules possible by simply replacing the aptamer.[53]

1.4.2 Electrochemical Aptamer-Based Sensors

Aptamers are oligomers of nucleic acids (most commonly, DNA) which are designed to bind to a specific target molecule through an in-vitro selection process.[55] Upon target binding, aptamers undergo a conformational change which can be leveraged to construct a sensor. In an EAB sensor, the aptamer is adsorbed to the surface of an electrode (typically using gold-thiol bonds to form a low-density, self-assembled monolayer) and functionalized with an electrochemically-active reporter such as methylene blue. In solution, the redox reporter resides some distance away from the electrode surface. However, upon target binding, the aptamer changes conformation in such a way that the redox

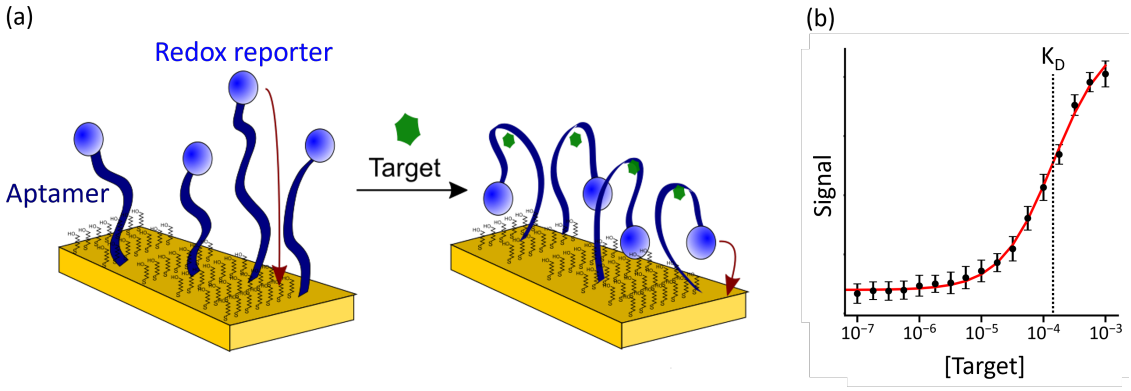

Figure 1.6: Operating principles of an EAB sensor. (a) Aptamers undergo conformational change upon target binding. In an EAB sensor, this is exploited to move a redox-active species closer to the electrode surface upon target binding, generating an electrochemically-measurable response. (b) The electrochemical signal output of an EAB sensor is proportional to target concentration. The response typically follows a Langmuir-Hill isotherm centered around the aptamer-target dissociation constant, K_D. Adapted with permission from [54].

reporter is brought closer to the electrode surface (Figure 1.6a).[12][53] This decrease in distance makes the electron transfer kinetics between the electrode and the redox reporter faster – a change that can be measured electrochemically.[7] Moreover, the electrochemical signal can quantify the concentration of the target molecule. At concentrations far below the aptamer-target dissociation constant (K_D), the signal is characteristic of the unbound conformation of the aptamer; while at concentrations far above K_D the signal is characteristic of the bound conformation. Near K_D, the signal is a linear combination of the bound and unbound fractions of the aptamers on the surface and depends strongly on target concentration (Figure 1.6b). Aptamers can be designed with disso-

[12]Sensors can also be designed such that the redox reporter moves farther from the surface upon target binding.

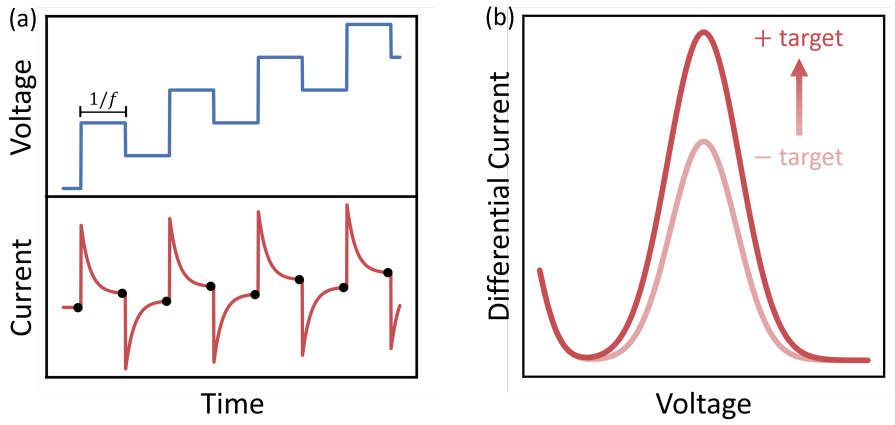

Figure 1.7: (a) Square wave voltammetry is performed by applying an increasing, pulsed voltage (top) and sampling the current response (bottom) at the end of each pulse. This method aims to eliminate non-Faradaic contributions by sampling at a low enough frequency (as determined by the pulse width 1/f) that the capacitive contribution has nearly vanished. (b) Square wave voltammetry applied to an EAB sensor. The peak associated with the redox probe increases in magnitude after the sensor is exposed to its target molecule, because the redox probe is now closer to the electrode surface and electron transfer kinetics are faster.

ciation constants in the clinically-relevant concentration range of their target molecule, yielding biosensors suitable for therapeutic monitoring.[56]

Indeed, EAB sensors have been developed for more than a dozen targets, including both small molecules and proteins.[53] They can accurately measure target molecular concentrations *in-vivo*, monitoring concentrations of their targets,[54] measuring individual metabolic rates,[57] and even enabling feedback-controlled dosing to maintain constant plasma concentrations in living rats.[58] While the modularity of these sensors (i.e. the ease of adapting a sensor to a new target) is given by aptamers, their rapid and reliable operation depends on the electrochemical interrogation method. The most common method to date relies on square wave voltammetry (SWV) as shown in Figure 1.7.

The success of SWV is largely due to its ability to negate background capacitance and return Faradaic currents with high signal-to-noise ratios (Figure 1.7). Furthermore, measuring sequential square wave voltammograms at two different frequencies has enabled drift correction and long-duration *in-vivo* measurements.[59] However, the technique has several drawbacks. First, the its time resolution is limited to the order of ten seconds due to the need to acquire two sequential voltammograms for a measurement – higher time resolution would be beneficial for monitoring rapid physiological processes such as neurotransmitter release.[60] Second, the peak current measured in SWV is affected by both the electron transfer rate constant (which depends on the target concentration) and the number of redox-active species on the surface (which varies sensor-to-sensor based on surface area and aptamer packing density) requiring calibration of each individual sensor before its deployment.[59] For these reasons, a variety of other electrochemical methods including cyclic voltammetry,[61] AC voltammetry,[62] amperometry,[63] and single-frequency impedance measurements[64] have been employed to interrogate EAB sensors. Chapter 5 of this thesis introduces a multi-frequency impedance measurement which enables rapid, calibration-free interrogation of EAB sensors.

1.5 Thesis Summary

Chapters 2, 3, and 4 are devoted to single-entity electrochemistry. In Chapter 2, the reactivity of single platinum nanoparticles is examined as they collide with inert, partially active, or fully electrochemically active microelectrodes.

Chapter 3 details the development of collisional single-particle impedance spectroscopy. The impedance spectrum of a microelectrode is continuously recorded and particle impacts are observed via discrete changes in the impedance.

Chapter 4 extends single-particle impedance spectroscopy to the scanning electrochemical cell microscope (SECCM) configuration. Impedance spectra are recorded of individual, sodium-intercalating nanoparticles and their respective electron- and ion-transfer rates are extracted, revealing suprisingly large particle-to-particle differences in these fundamental material properties.

Chapter 5 uses the fast impedance spectroscopy method detailed in Chapter 3 as an interrogation method for electrochemical aptamer-based (EAB) biosensors. This method gives better precision and time resolution than the previous standard, and is demonstrated to operate both *in vitro* and *in vivo*.

References

[1] M. Piccolino, *Brain Research Bulletin* **1998**, *46*, 381–407.

[2] R. A. Marcus, *The Journal of Chemical Physics* **1956**, *24*, 966–978.

[3] Z. Yang, J. Zhang, M. C. W. Kintner-Meyer, X. Lu, D. Choi, J. P. Lemmon, J. Liu, *Chemical Reviews* **2011**, *111*, 3577–3613.

[4] J. C. Siu, N. Fu, S. Lin, *Accounts of Chemical Research* **2020**, *53*, 547–560.

[5] N. J. Ronkainen, H. B. Halsall, W. R. Heineman, *Chemical Society Reviews* **2010**, *39*, 1747.

[6] R. G. Compton, C. E. Banks, *Understanding Voltammetry*, 3rd, World Scientific, **2018**.

[7] A. J. Bard, L. R. Faulkner, *Electrochemical Methods: Fundamentals and Applications*, 2nd ed., John Wiley & Sons, **2001**.

[8] S. E. F. Kleijn, S. C. S. Lai, M. T. M. Koper, P. R. Unwin, *Angewandte Chemie International Edition* **2014**, *53*, 3558–3586.

[9] M. Kang, C. L. Bentley, J. T. Mefford, W. C. Chueh, P. R. Unwin, *ACS Nano* **2023**, *17*, 21493–21505.

[10] W. H. Coulter, Means for counting particles suspended in a fluid, US Patent 2,656,508, **1953**.

[11] B. M. Quinn, P. G. V. '. Hof, S. G. Lemay, *Journal of the American Chemical Society* **2004**, *126*, 8360–8361.

[12] J. Chung, P. Hertler, K. W. Plaxco, L. Sepunaru, *Journal of the American Chemical Society* **2021**, *143*, 18888–18898.

[13] K. Micka, *Collection of Czechoslovak Chemical Communications* **1956**, *21*, 647–651.

[14] I. Jones, R. Kaye, *Journal of Electroanalytical Chemistry and Interfacial Electrochemistry* **1969**, *20*, 213–221.

[15] X. Xiao, A. J. Bard, *Journal of the American Chemical Society* **2007**, *129*, 9610–9612.

[16] S. V. Sokolov, S. Eloul, E. Kätelhön, C. Batchelor-McAuley, R. G. Compton, *Physical Chemistry Chemical Physics* **2017**, *19*, 28–43.

[17] L. A. Baker, *Journal of the American Chemical Society* **2018**, *140*, 15549–15559.

[18] S.-M. Lu, K. J. Vannoy, J. E. Dick, Y.-T. Long, *Journal of the American Chemical Society* **2023**, *145*, 25043–25055.

[19] L. Zhang, O. J. Wahab, A. A. Jallow, Z. J. O'Dell, T. Pungsrisai, S. Sridhar, K. L. Vernon, K. A. Willets, L. A. Baker, *Analytical Chemistry* **2024**, *96*, 8036–8055.

[20] W. Cheng, R. G. Compton, *TrAC - Trends in Analytical Chemistry* **2014**, *58*, 79–89.

[21] S. J. Percival, B. Zhang, *The Journal of Physical Chemistry C* **2016**, *120*, 20536–20546.

[22] L. D. Ha, K. J. Kim, S. J. Kwon, B.-Y. Chang, S. Hwang, *Small* **2023**, *19*, 2302158.

[23] W. Wei, T. Yuan, W. Jiang, J. Gao, H.-y. Chen, W. Wang, *Journal of the American Chemical Society* **2020**, DOI `10.1021/jacs.0c06171`.

[24] K. Kanokkanchana, E. N. Saw, K. Tschulik, *ChemElectroChem* **2018**, *5*, 3000–3005.

[25] Y. Li, J. T. Cox, B. Zhang, *Journal of the American Chemical Society* **2010**, *132*, 3047–3054.

[26] T. Sun, Y. Yu, B. J. Zacher, M. V. Mirkin, *Angewandte Chemie International Edition* **2014**, *53*, 14120–14123.

[27] G. Askarova, M. Hesari, K. Barman, M. V. Mirkin, *ACS Applied Materials & Interfaces* **2023**, *15*, 47168–47176.

[28] G. Jayamaha, M. Maleki, C. L. Bentley, M. Kang, *The Analyst* **2024**, *149*, 2542–2555.

[29] X. Xu, D. Martín-Yerga, N. E. Grant, G. West, S. L. Pain, M. Kang, M. Walker, J. D. Murphy, P. R. Unwin, *Small* **2023**, *19*, 1–10.

[30] J. Zhao, M. Wang, Y. Peng, J. Ni, S. Hu, J. Zeng, Q. Chen, *Angewandte Chemie International Edition* **2023**, DOI `10.1002/anie.202304424`.

[31] C. H. Ryu, H. Ren, *Nano Letters* **2024**, *24*, 6112–6116.

[32] C. Meng, S. Knežević, F. Du, Y. Guan, F. Kanoufi, N. Sojic, G. Xu, *eScience* **2022**, *2*, 591–605.

[33] Y. Wei, Y. Zhang, J. Pan, T. Chen, X. Xing, W. Zhang, Z. Lu, *Angewandte Chemie International Edition* **2023**, *62*, e202214103.

[34] J.-F. Lemineur, H. Wang, W. Wang, F. Kanoufi, *Annual Review of Analytical Chemistry* **2022**, *15*, 57–82.

[35] B. Niu, W. Jiang, B. Jiang, M. Lv, S. Wang, W. Wang, *Nature Communications* **2022**, *13*, DOI 10.1038/s41467-022-30058-4.

[36] O. J. Wahab, M. Kang, P. R. Unwin, *Current Opinion in Electrochemistry* **2020**, *22*, 120–128.

[37] X. Xu, D. Martín-Yerga, N. E. Grant, G. West, S. L. Pain, M. Kang, M. Walker, J. D. Murphy, P. R. Unwin, *Small* **2023**, *19*, 1–10.

[38] I. M. Ornelas, P. R. Unwin, C. L. Bentley, *Analytical Chemistry* **2019**, *91*, 14854–14859.

[39] G.-Z. Zhu, S. Prabhudev, J. Yang, C. M. Gabardo, G. A. Botton, L. Soleymani, *The Journal of Physical Chemistry C* **2014**, *118*, 22111–22119.

[40] E. Fahrenkrug, D. H. Alsem, N. Salmon, S. Maldonado, *Journal of The Electrochemical Society* **2017**, *164*, H358–H364.

[41] A. Lasia, *Electrochemical Impedance Spectroscopy and its Applications*, Springer New York, **2014**.

[42] E. Warburg, *Annalen der Physik* **1899**, *303*, 493–499.

[43] A. Lasia, *The Journal of Physical Chemistry Letters* **2022**, *13*, 580–589.

[44] J. E. B. Randles, *Discussions of the Faraday Society* **1947**, *1*, 11.

[45] M. Fleischmann, S. Pons, *Journal of Electroanalytical Chemistry and Interfacial Electrochemistry* **1988**, *250*, 277–283.

[46] P. G. Bruce, A. Lisowska-Oleksiak, P. Los, C. A. Vincent, *Journal of Electroanalytical Chemistry* **1994**, *367*, 279–283.

[47] A. C. Lazanas, M. I. Prodromidis, *ACS Measurement Science Au* **2023**, *3*, 162–193.

[48] G. S. Popkirov, R. N. Schindler, *Review of Scientific Instruments* **1992**, *63*, 5366–5372.

[49] G. S. Popkirov, R. N. Schindler, *Review of Scientific Instruments* **1993**, *64*, 3111–3115.

[50] A. E. G. Cass, G. Davis, G. D. Francis, H. A. O. Hill, W. J. Aston, I. J. Higgins, E. V. Plotkin, L. D. L. Scott, A. P. F. Turner, *Analytical Chemistry* **1984**, *56*, 667–671.

[51] D. Rodbard, *Diabetes Technology & Therapeutics* **2016**, *18*, S2–3.

[52] J.-S. Kang, M.-H. Lee, *The Korean Journal of Internal Medicine* **2009**, *24*, 1–10.

[53] A. M. Downs, K. W. Plaxco, *ACS Sensors* **2022**, *7*, 2823–2832.

[54] B. Roehrich, K. K. Leung, J. Gerson, T. E. Kippin, K. W. Plaxco, L. Sepunaru, *ACS Sensors* **2023**, *8*, 3051–3059.

[55] C. Tuerk, L. Gold, *Science* **1990**, *249*, 505–510.

[56] A. M. Downs, J. Gerson, K. K. Leung, K. M. Honeywell, T. Kippin, K. W. Plaxco, *Scientific Reports* **2022**, *12*, 1–10.

[57] A. Idili, J. Gerson, T. Kippin, K. W. Plaxco, *Analytical Chemistry* **2021**, *93*, 4023–4032.

[58] P. Dauphin-Ducharme, K. Yang, N. Arroyo-Currás, K. L. Ploense, Y. Zhang, J. Gerson, M. Kurnik, T. E. Kippin, M. N. Stojanovic, K. W. Plaxco, *ACS Sensors* **2019**, *4*, 2832–2837.

[59] B. S. Ferguson, D. A. Hoggarth, D. Maliniak, K. Ploense, R. J. White, N. Woodward, K. Hsieh, A. J. Bonham, M. Eisenstein, T. E. Kippin, K. W. Plaxco, H. T. Soh, *Science Translational Medicine* **2013**, *5*, DOI 10.1126/scitranslmed.3007095.

[60] D. Bruns, R. Jahn, *Nature* **1995**, *377*, 62–65.

[61] M. A. Pellitero, S. D. Curtis, N. Arroyo-Currás, *ACS Sensors* **2021**, *6*, 1199–1207.

[62] S. Zhao, W. Yang, R. Y. Lai, *Biosensors and Bioelectronics* **2011**, *26*, 2442–2447.

[63] N. Arroyo-Currás, P. Dauphin-Ducharme, G. Ortega, K. L. Ploense, T. E. Kippin, K. W. Plaxco, *ACS Sensors* **2018**, *3*, 360–366.

[64] A. M. Downs, J. Gerson, K. L. Ploense, K. W. Plaxco, P. Dauphin-Ducharme, *Analytical Chemistry* **2020**, *92*, 14063–14068.

Chapter 2

Single Particle Characterization at Active and Partially Active Electrodes

Portions of this work were published in:

Roehrich, B.; Sepunaru, L. Nanoimpacts at Active and Partially Active Electrodes: Insights and Limitations. *Angewandte Chemie International Edition* **2020**, 59 (43), 19184–19192.

https://doi.org/10.1002/anie.202007148.

2.1 Introduction

Nanomaterials have become increasingly prevalent in catalysis. Unlike molecular catalysts, these materials are not atomically precise and thus have non-homogenous sizes, morphologies, and catalytic activities. Typical analytical techniques measure macroscopic, ensemble properties and lose the nuances of individual entities. A better understanding of the properties of individual nanocatalysts will allow for better design and control of macroscopic systems. New methods are therefore needed to analyze these materials. The electrochemical nanoimpact technique has recently emerged as a means of measuring the properties of individual entities rather than ensembles.[1–7] This method has recently been used to study particle size,[8–10] porosity,[11, 12] and heterogenous catalytic rates on a single-particle basis;[13–15] these parameters are critically important to the performance of an electrocatalyst. While a wide variety of systems have been analyzed through particle–electrode impacts,[5, 6, 16, 17] several typical schemes have emerged. In the simplest case, the particle is directly reduced or oxidized upon electrode impact, as in the oxidation of Ag nanoparticles.[9, 18] Alternatively, electroactive particles impacting an inert electrode allow a current to pass in an electrocatalytic amplification (ECA)[19, 20] scheme, or an insulating particle may block a redox event at an active electrode and cause a corresponding, discrete decrease in current.[21, 22]

The requirement for an active particle–inactive electrode in ECA schemes (or vice versa in blocking schemes) limits both the scope of particle–electrode impact detection and the depth of mechanistic insight such impacts can reveal. ECA schemes have typ-

ically required the addition of an inner-sphere redox probe, such as hydrogen peroxide or hydrazine,[5, 19, 20] or used protons or oxygen already present in solution.[8, 12, 19, 23–26] Regardless of the redox species, the measurements require that the particle be more active toward the redox reaction than the electrode. This allows one to choose a potential window such that the particle is active toward the reaction of choice while the electrode remains inert—guaranteeing measurable (above noise) currents upon particle impact but severely confining parameters of study. The ability to measure nanoimpacts at active electrodes would increase the versatility of the technique, by increasing the possible potential windows and permutations of electrode and particle materials, and by allowing simultaneous measurement of the properties of both materials.

We posed an initial question: Can catalytic particles be detected at an active electrode? Here we present a series of model cases of electroactive particle–active electrode impact events, showing that individual particle detection is possible at partially active electrodes and can be used to glean mechanistic insight. The electrode must have a larger overpotential toward the redox event than the particle so that impacting particles produce a measurable increase in current, however we show that the product of an electrode reaction can be consumed by the catalytic particle and yield detectable collision events. Furthermore, our results shed new light on the deactivation mechanism of platinum catalysts during the hydrogen evolution reaction. This establishes an additional tool in nanoimpact studies, broadening the material scope of analyte, particle, and electrode to enhance our understanding of electrochemical processes occurring at the nanoscale.

2.2 Hydrogen Evolution Reaction on Individual Platinum Nanoparticles

We chose the hydrogen evolution reaction (HER) as a first model system to study particle impacts at an active electrode. Several groups have used the HER in collisional studies due to its inner-sphere nature.[12, 20, 23, 27] As seen in the voltammograms in Figure 2.1A, the overpotential of the HER is approximately 200 mV larger on Au compared to Pt (the high scan rate was chosen to minimize deactivation of the Pt electrode, as discussed later). Therefore, one can apply a potential to an Au electrode such that it does not catalyze the HER, while a Pt particle does catalyze the HER and thus produces a discrete current transient upon contact with the electrode. Using sufficiently dilute particle suspensions (6 pM), individual impacts can be detected and resolved. We measured current–time traces as Pt nanoparticles (30 nm diameter, 2.7) collided stochastically with an Au microelectrode in an acidic (pH 5, 20 mM citrate), nitrogen-purged solution. Dynamic light scattering measurements show that the particles are stable over the experimental time scale (2.8). Each observed current transient arises from the collision of a single Pt nanoparticle with the electrode. Chronoamperomograms obtained at an inactive electrode are well explained by the HER mechanism on Pt. Pt nanoparticle impacts produce transient current spikes at -300 mV vs SCE (Figure 2.1B). This potential is sufficient to drive the Volmer step (Equation 1) but not the Heyrovsky step (Equation 2).[23, 28, 29] Diffusing particles that collide with the electrode adsorb a monolayer of

hydrogen via a 1-electron process (Equation 2.1) without catalyzing further reactions. This produces a spike-like current transient for each individual particle that impacts the electrode, the reaction is complete within 5 ms (2.9). At -660 mV, the Heyrovsky step can occur on Pt while the Au electrode remains inert (Figure 2.1A). Impacting Pt particles produce a noticeable "step" after the Volmer spike, due to this additional catalytic reduction process (Figure 1C). These observations agree with recent work by the Zhang group.[23]

$$H^+ + e^- \longrightarrow H_{ads} \tag{2.1}$$

$$H_{ads} + H^+ + e^- \longrightarrow H_2 \tag{2.2}$$

Figure 2.1D shows the current response produced by Pt nanoparticles colliding with a partially active Au electrode (-750 mV). As before, the step response is due to the Heyrovsky step of the HER. However, the spikes preceding the steady-state current, indicative of the rapid Volmer step, are conspicuously absent. As an explanation for this phenomenon, we propose that Au electrode-produced hydrogen gas saturates the nanoparticles before they reach the electrode surface. Hydrogen adsorption is known to be facile on Pt in acidic conditions,[30] so particles that approach the electrode will rapidly adsorb a monolayer of hydrogen concentrated in the vicinity of the active electrode. Consequently, the hydrogen-saturated particles that impact the electrode begin producing H_2 directly via Equation 2.2 (the Heyrovsky step is the likely H_2 formation step on Pt nanoparticles).[15, 23] This is in line with previous reports of a more step-

like response of Pt nanoparticle impacts in H_2-saturated solution compared to N_2- or He-saturated solutions.[12, 27] These results show that the use of an active electrode can provide valuable mechanistic insight into the reactions occurring at impacting particles by generating reactive species in-situ. We note that the frequency of events is lower at a fully active electrode (-850 or -1000 mV, 2.10), likely due to the extremely low proton concentration near the electrode. Collisions recorded in alkaline solution (pH 8, 2.11) follow a similar trend, with Volmer spikes persisting to more negative potentials due to the slower Volmer kinetics in alkaline media.[31]

Table 2.7.2 shows the impact frequencies measured for the HER at the three potentials used in this study. In all cases the experimental frequency are similar, but lower than the theoretical frequency by a factor of 3-4,[32] this lower frequency is similar to previous nanoimpact studies and the cause is not well understood.[20, 33, 34] The frequency remains unchanged in weaker electrolyte (5 mM citrate, Table 2.7.2), showing that electrochemical migration does not play a significant role in the low experimental frequency. The frequency also does not appear to be affected by the nature of the electrochemical reaction at the particle, or by the partial activation of the electrode towards the HER.

The data shown in Figure 2.1 can be used to evaluate the heterogeneity of the nanoparticles. After collecting statistically significant numbers of spike and step events, the charges and steady state currents could be represented in a meaningful histogram as shown in Figure 2.2. Using the data shown in Figure 2.2A, we can calculate the elec-

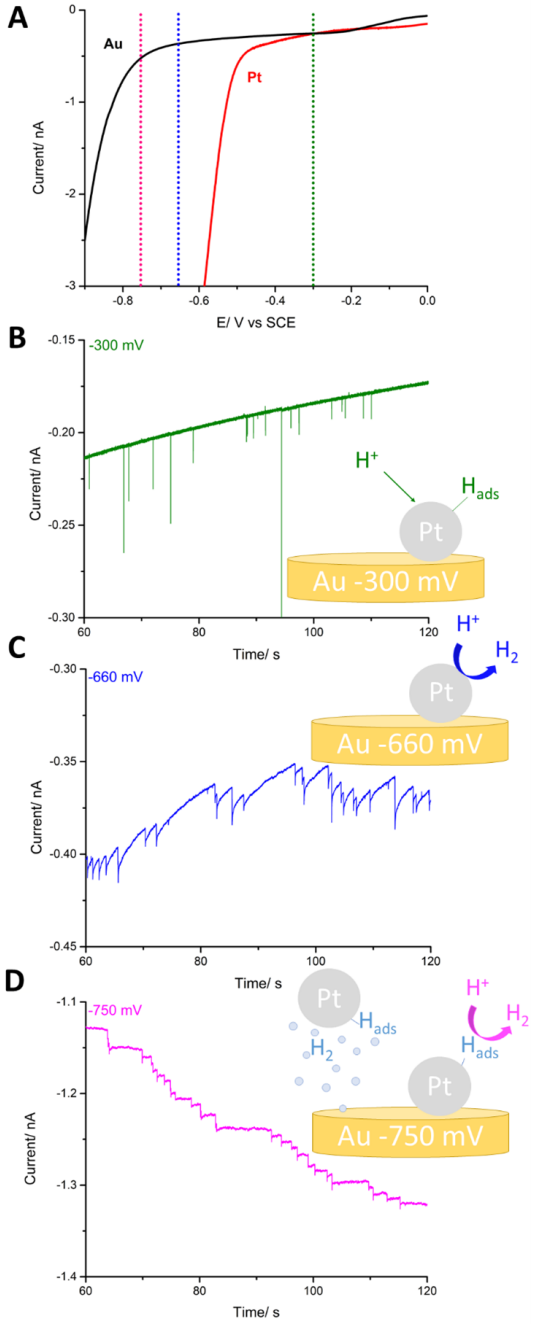

Figure 2.1: (A) Linear sweep voltammograms recorded at 250 mV/s of Au and Pt microelectrodes in nitrogen-saturated, pH 5, 20 mM citrate solution. (B–D) Representative chronoamperomograms of 30 nm diameter Pt nanoparticles (6 pM) impacting an Au electrode under the same conditions as (A) with applied biases of -300, -660 and -750 mV vs SCE, respectively.

troactive surface area (EASA) of the particles. Assuming a charge density of 210 μCcm^{-2} for a hydrogen monolayer on polycrystalline Pt and a surface coverage of 77%,[35] the average spike charge of 45 fC corresponds to an EASA of $2.7 \times 10^4 nm^2$ per particle. We note that the surface coverage of 77% is reported at the onset of hydrogen evolution; the surface coverage should be less at -300 mV, well before the onset of the HER, so our calculated EASA is an underestimation. This value is still an order of magnitude larger than geometrically expected for a 15 nm radius sphere due to surface roughness and porosity (2.7). Previous reports on particles from the same manufacturer have measured comparably large surface areas, attributed to particles' porosity.[11, 23, 36]

To validate the active electrode–active particle scheme, we also measured steady-state currents at -750 mV. As previously described, these currents are due to the full hydrogen evolution reaction occurring on colliding nanoparticles. The current after each impact event remains constant until the next impact, the potential is sufficiently negative to suggest a mass transport limit (steps recorded at -850 mV in 2.10 are not significantly larger and are on the order of 10-15 pA). We calculated the steady-state currents for these particles based on either hydronium, diprotic citric acid, or hydrogen gas diffusion (Supporting Information).[37] The currents in Figure 2.2B are not well explained by the diffusion of any of these species. Rather, the hydrogen evolution reaction likely proceeds via a coupled chemical–electrochemical mechanism in the citric acid buffer. The modelling of this process is complex, and previous reports have observed smaller currents than predicted.[38] Based on the citric acid concentration used here, the steady

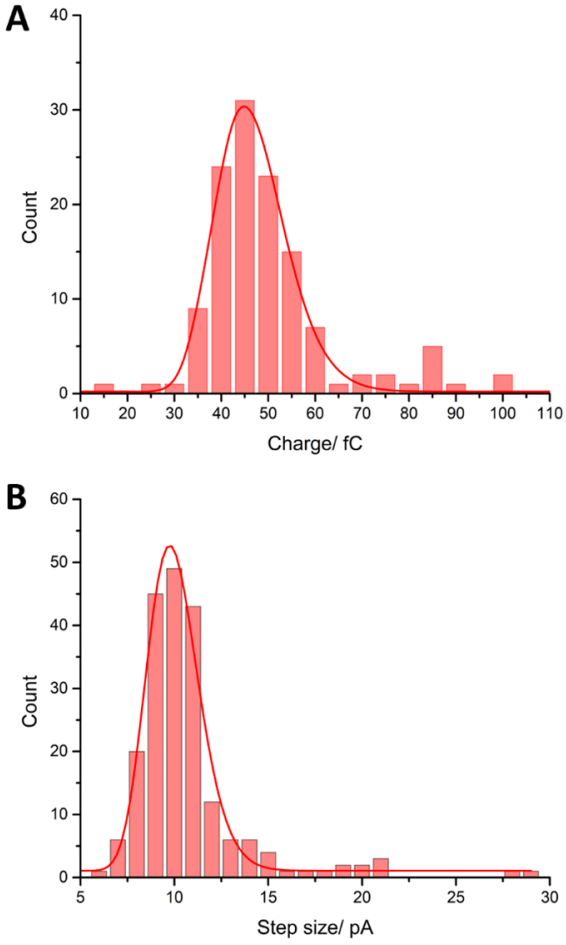

Figure 2.2: (A) Distribution of integrated current transients recorded at -300 mV vs SCE. Assuming a log-normal distribution, the fitted mode corresponds to 45 fC with a standard deviation of 8 fC (N = 134). (B) Distribution of steady-state currents recorded at -750 mV vs SCE; the mode is 9.8 pA with a standard deviation of 1.4 pA (N = 204).

state current should be less than 20% of the steady state current expected from a simpler electrochemical reaction.[38] Despite this, the distribution of steady-state currents shown in Figure 2.2B is qualitatively similar to the distribution of charge obtained at the inactive electrode (Figure 2.2A): both parameters follow log-normal distributions and the relative standard deviations (RSD) in Figures 2.2A and 2.2B are 0.18 and 0.14, respectively. The distributions suggest both the active and inactive electrode measurements are probing the size of the particles: the charge in Figure 2.2A is proportional to the total EASA while the currents in Figure 2.2B scale with the particle radius. The RSD in Figure 2.2B is smaller because the particles are fairly monodisperse in radius (2.7), but likely have highly variable internal structures due to their porosity. This result shows that active particle–active electrode schemes can also yield physically meaningful measurements.

2.3 Deactivation of Pt During HER

We noted that particle collisions measured at -660 mV vs SCE did not produce true steady-state responses, yet at -750 mV they did. We attributed the decay in current at -660 mV to deactivation of the Pt particles, which has been reported previously (especially in other nano-impact studies).[8, 19, 20, 27, 39] Because we also observed deactivation of a Pt microelectrode toward the HER (2.12), we questioned whether Pt particle impacts at a partially-active Pt electrode could help explain the deactivation mechanism. Specifically, evidence for size dependency on the activity of nanoparticles catalysis has been shown before.[13] Partial or total deactivation of the Pt electrode could allow for Pt particle

detection, letting us decouple the size effect from other physical parameters and delineate the origin of deactivation.

Figure 2.3 shows chronoamperomograms measured for this permutation. At -300 mV the Volmer step (Equation 2.1) can occur on Pt. The Pt electrode adsorbs a monolayer of hydrogen without catalyzing further reactions. Pt particles stochastically collide with the electrode, adopt its potential, and adsorb hydrogen, producing a spike response in Figure 2.3A analogous to the current transients observed in Figure 2.1B. Integration of the spikes in Figure 2.3A yields charges on the order of 50 fC, as was observed with Pt particles colliding with an Au electrode.

Chronoamperomograms measured at more reducing potentials show electrode deactivation. Based on the linear sweep voltammogram shown in Figure 2.1A and on the cyclic voltammogram shown in 2.12, we expect currents on the order of several nA when the Pt electrode is active toward the HER (<-550 mV vs SCE). Instead, the background current in Figure 2.3B is an order of magnitude smaller ($I_{ss} < 300$ pA) compared to the theoretical value. In a similar way, Pt nanoparticles impact the electrode, catalyze the full HER, and become deactivated on a time scale of approximately 1 second. The Pt NP deactivation time scale is significantly longer than the instrument-limited response that is dictated by the experimental sampling rate (100 Hz), hence reflecting a true deactivation process.

At -750 mV (Figure 2.3C), the electrode produces H_2. As before, particles adsorb electrode-produced H_2; collisions produce a step response due to the Heyrovsky step

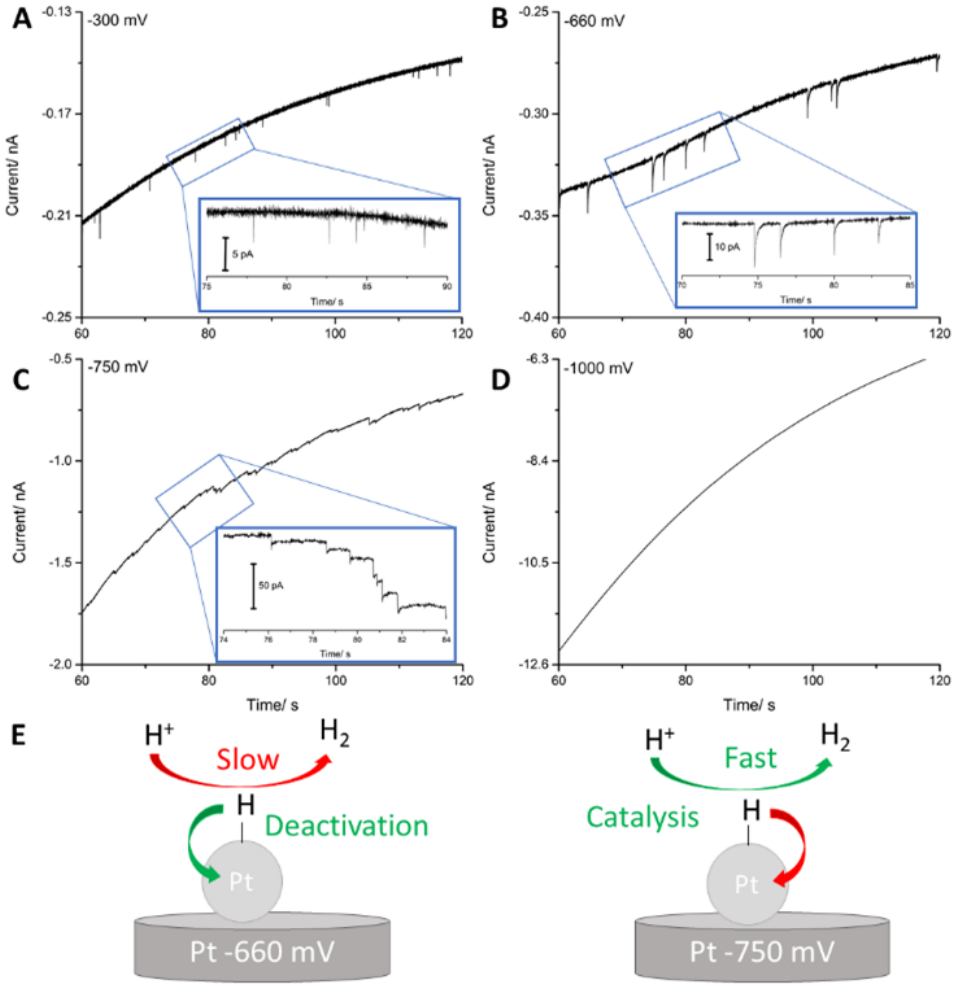

Figure 2.3: Representative chronoamperomograms of 30 nm diameter Pt nanoparticles (6 pM) impacting a Pt ultramicroelectrode biased at -300 (A), -660 (B), -750 (C), or -1000 (D) mV vs SCE in nitrogen-saturated, pH 5, 20 mM citrate solution. Insets: linear baseline subtractions of the chronoamperomograms. (E) Proposed mechanisms for the current transients observed in (B) and (C).

(Equation 2.2). However, our recordings of the nanoparticles' stochastic collisions clearly indicate that the Pt nanoparticles remain active toward HER (Figure 2.3C inset). No events are observed at -1000 mV (Figure 2.3D) due to the low proton concentration near the fully active electrode. We note that the steadily decreasing current, rather than a steady state, in Figure 2.3D indicates significant deactivation of the Pt microelectrode.

Previous reports typically attribute Pt deactivation during the HER to hydrogen absorption into the crystal lattice of Pt: while hydrogen adsorption to the surface of the catalyst is necessary for the reaction to occur, hydrogen incorporation into the lattice may reduce the catalytic activity.[19, 20, 27, 40] Our results support this hypothesis; a schematic to describe this mechanism is shown in Figure 2.3E. Hydrogen absorption into the lattice first requires hydrogen adsorption to the surface of Pt. At mild potentials the HER kinetics are slower, causing adsorbed hydrogen to spend more time on the surface because the Heyrovsky step is rate-limiting on Pt. At more negative potentials the residence time of H atoms on the Pt surface is shorter, they are quickly consumed by the Heyrovsky step and less likely to diffuse into the lattice; hence the slower deactivation.

This explanation seems contradictory to the fact that Pt particle impacts are detectable in hydrogen-saturated solutions, whether the electrode-produced hydrogen in this report or externally added hydrogen as previously reported.[27] However, hydrogen permeation through Pt is kinetically slow without an electrochemical driving force.[41] Hydrogen adsorbed by Pt particles pre-impact does not cause deactivation because the electrochemical potential is approximately equal across the freely diffusing parti-

cle–solution interface. Once the particle collides with the electrode, a sufficient potential difference can be built across the interface and permeation can occur. When the HER is kinetically limited, hydrogen diffusion into the Pt lattice dominates and deactivation occurs. Under a mass transport-limited regime, the Heyrovsky step dominates and fewer hydrogen atoms diffuse into the lattice. The differing responses of the µm-scale electrode and nm-scale particles at -750 mV, under mass transport control, support this hypothesis. Proton flux to the particles is significantly larger due to their smaller size, minimizing deactivation. The proton flux to the microelectrode is smaller compared to the Pt nanoparticle, and the background current seen in Figure 2.3C steadily decreases due to deactivation via hydrogen diffusion into the electrode. While preliminary x-ray diffraction results using a macroscopic Pt electrode do not show significant structural changes during the HER (Figure 2.13), higher resolution diffraction data is needed to thoroughly assess this hypothesis. The competing rates of proton reduction on Pt and hydrogen incorporation into Pt control the deactivation of the catalyst. The active electrode–active particle impact scheme allows direct, simultaneous comparison of the same material in different size regimes, revealing mass transport as a factor in catalyst stability. This analysis yields new insight into the puzzle of Pt deactivation during the HER.

2.4 Local Environmental Effects during ORR

Based on these results, we sought to understand what further mechanistic information could be gleaned through the use of an active electrode. Oxygen reduction was chosen

as a second model inner-sphere system. The oxygen reduction reaction (ORR) can yield either hydrogen peroxide or water, dependent on solution conditions, electrode material, and applied potential. On Pt, 4-electron reduction to water (Equation 2.3) is preferred while on carbon 2-electron reduction to hydrogen peroxide dominates at mild potentials (Equation 2.4).[42–44] Hydrogen peroxide formed on a carbon electrode could be further reduced to water by impacting Pt nanoparticles (Equation 2.5).[19]

$$O_2 + 4H^+ + 4e^- \longrightarrow 2H_2O \tag{2.3}$$

$$O_2 + 2H^+ + 2e^- \longrightarrow H_2O_2 \tag{2.4}$$

$$H_2O_2 + 2H^+ + 2e^- \longrightarrow 2H_2O \tag{2.5}$$

Figure 2.4A shows a chronoamperomogram obtained using a carbon fiber microelectrode biased at -400 mV vs SCE. The solution contained 6 pM Pt nanoparticles in phosphate buffer (pH 8, 20 mM) and atmospheric oxygen, corresponding to an O_2 concentration of 260 μM.[45] As seen in the inset linear sweep voltammograms, this potential is sufficient for O_2 reduction on Pt via Equation 2.3, while no reaction occurs on the carbon microelectrode. As a control experiment, no impacts are visible if the electrode is biased at 0 V vs SCE (Figure 2.14). The discrete events observed in Figure 2.4A are attributed to 4-electron reduction of O_2 on individual Pt nanoparticles. Here, a carbon electrode was chosen due to its lower activity toward the competing HER;[46] proton reduction does not occur until almost -2 V under these conditions (inset, Figure 2.4).

In Figure 2.4B, events are again attributed to individual particle impacts. At this potential (-800 mV vs SCE), the carbon electrode is active toward H_2O_2 production as in

Equation 2.4. Pt particles that collide with the electrode further reduce the H_2O_2 product to H_2O via the additional 2-electron process shown in Equation 2.5. This produces discrete steps in the chronoamperomogram even though the electrode is active toward O_2 reduction. Particle impacts were only detectable due to their further reduction of electrode-produced H_2O_2. We also allowed Pt nanoparticles to collide with a Pt microelectrode biased at -400 mV in the presence of oxygen, analogous to the data shown in Figure 2.3. No current transients were observed (Figure 2.15). The electrode reduces oxygen to water without deactivating, so the concentration of oxygen near the electrode surface is too small to observe a single-particle impact event.

We measured the discrete steady-state currents observed at the active (-800 mV) and inactive (-400 mV) C microelectrode. Based on Equations 2.3 and 2.5, particles that reduce O_2 directly to H_2O (at the inactive electrode) should produce steady-state currents twice as large as those that reduce H_2O_2 to H_2O (at the active electrode). As shown in Figure 2.4C, this is indeed the case. Steady-state currents measured at the inactive electrode (blue, 8.5 $\pm$ 2.5 pA) were approximately twice as large as those measured at the active electrode (red, 5.0 $\pm$ 1.5 pA). We assume the measured 8.5 pA steps correspond to 4-electron reduction; however, the physical process likely has an n of less than 4. This is because hydrogen peroxide formed as an ORR intermediate on Pt may diffuse away from the particle before it is further reduced, preventing full 4-electron transfer.[25, 47] Thus, the deviation from the expected two-to-one ratio in steady- state

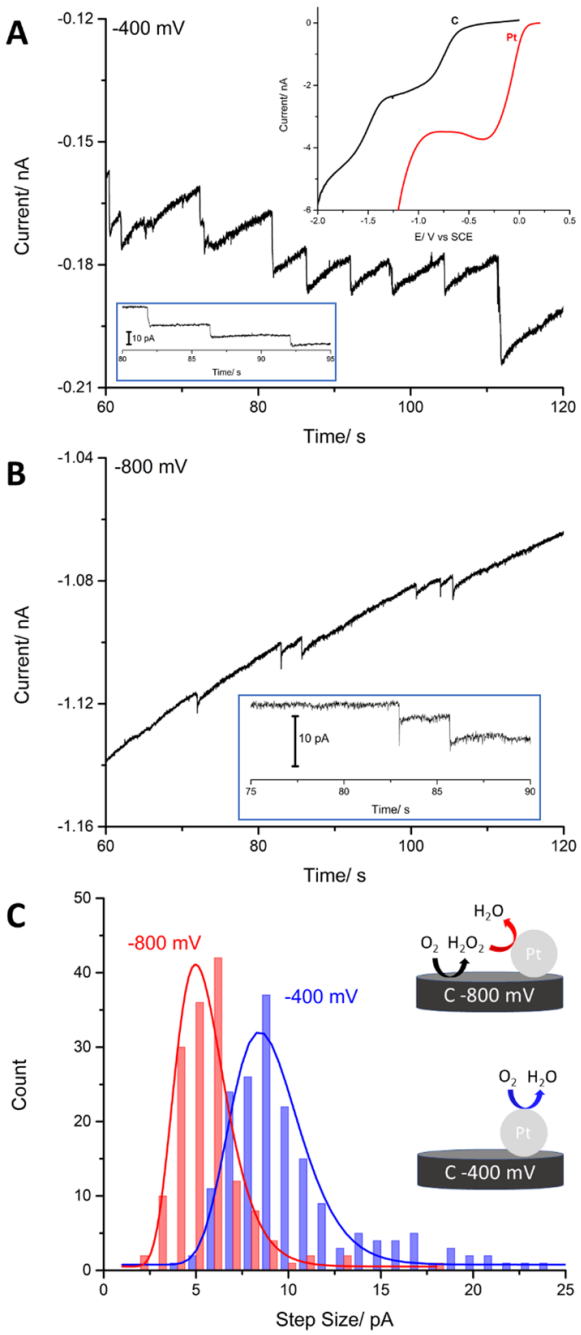

Figure 2.4: Representative chronoamperomograms of 30 nm diameter Pt nanoparticles (6 pM) impacting a carbon electrode biased at (A) -400 mV and (B) -800 mV in air-saturated 20 mM pH 8.2 phosphate buffer. Insets: linear sweep voltammograms (20 mV/s) of C and Pt microelectrodes under the same conditions, in the absence of Pt particles; baseline-subtracted chronoamperomograms. (C) Log-normal fitted distributions of step sizes measured using a carbon electrode biased at either -400 (N = 181) or -800 mV (N = 150), schematics show the proposed mechanistic steps.

currents is predominantly due to the high mass transport nature of the hydrogen peroxide intermediate.[47, 48]

As in the HER, the particle impact frequency during the ORR is lower than predicted by diffusion (Table 2.7.2). The frequency is also similar at the inert (-400 mV) and H_2O_2-producing (-800 mV) electrode. The Compton group recently noted a 3-4 times smaller impact frequency in the presence of oxygen compared to the absence of oxygen, and tentatively attributed it to the Faradaic electrode reaction altering the mass transport of the particles.[34] However, as we observe a similar frequency regardless of a Faradaic reaction at the electrode, and qualitatively similar (3-4 times smaller than theory) frequencies in both the HER and ORR. While the electrochemical reaction occurring on the particle does not seem to affect the impact frequency, the underlying reason for small experimental frequencies remains unclear.

We used these results as a second way of calculating the EASA of the particles. Assuming the average 8.5 pA steady-state currents are due to the 4-electron reduction of oxygen to form water (as noted above, this is likely not strictly true), we calculated an EASA of 3.1×10^2 nm^2 per particle. This value is two orders of magnitude smaller than that previously calculated using the Volmer step, and an order of magnitude smaller than the geometric surface area. This is expected since the process is catalytic by nature and thus reflects events occurring only at the surface of the nanoparticles rather than in the interior of the nanoparticle, as in the case of hydrogen adsorption. Theoretically, under mass transfer limited reaction, an individual Pt NP with a radius of 15 nm should

produce currents of 12.5 pA and 25 pA via ORR for 2 e- and 4 e- processes, respectively (see Supporting Information). Further examination of the mean steady-state currents seen in Figure 2.4C indicates two-fold attenuation of the experimentally observed steady-state current compared with the theoretical prediction. The 50% "loss" of current can be attributed to either a negative kinetic effect,[34, 49, 50] i.e., decreased catalytic activity, or a partial particle dissolution/poisoning induced by the reaction intermediates.

Deactivation of Pt surfaces during the ORR is a well-known problem.[51, 52] Established explanations in the catalysis literature include poisoning by reactive intermediates, Pt dissolution, Ostwald ripening, and nanoparticle migration-aggregation.[52–56] Here, we measure current transients from individual particles, so we exclude Ostwald ripening and aggregation as deactivation mechanisms. Scanning transmission electron microscopy (STEM)[57] imaging of the particles before and after the ORR reveals no decrease in particle diameter after the ORR (Figure 2.16). While Pt deactivation has previously been attributed to poisoning by C- or O- containing species,[53, 58] energy dispersive x-ray spectroscopy (EDS) does not reveal significant build-up of these elements over the course of the ORR (Figure 2.17).

The nanoimpact results exhibit instantaneous steady-state currents (Figure 2.4A, B insets) and the steady-state current from the Pt microelectrode (Figure 2.4A inset) agrees with the predicted diffusional current (Supporting Information), suggesting that the smaller current is intrinsically due to the particles rather than a continual deactivation

process. We note that both O_2 and H_2O_2 reduction are similarly affected due to the similar attenuation in their currents.

2.5 Particle Detection on an Active Electrode

Reactions described thus far have been exclusively inner sphere. Outer-sphere reactions are not sensitive to the nature of the particle or the electrode, eliminating the constraints of material mismatch. We chose to use ruthenium (III) hexamine reduction as a model outer-sphere reaction. The formal potential of this reaction is the same on Au and Pt, as shown in Figure 2.18. As described above, the additional EASA added by a nanoparticle should cause an increase in current. No discernible steps could be resolved in the obtained chronoamperomograms (Figure 2.18). This is because the additional EASA is added within the electrode's diffusion layer, where there is already a low concentration of analyte. With a partially active electrode in the HER, the low proton concentration in the diffusion layer is not a problem because the Heyrovsky step can proceed via direct H_2O reduction, identical to the HER mechanism in basic solutions. A fully active electrode depletes the analyte concentration to the point that impact events do not cause detectable changes in current; this also holds when there is no kinetic difference between an inner-sphere reaction at a particle and at the electrode, as seen in Figures 2.10 and 2.15. Measurements using TEMPO as an outer-sphere anodic redox probe similarly did not reveal any stochastic collision events (Figure 2.19).

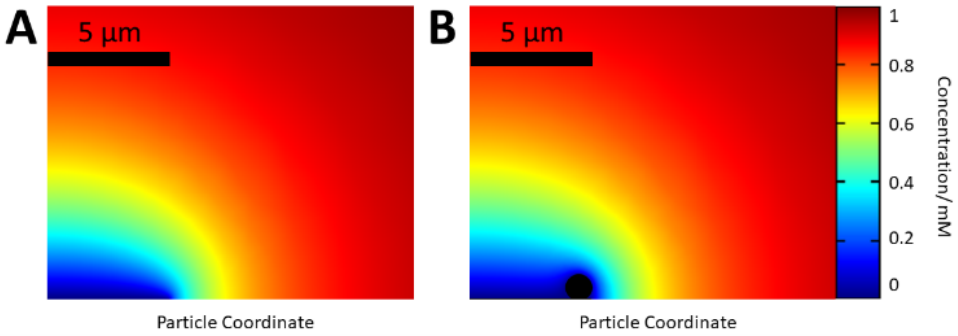

Figure 2.5: (A) Diffusion profile formed at a 5 μm radius electrode, 100 ms after electrode activation. (B) Perturbation of the diffusion profile by a catalytic particle (black diamond) 100 ms after the electrode is activated. The particle has radius 0.5 μm such that $r_{NP}/r_e = 0.1$.

We turned to numerical methods to determine the limits of detection in the outer-sphere case, at a fully active electrode. Simulations were performed using COMSOL Multiphysics (full details of the simulations can be found in the supporting information). An overview of the simulation space is shown in Figure 2.20. Briefly, a 5 μm radius electrode was defined as a region in a larger quarter-hemisphere simulation space. This configuration has previously been used to allow for 3-D simulations without requiring excessive computational power.[10, 59, 60] Simulated concentration gradients in the absence and presence of a catalytic particle are shown in Figure 2.5A and 2.5B, respectively. The particle was placed on the electrode midway between the "walls" of the simulation space, its radial distance from the electrode center is used as the particle coordinate (see inset, Figure 2.6A). As seen in Figure 2.5, a large ($r_{NP}/r_{elec} = 0.1$) catalytic particle sitting at the edge of the electrode causes a significant perturbation in the concentration gradient shortly after the reaction begins. The perturbation is far less significant over longer time scales and with smaller particles (Figure 2.21).

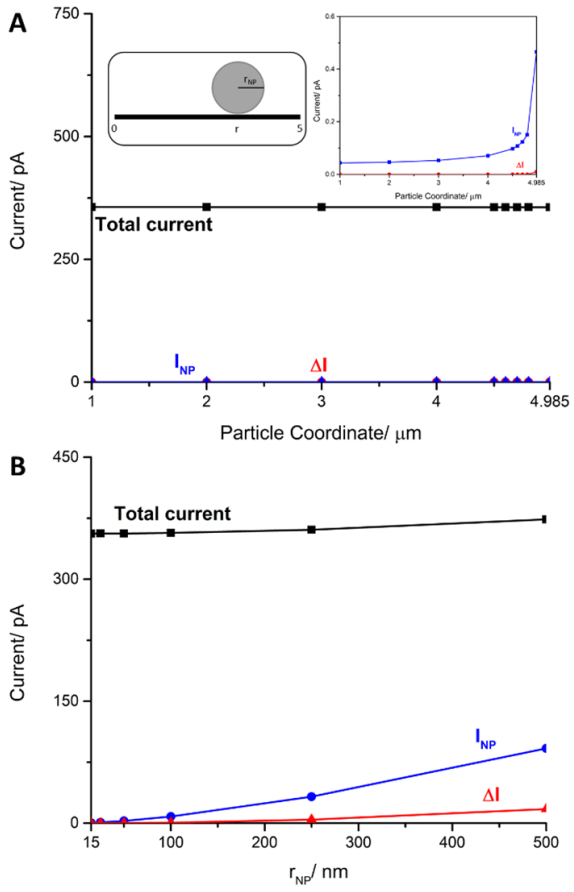

Figure 2.6: (A) Simulated steady-state current as a function of particle location using a 15 nm particle (r_{NP} = 15 nm) on a 5 μm radius electrode. The contribution of the catalytic particle to the total current (I_{NP}) is plotted in blue and the change in total current (ΔI) compared to the absence of the particle is plotted in red. (B) Simulated steady-state current as a function of particle radius. The particle is located r_{NP} away from the edge of a 5 μm radius electrode, such that r = 5 - r_{NP}. For readability, these data are recorded in Tables 2.7.7 and 2.7.7.

The limitations of active particle–active electrode collision detections were tested with a series of simulations, shown in Figure 2.6. Using a 15 nm radius particle to match experimental conditions, the change in current due to the particle (compared to the current in the absence of a particle) is nonzero only if the particle is placed 15 nm from the edge of the electrode (Figure 2.6A). In that case, the change in current is calculated to be 10 fA. This value is below our instrumental limit of detection, and we emphasize that experimental ΔI values would be four times smaller than this due to the simulation only accounting for one-quarter of the electrode surface.

It seems intuitively apparent that a catalytic particle with a radius on the order of the electrode radius would significantly increase the total current, as previously described by the Bard group,[61] so this result begged the question of the smallest particle detectable using an outer-sphere redox probe. Varying the particle radius (Figure 2.6B) while fixing its location at the electrode edge shows that a 250 nm particle is likely detectable on a typical 5 μm ultramicroelectrode ($r_{NP}/r_e = 0.05$). The simulated ΔI of 4 pA should yield an experimental response on the order of 1 pA, which is within our experimental limits. However, particles landing toward the center of the electrode would produce a lesser response due to the lower analyte flux to the electrode center. As well as being exceptionally difficult to resolve experimentally, this spatial effect would need to be decoupled from the effect of non-homogenous particle size in order to extract useful analytical information. Considering the limit of the minimal detectable particle size, the applicability of outer-sphere ECA detection schemes is severely limited. Despite this, particle impacts at

partially activated electrodes enable the investigation of a wider range of electrocatalysts by mitigating the limitation of material choice for relevant inner sphere reactions.

2.6 Conclusions

In summary, we have shown that active particle-–active electrode schemes can give deeper mechanistic insights than typical ECA-type measurements. In the hydrogen evolution reaction, the transition from current spikes to current steps at increasingly reducing potentials implies that electrode-generated hydrogen adsorbs to the Pt particle surface prior to impact. Deactivation of the Pt catalyst is attributed to hydrogen diffusion into the lattice; this effect is minimized when surface-bound hydrogen quickly reacts with species in solution. We demonstrate that competing electrochemical reactions, such as oxygen and hydrogen peroxide reduction, can be distinguished by the nature of particle collision transients; furthermore, the small ORR currents imply rapid activity degradation on the nanoscale. Experimental and computational results suggest that ECA schemes are still limited to inner-sphere reactions. This study demonstrates the potential of active or partially active electrodes in nanoimpact techniques as a tool to further probe the electrocatalytic properties of nanomaterials.

2.7 Supporting Information

2.7.1 Experimental

Citric acid (Sigma-Aldrich ≥99.5%), sodium citrate tribasic dehydrate (Sigma-Aldrich, ≥99.0%), sodium hydroxide (NaOH, Sigma-Aldrich, ≥98%), sodium phosphate monobasic (NaH_2PO_4, Sigma-Aldrich, ≥99.0%) , sodium phosphate dibasic (Na_2HPO_4, Sigma-Aldrich, ≥99.0%), potassium chloride (KCl, Sigma-Aldrich, ≥99.0%), ruthenium (III) hexamine chloride ($Ru(NH_3)_6Cl_3$, Sigma-Aldrich, 98%), TEMPO (Oakwood Chemical) , and citrate-capped 30 nm platinum nanoparticles (0.5 mg mL^{-1} in 2 mM citrate, Nanocomposix) were used as received. All solutions were prepared using deionized water purified to 18.2 $M\Omega\,cm^{-1}$ using a WaterPro BT purification system (Labconco). Gold, platinum, and carbon fiber ultramicroelectrodes were purchased from BASi. Electrodes were polished on 0.3 μm alumina pads for two minutes prior to each measurement. Electrode radii were measured electrochemically using ruthenium (III) hexamine reduction (Figure 2.18). The size distribution of the as-purchased Pt nanoparticles was confirmed using a FEI Tecnai G2 Sphera transmission electron micro-scope (Figure 2.8). The stability of the particles in water and the buffer solutions used in impact experiments was assessed using dynamic light scattering (Malvern Zetasizer Nano ZS, Figure 2.9). All electrochemical measurements were performed using a Biologic SP-300 potentiostat. A 50 kHz filter was applied, the sampling rate was 100 Hz. The electrochemical cell was placed in a well-grounded Faraday cage. A saturated

calomel electrode (SCE) was used as the reference and a platinum wire as the counter electrode. Cyclic voltammograms were recorded at a scan rate of 20 mV s^{-1} unless otherwise noted. For particle impact studies, 100 μL of Pt nanoparticle suspension (0.05 mg mL^{-1}) was added to 5 mL of buffer solution to yield a 6 pM particle suspension immediately before measurement. All measurements were carried out within 5 minutes of particle introduction to the solution in order to minimize aggregation effects.

As-purchased Pt nanoparticles were imaged using an FEI Technai G2 Sphera TEM operating at 200 kV in order to confirm the particle size and morphology. A sample was drop-cast onto a clean carbon-coated copper grid (Ted Pella Inc.) and allowed to air dry before being loaded on a single-tilt TEM holder. Bright-field TEM was performed with 2.84 μA filament (LaB_6) current, images were captured at 97kX magnification using a Gatan Ultrascan CCD camera. Particle sizing and chemical analysis pre- and post-ORR was performed using a Thermo-Fisher Talos G2 F200X operating at 200 kV in scanning transmission electron microscopy (STEM) mode. The sample preparation is described below. High angle annular dark field STEM (HAADF-STEM) was used for the analysis due to the high contrast between the Pt nanoparticles and the carbon support film. X-ray diffraction was collected on a Pt working electrode using a Rigaku Smartlab equipped with a HyPix detector in the Bragg-Brentano ($\theta/2\theta$) optics configuration. The x-ray source was Cu Kα, the size of the beam was set using a 2.5° soller slit, a 1/8-degree incident slit, and a 2 mm length limiting slit. The electrode sample was mounted using a homemade sample holder. The receiving optics were a Kβ filter followed by a 20 mm

receiving slit and a 2.5° soller slit. The detector was operated in 1D scanning mode. Diffraction data was collected from 35-50° with a 0.02° step size and a scan speed of 1° min^{-1}.

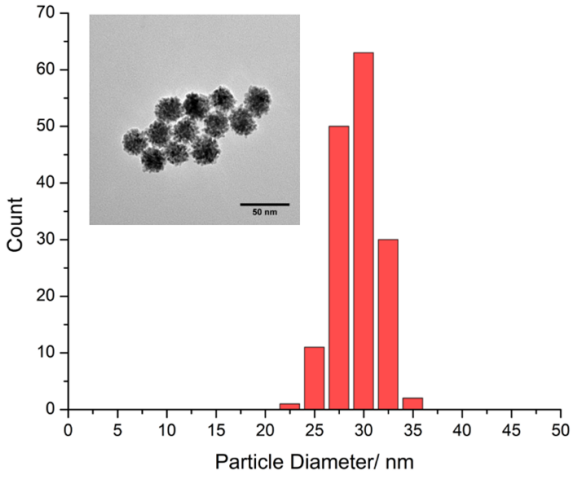

Figure 2.7: Pt nanoparticle morphology and size distribution (29.4 ± 2.4 nm) obtained by TEM (N = 157).

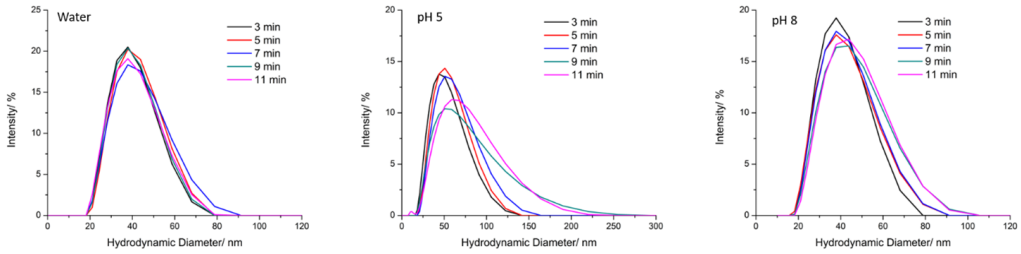

Figure 2.8: Pt nanoparticle size distribution obtained using dynamic light scattering as a function of time in solution. 100 μL of Pt nanoparticle suspension (0.5 mg min^{-1}) was added to 1 mL of water or buffer solution immediately prior to measurement. Minimal aggregation is seen in pH 8 phosphate buffer (right). Aggregation is more significant in pH 5 citrate buffer (center). The particles are stable in neutral, 18.2 MΩ cm-1 water (left).

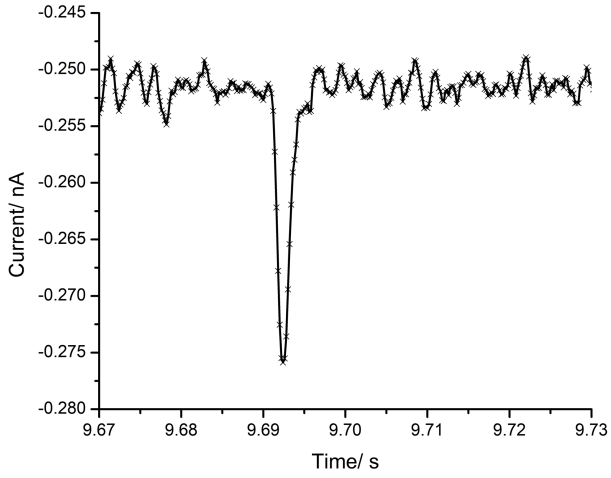

Figure 2.9: Raw data from a chronoamperomogram of a Pt nanoparticle impacting an Au microelectrode (radius 5.84 μm) biased at -300 mV vs SCE in nitrogen-purged, 20 mM, pH 5 citrate. The data were sampled at 5 kHz, revealing that the pseudocapacitive charging occurs within 5 ms.

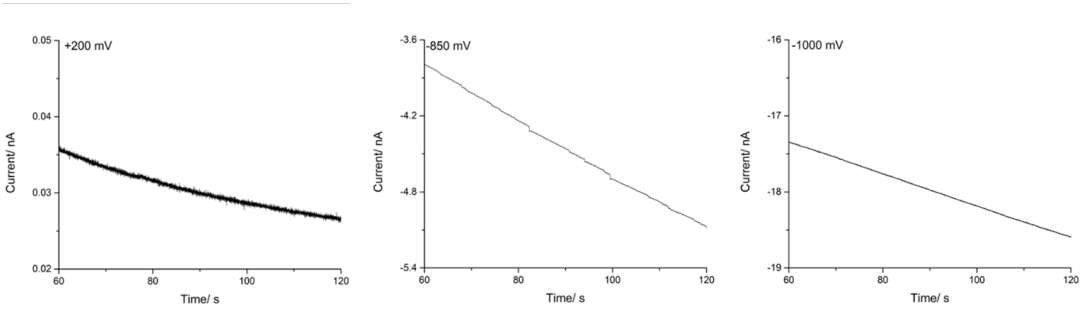

Figure 2.10: Chronoamperomograms of Pt nanoparticles (30 nm diameter, 6 pM) impacting an Au electrode (radius 5.84 μm) in nitrogen-purged, 20 mM, pH 5 citrate. The electrode was biased at +200 mV vs SCE as a control; no events are observed because this potential is in-sufficient to drive any reaction on impacting Pt particles (left). Infrequent steps are seen at -850 mV due to the Heyrovsky step of the HER, as discussed in the text (center). No events are observed at -1000 mV because the electrode surface is depleted of protons, impacting particles do not catalyze any additional electrochemical reactions (right).

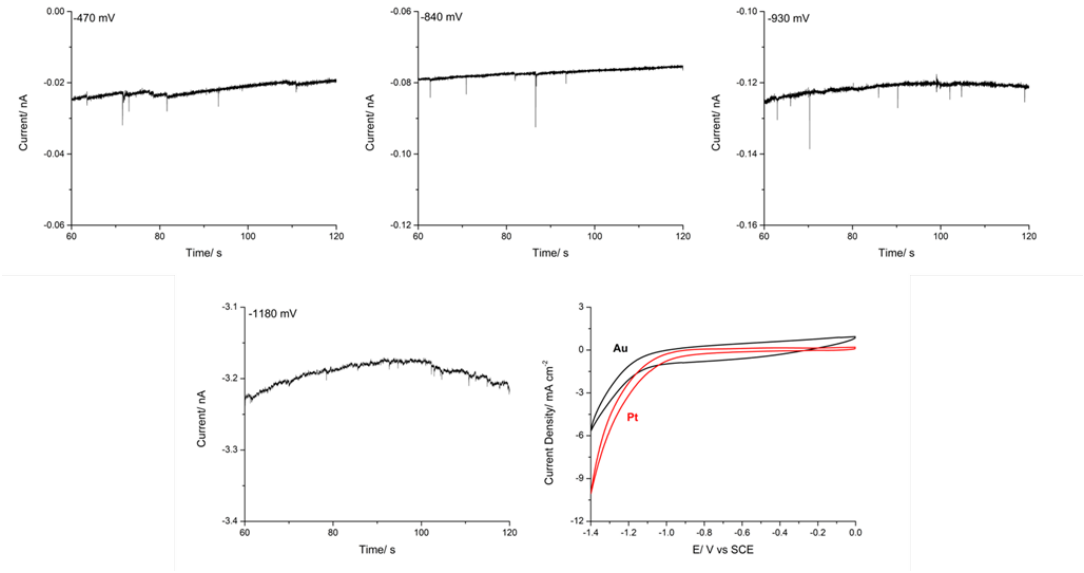

Figure 2.11: Chronoamperomograms of Pt nanoparticles (30 nm diameter, 6 pM) impacting an Au electrode (radius 5.84 μm) in 20 mM, pH 8.2 nitrogen purged phosphate buffer. Spikes persist at much higher potentials in basic conditions compared to acidic conditions, likely because hydrogen adsorption is the rate-limiting step of the HER in alkaline solutions.[31]

In addition to measuring nanoimpacts via the HER in acidic (pH 5) conditions, we performed the same measurements in alkaline condi-tions. 20 mM phosphate buffer (pH 8.2) was purged with N2 and used in the place of the citrate buffer. Electrode potentials were such that each potential is approximately 180 mV negative of the potential used in acidic solutions, due to the Nernstian shift with pH.

2.7.2 Particle Impact Frequency Calculation

The theoretical impact event frequency can be calculated by assuming purely Brownian motion as outlined by Shoup and Szabo.[32] The nanoparticles' diffusion coefficient

Reaction	Electrode	Buffer	Potential	N	Impacts/min (Theory)	Impacts/min (Experiment)
HER	Au	Citrate, pH 5, 20 mM	-300 mV	124	89	25 ± 8
HER	Au	Citrate, pH 5, 20 mM	-660 mV	117	89	23 ± 9
HER	Au	Citrate, pH 5, 20 mM	-750 mV	113	89	23 ± 10
HER	Au	Citrate, pH 5, 5 mM	-660 mV	135	89	27 ± 7
ORR	C	Phosphate, pH 8, 20 mM	-400 mV	100	62	20 ± 7
ORR	C	Phosphate, pH 8, 20 mM	-800 mV	89	62	18 ± 3

Table 2.1: Calculated and observed particle impact frequencies. All frequencies were measured using a 6 pM particle concentration. Experi-mental results are the average ± standard deviation of five independent, 1-minute chronoamperomograms. After particle injection, the suspensions were agitated by 10-15 s of either N2 bubbling (for the HER) or sonication (for the ORR) in order to assure good dispersal in the buffer. For the HER, the citrate buffer was bubbled with N2 for 20 minutes prior to particle injection.

is first calculated using the Stokes-Einstein equation,[62] taking the viscosity of water as 8.9×10^{-4} Pa s at 25 ℃:

$$D = \frac{k_B T}{6\pi\eta r_{NP}} \tag{2.6}$$

Application of 2.6 yields $D = 1.63 \times 10^{-11} m^2 s^{-1}$. We then calculate the expected particle impact frequency for the Au (re = 5.84 μm) and C (re = 4.21 μm) microelectrodes used in this study. The theoretical results are included with the experimentally observed frequencies in Table 2.7.2.

2.7.3 Electroactive Surface Area Calculations

Pt nanoparticle surface areas were calculated in two ways. From the spikes attributed to the Volmer step, we assume a monolayer of hydrogen forms on impacting particles,

with a surface coverage of 77%. An ideal monolayer of H has a surface charge of 210 μC cm^{-2} on polycrystalline Pt.[35]

$$EASA = \frac{45fC}{0.77 \times 210\mu C cm^{-2}} = 2.8 \times 10^4 nm^2 \tag{2.7}$$

For comparison, the surface area of a smooth, 15 nm radius sphere is 2.8×10^3 nm^2.

2.7.4 Steady State Diffusional Current Calculations

The current response to particle impacts in Figure 2.7D appears to be limited by mass transfer. We calculated the limiting currents to a 15 nm radius sphere on a planar surface.[62] The current may be limited by the diffusion of either hydronium or diprotic citric acid to the electrode, or by diffusion of hydrogen gas away from the electrode. In Equation 2.8, n is the number of electrons transferred (2), F is Faraday's constant, D is the diffusion coefficient of the diffusion-limiting species, C is the concentration of that species, and r is the radius of the electrode (15 nm).

$$I = 4\pi \ln 2nFDCr \tag{2.8}$$

$$pH = pK_a + \log \frac{A^-}{HA} \tag{2.9}$$

Proton diffusion: The concentration of protons (hydronium ions) in the pH 5 solution is 10^-5 M. The diffusion coefficient of protons is around 9.3×10^{-9}m^{2}s^{-1}.[63] Considering Equation 2.8, $I_{H^+} = 2.3pA$

Citric acid diffusion: The proton source for the HER may be protonated citric acid. We first calculate the concentration of diprotic citric acid considering the pH of 5, its $pK_{a,2}$ value of 4.76,[64] and the total citrate concentration of 20 mM. Considering Equation 2.9, we find that $[H_2A^-] = 7.3mM$. Considering the diffusion coefficient of diprotic citric acid as $5.39 \times 10^{-10}\ m^2 s^{-1}$, $I_{H_2cit^-} = 99pA$.

Hydrogen diffusion: The mass transfer limit may also be due to the diffusion of the product, hydrogen, away from the electrode as previously reported for the oxygen evolution reaction.[37] The diffusion coefficient of hydrogen in aqueous solutions is approximately 1.92×10^{-9} m^2 s^{-1},[65] its solubility is 17.4 μL H_2 (at STP)/ mL H_2O (equivalently, 7.1 $\times 10^{-4}$ M).[66] This calculation represents a lower limit on the diffusional H_2 current, as supersaturation of the solution would effectively increase the mass transport of H_2. Evaluation of Equation 2.8 yields $I_{H_2} = 81\ pA$. We note that this assumes no H_2 gas bubble formation. Bubble formation is unlikely in this case, for reasons similar to those outlined by Liang et al.[27] The effective proton concentration in this study (at most 7.3 mM based on citric acid) is orders of magnitude lower than the 1 M $HClO_4$ used by Chen and Luo to generate H_2 bubbles on planar electrodes or the 0.25 M H_2SO_4 used by Chen, Luo, and White at recessed electrodes.[15, 67] Examples of gas bubble formation in the literature rely on high analyte concentrations in order to achieve supersaturation,[68] the low analyte concentrations in this work make H_2 supersaturation (and thus, H_2 bubble formation) highly improbable.

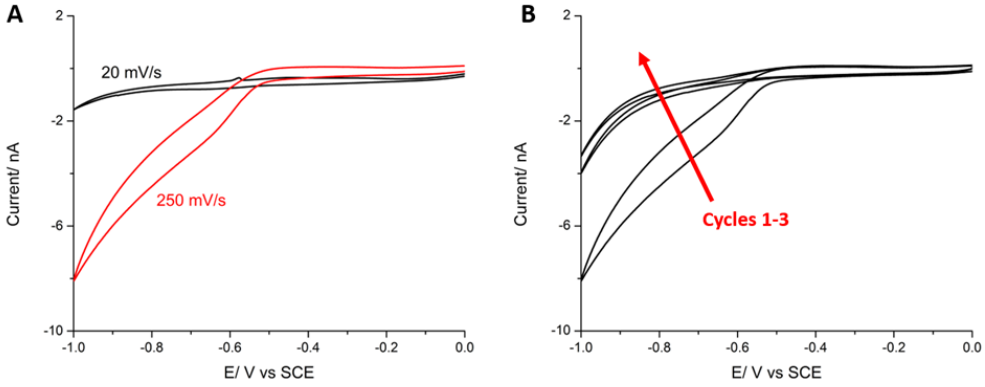

Figure 2.12: Cyclic voltammograms of a Pt microelectrode (radius 4.59 μm) in nitrogen-purged, 20 mM, pH 5 citrate buffer. Electrode deactivation is shown by the smaller currents recorded at 20 mV/s compared to 250 mV/s. (B) Successive cyclic voltammograms recorded at 250 mV/s. Significant electrode deactivation is observed in the second and third cycles; the fast scan rate minimizes deactivation in the first cycle. The cathodic sweep of the first cycle was used as the linear sweep voltammogram of the Pt electrode in Figure 2.7A.

2.7.5 Steady State Currents in ORR

The steady-state current for a 15 nm radius sphere, on a flat surface, catalyzing the ORR was also calculated using Equation 2.8.[62] The diffusion coefficient of oxygen is 1.9×10^{-9} m^2 s^{-1},[69] the concentration of O_2 in a solution under ambient atmosphere (21% O_2) is 260 μM.[45] For the 4-electron reduction from O_2 to water, $I = 25pA$.

$$I_{disk} = 4nFDCr \tag{2.10}$$

The steady-state current on the r = 4.59 μm Pt microelectrode is also calculated to be 3.5 nA using Equation 2.10.

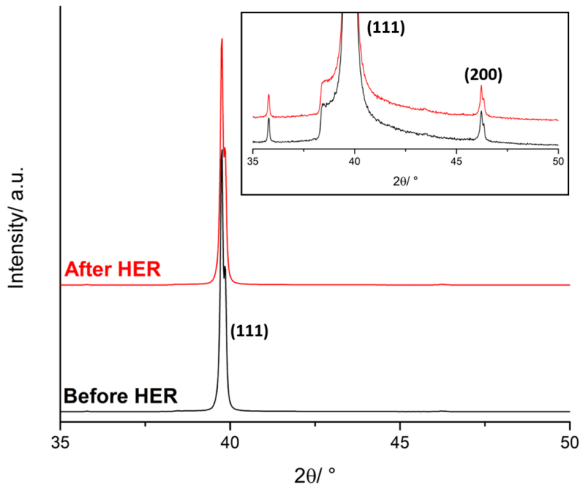

Figure 2.13: X-ray diffraction patterns of a 2 mm diameter Pt working electrode before (black) and after (red) it was used in the HER. After the initial diffraction pattern was collected the electrode was submerged in nitrogen-purged, 20 mM, pH 5 citrate buffer and biased at -660 mV vs SCE for 5 minutes; a second diffraction pattern was collected immediately after the electrochemistry. Pt (111) remains at 39.75° and Pt (200) remains at 46.22° after electrochemical treatment, no peak broadening is observed. The small peak at 35.78° visible in the inset is due to the small fraction of unfiltered Cu Kβ radiation.

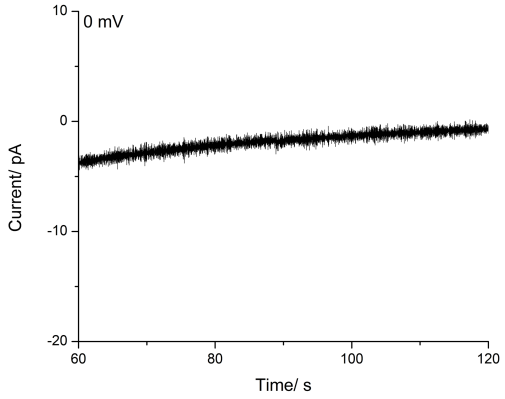

Figure 2.14: Chronoamperomogram of Pt nanoparticles (30 nm diameter, 6 pM) impacting a C microelectrode (radius 4.21 μm) biased at 0 mV vs SCE in pH 8.2, air-saturated phosphate solution. No impact events are visible at this potential.

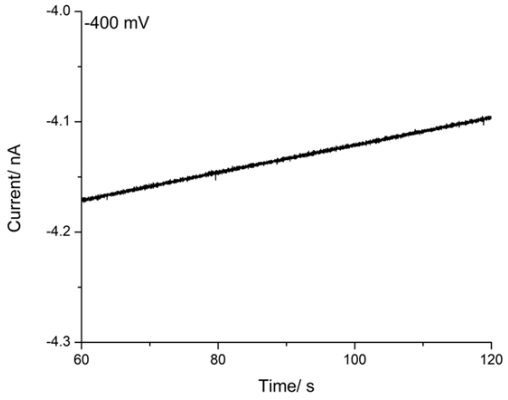

Figure 2.15: Chronoamperomogram of Pt nanoparticles (30 nm diameter, 6 pM) impacting a Pt microelectrode (radius 4.59 μm) biased at -400 mV vs SCE in pH 8.2, air-saturated 20 mM phosphate solution.

2.7.6 STEM Images of Pt NPs pre- and post-ORR

We quantified particle degradation during the ORR via ex-situ STEM imaging. A carbon coated copper TEM grid was drop-cast with Pt NP suspension (0.05 mg min^{-1}) to serve as a control, without electrochemical treatment. For the electrochemically treated particles, we adopted a technique described by Feliu and Abruña.[57] A copper wire was poked through a carbon coated copper TEM grid to create a small hole. The wire was removed and the grid was drop-cast with Pt nanoparticle suspension. After drying overnight, the wire was inserted through the grid and connected to our potentiostat. The grid was immersed in air-saturated, 20 mM, pH 8 phosphate buffer and biased at -400 mV vs SCE for 5 minutes to drive the ORR.

In the absence of electrochemical treatment, the average particle diameter was found to be 32.4 ± 2.4 nm by STEM (N = 90). After the ORR, the average particle diameter was

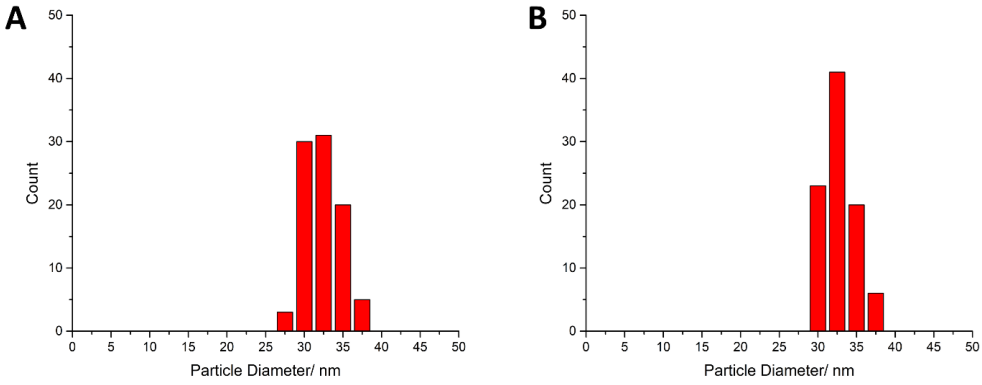

Figure 2.16: Distribution of the Pt NP diameters measured before (A) and after (B) the oxygen reduction reaction. Both histograms have N = 90. The average diameter in A is 32.4 ± 2.4 nm, the average diameter in B is 32.8 ± 2.0 nm.

32.8 ± 2.0 nm (N = 90). Furthermore, elemental mapping does not reveal any significant difference in the concentrations of platinum, carbon, or oxygen in the particles before and after the ORR (Figure 2.17).

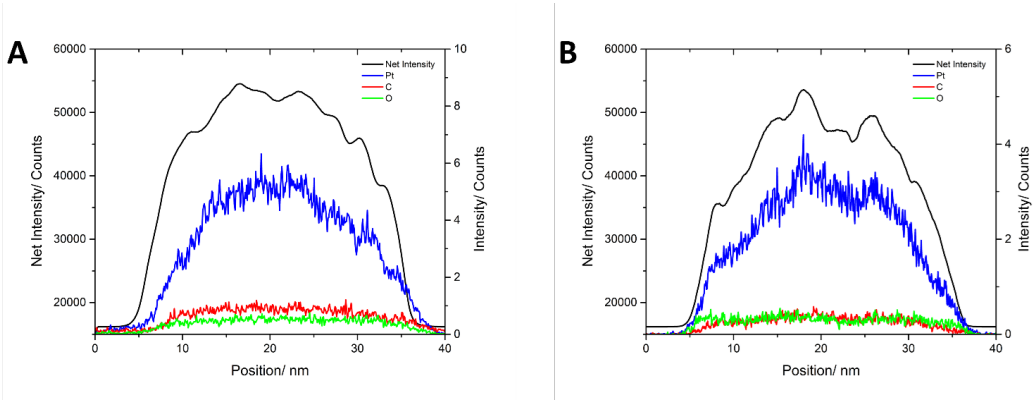

Figure 2.17: Energy-dispersive x-ray (EDX) line spectra of individual Pt NPs before (A) and after (B) the ORR.

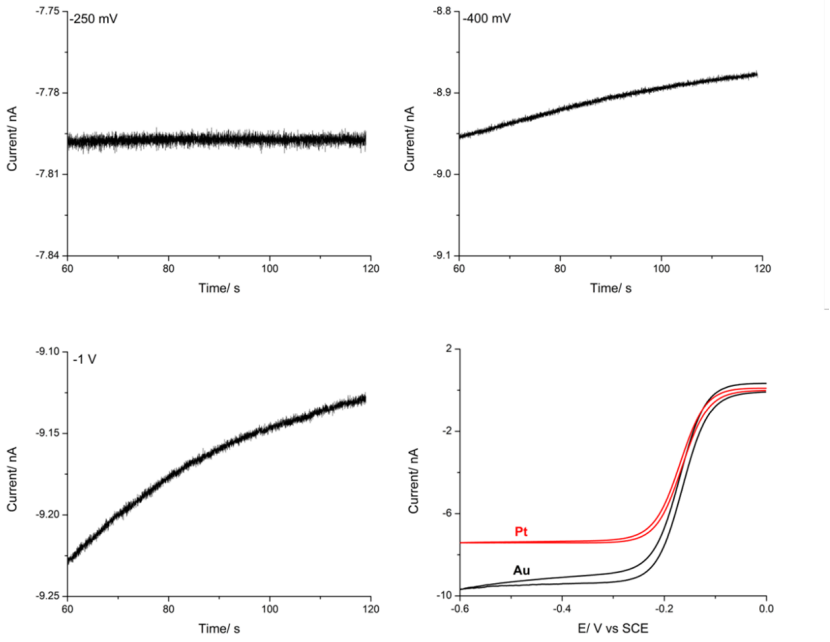

Figure 2.18: Chronoamperomograms of Pt nanoparticles (30 nm diameter, 6 pM) impacting an Au electrode (radius 5.84 μm) in a nitrogen-purged solution of 5 mM $Ru(NH_3)_6Cl_3$ in 20 mM KCl. The current at the Au electrode is larger than at the Pt electrode (bottom right) due to the larger radius of the Au electrode, as shown below.

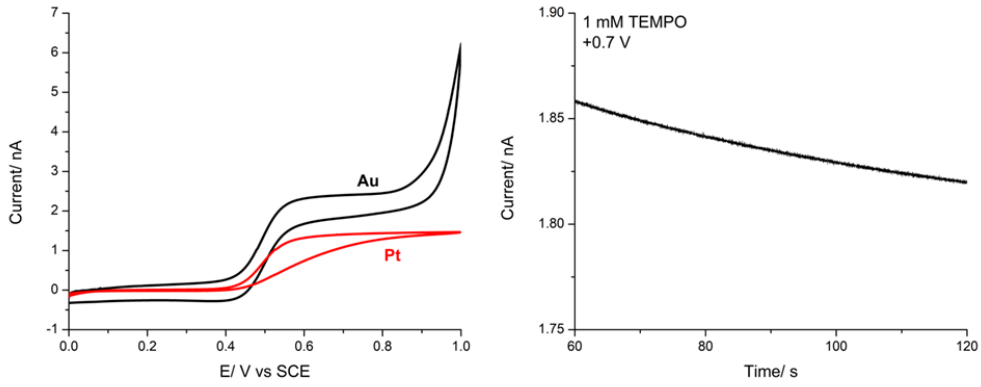

Figure 2.19: Left: CVs of Au and Pt UMEs in 1 mM TEMPO, 20 mM KCl. Right: Chronoamperomogram of Pt nanoparticles (30 nm diameter, 6 pM) impacting an Au electrode biased at 700 mV vs SCE in a 1 mM TEMPO solution, supported by 20 mM KCl.

2.7.7 Finite Element Simulations

Numerical simulations were performed using the commercially available finite element analysis package, COMSOL 5.5. Simulations were performed on a PC equipped with 16 GB of RAM and a 2.90 GHz Intel Core i7 CPU.

Simulations were performed using a quarter-hemispherical geometry in order to minimize computation time for three-dimensional simulations. An overview of the simulation geometry is shown in Figure 2.20. A quarter-circle with radius re is defined as the electrode surface (region 1). Region 3 is a quarter hemisphere with radius $10r_e$ and is used to define the simulation volume. Through 2D simulations in larger geometries, we found that this distance was sufficient to avoid the diffusion layer reaching the simulation border. A second quarter hemisphere (region 2, $r = 11r_e$) was used to define the bulk concentration boundary condition using an infinite element domain. This approach

mimics strategies employed in similar systems.[10, 70] A nanoparticle was simulated using a sphere with radius r_{NP}. The sphere was placed on the electrode surface as shown in Figure 2.20B, equidistant from the "walls" of the simulation and with its center located r_{NP} above the electrode surface (such that there is a point contact between the particle and the electrode). When needed, the particle location was varied along the red line shown in Figure 2.20B: the particle coordinate refers to the distance between the center of the particle and the center of the electrode (the corner of the simulation space).

The COMSOL "electroanalysis" and "transport of dilute species" modules were used to define boundary conditions. No-flux conditions were applied to region 3 and, if applicable, the particle surface. The $Ru(NH_3)_6^{3+}$ concentration was set equal to its bulk concentration (1 mM) in region 2, an infinite element domain. The initial concentration of $Ru(NH_3)_6^{3+}$ in the entire simulation space was set to 1 mM, the initial concentration of $Ru(NH_3)_6^{2+}$ was set to 0. Electrode surfaces were defined as region 1 (Figure 2.20A) and, if applicable, the particle surface. The electrode potential was set 0.4 V negative of the formal $Ru(NH_3)_6^{3+}$ reduction potential in order to achieve a mass transport limited current. Mass transport was solved for using Fick's second law. Finite element simulations are highly sensitive to the chosen mesh. We adopted a strategy established by the Renault group in order to maintain a consistent mesh in the presence and in the absence of a nanoparticle.[10] In both cases, the nanoparticle sphere is drawn in the simulation space. Its surface is used to define a finer mesh in its vicinity, described in more detail below. For simulations in the presence of a catalytic particle, we applied the

"thin impermeable layer" and "electrode surface" boundary conditions to the surface of the sphere. This applies a no-flux boundary condition to the particle and lets us define an electrochemical reaction on the particle surface. These boundary conditions are not applied in the absence of the particle, maintaining the same mesh while allowing flux through the sphere.

The simulation space was meshed using the default tetrahedral mesh with "fine" element sizing. This was chosen because simulations performed with the next-finer element sizing ("finer") yielded steady-state currents within 1% of the "fine" mesh. Two additional constraints were imposed in order to achieve a finer mesh near the electrode and particle surfaces. At the particle surface, the maximum element size was restricted to $r_{NP}/10$. At the electrode surface, the maximum element size was restricted to $r_e/100$ and the maximum element growth rate was set to 1.05. We found that this mesh gave consistent, physically interpretable results while minimizing computation time. We solved for stationary solutions, representing steady-state currents. Typical studies solved for approximately 300,000 degrees of freedom. ΔI values shown here and in the main text represent the change in steady-state current before and after the no-flux and electrode surface boundary conditions are applied to the surface of the sphere. Because the sphere and the electrode are defined by two separate "electrode surface" boundary conditions, we can determine the current through each independently and thus determine the particle's contribution (I_{NP}) to the total current.

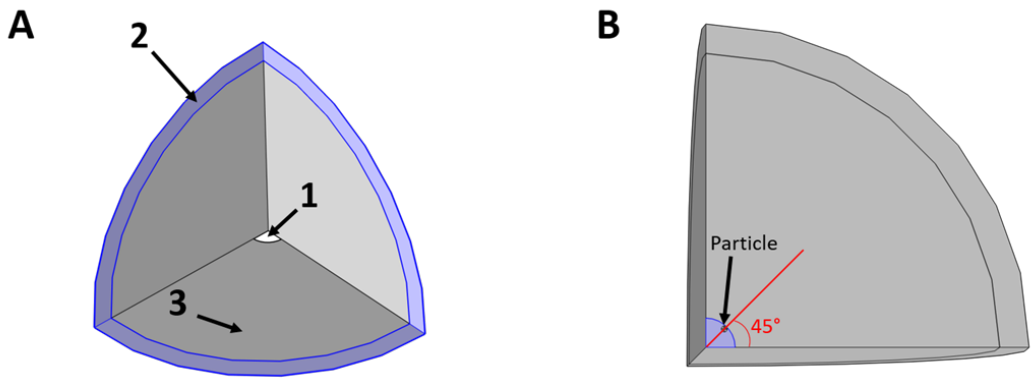

Figure 2.20: (A) Overview of the simulation geometry. Region 1 is the electrode surface; region 2 is an infinite element domain to which a bulk concentration boundary condition is applied; region 3 forms the borders of the simulation space with a no-flux boundary condition. (B) Top-down view. The nanoparticle is placed on the electrode surface, equidistant from the "walls" of the simulation.

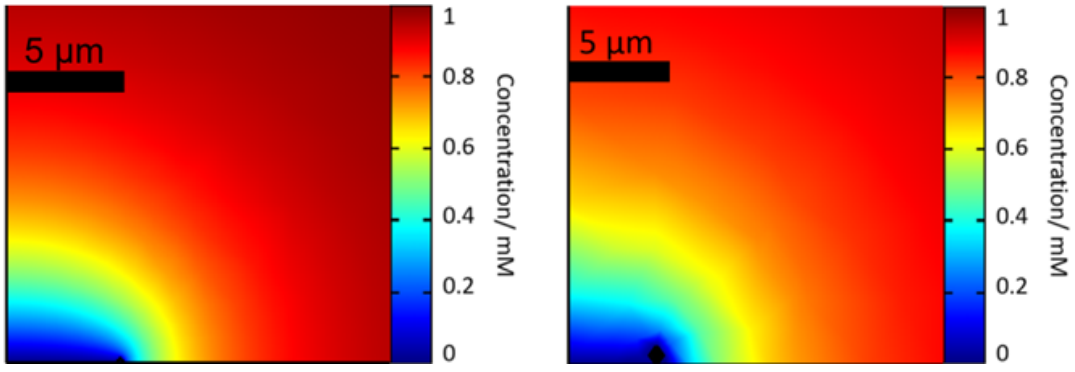

Figure 2.21: (Left) Diffusion profile simulated for a 100 nm nanoparticle after 100 ms. The particle has a minimal effect on the shape and size of the diffusion layer. (Right) Diffusion profile simulated for a 500 nm nanoparticle 1 second after electrode activation.

Particle Coordinate/ μm	Total Current/ pA	I_{NP}/ pA	ΔI/ pA
1	356.64	0.04330	0
2	356.5	0.04330	0
3	356.38	0.04629	0
4	356.32	0.05307	0
4.5	356.19	0.07080	0
4.6	356.14	0.09700	0
4.7	356.03	0.10773	0
4.8	356.36	0.12342	0
4.985	356.06	0.46548	0.01

Table 2.2: Simulated current as a function of particle location. The particle radius is 15 nm and the electrode radius is 5 μm.

Particle Size/ nm	Total Current/ pA	I_{NP}/ pA	ΔI/ pA
15	356.07	0.46548	0.01
25	356.28	1.0088	0.04
50	356.26	2.8748	0.17
100	356.96	8.1930	0.68
250	360.76	32.628	4.31
500	373.55	92.013	17.38

Table 2.3: Simulated current as a function of particle size. The particle is located r_{NP} away from the edge of a 5 μm radius electrode, such that $r = 5 - r_{NP}$

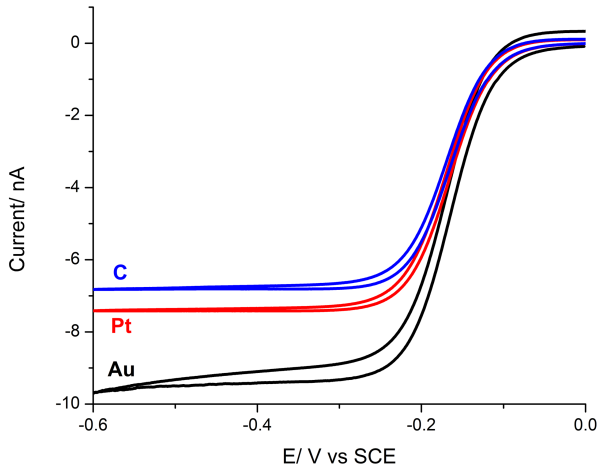

Figure 2.22: $Ru(NH_3)_6Cl_3$ reduction at Au (black), Pt (red) and C (blue) ultramicroelectrodes with 20 mM KCl supporting electrolyte. Electrode radii were calculated using the measured steady-state current at -0.4 V vs SCE.

2.7.8 Electrode Size Measurements

Electrode radii were measured electrochemically using $Ru(NH_3)_6Cl_3$ reduction. CVs were recorded at 20 mV/s in a solution of 4.971 mM $Ru(NH_3)_6Cl_3$ supported by 20 mM KCl. Taking the diffusion coefficient for $Ru(NH_3)_6Cl_3$ as 8.43×10^{-10} m^2 s^{-1},[71] the electrode radii were calculated using Equation 2.10. The electrode radii were measured for the Au (5.84 μm), Pt (4.59 μm), and C (4.21 μm) ultramicroelectodes used in this work.

References

[1] T. J. Anderson, B. Zhang, *Accounts of Chemical Research* **2016**, *49*, 2625–2631.

[2] S. M. Oja, Y. Fan, C. M. Armstrong, P. Defnet, B. Zhang, *Analytical Chemistry* **2016**, *88*, 414–430.

[3] N. V. Rees, *Electrochemistry Communications* **2014**, *43*, 83–86.

[4] J. Clausmeyer, W. Schuhmann, *TrAC - Trends in Analytical Chemistry* **2016**, *79*, 46–59.

[5] L. A. Baker, *Journal of the American Chemical Society* **2018**, *140*, 15549–15559.

[6] S. Goines, J. E. Dick, *Journal of The Electrochemical Society* **2020**, *167*, 037505.

[7] Y. Fang, H. Wang, H. Yu, X. Liu, W. Wang, H. Y. Chen, N. J. Tao, *Accounts of Chemical Research* **2016**, *49*, 2614–2624.

[8] P. Li, Q. He, H. X. Liu, Y. Liu, J. J. Su, N. Tian, D. Zhan, *ChemElectroChem* **2018**, *5*, 3068–3072.

[9] K. Tschulik, B. Haddou, D. Omanović, N. V. Rees, R. G. Compton, *Nano Research* **2013**, *6*, 836–841.

[10] C. Renault, S. G. Lemay, *ChemElectroChem* **2019**, 69–73.

[11] W. Yu, C. Batchelor-Mcauley, Y. C. Wang, S. Shao, S. M. Fairclough, S. J. Haigh, N. P. Young, R. G. Compton, *Nanoscale* **2019**, *11*, 17791–17799.

[12] X. Jiao, C. Batchelor-McAuley, N. P. Young, R. G. Compton, *Physical Chemistry Chemical Physics* **2018**, *20*, 23847–23850.

[13] J. M. Kahk, N. V. Rees, J. Pillay, R. Tshikhudo, S. Vilakazi, R. G. Compton, *Nano Today* **2012**, *7*, 174–179.

[14] X. Jiao, C. Lin, N. P. Young, C. Batchelor-McAuley, R. G. Compton, *Journal of Physical Chemistry C* **2016**, *120*, 13148–13158.

[15] Q. Chen, L. Luo, *Langmuir* **2018**, *34*, 4554–4559.

[16] W. Cheng, R. G. Compton, *TrAC - Trends in Analytical Chemistry* **2014**, *58*, 79–89.

[17] S. V. Sokolov, S. Eloul, E. Kätelhön, C. Batchelor-McAuley, R. G. Compton, *Physical Chemistry Chemical Physics* **2017**, *19*, 28–43.

[18] Y. G. Zhou, N. V. Rees, R. G. Compton, *Angewandte Chemie - International Edition* **2011**, *50*, 4219–4221.

[19] X. Xiao, A. J. Bard, *Journal of the American Chemical Society* **2007**, *129*, 9610–9612.

[20] Y. Xiao, F. R. F. Fan, J. Zhou, A. J. Bard, *Journal of the American Chemical Society* **2008**, *130*, 16669–16677.

[21] B. M. Quinn, P. G. V. '. Hof, S. G. Lemay, *Journal of the American Chemical Society* **2004**, *126*, 8360–8361.

[22] J. E. Dick, C. Renault, A. J. Bard, *Journal of the American Chemical Society* **2015**, *137*, 8376–8379.

[23] P. A. Defnet, C. Han, B. Zhang, *Analytical Chemistry* **2019**, *91*, 4023–4030.

[24] R. A. Thearle, Z. Sofer, D. Bouša, M. Pumera, *ChemPhysChem* **2016**, 2096–2099.

[25] D. Öhl, J. Clausmeyer, S. Barwe, A. Botz, W. Schuhmann, *ChemElectroChem* **2018**, *5*, 1886–1890.

[26] L. Chen, C. Lin, R. G. Compton, *Physical Chemistry Chemical Physics* **2018**, *20*, 15795–15806.

[27] Z. P. Xiang, H. Q. Deng, P. Peljo, Z. Y. Fu, S. L. Wang, D. Mandler, G. Q. Sun, Z. X. Liang, *Angewandte Chemie - International Edition* **2018**, *57*, 3464–3468.

[28] M. C. Tavares, S. A. S. Machado, L. H. Mazo, *Electrochimica Acta* **2001**, *46*, 4359–4369.

[29] J. O. Bockris, S. U. Khan, *Surface Electrochemistry: A Molecular Level Approach*, Plenum Press, **1993**.

[30] E. Santos, P. Hindelang, P. Quaino, E. N. Schulz, G. Soldano, W. Schmickler, *ChemPhysChem* **2011**, *12*, 2274–2279.

[31] I. Ledezma-Yanez, W. D. Z. Wallace, P. Sebastián-Pascual, V. Climent, J. M. Feliu, M. T. M. Koper, *Nature Energy* **2017**, *2*, 1–7.

[32] D. Shoup, A. Szabo, *Journal of Electroanalytical Chemistry* **1982**, *140*, 237–245.

[33] S. E. F. Kleijn, S. C. S. Lai, T. S. Miller, A. I. Yanson, M. T. M. Koper, P. R. Unwin, *Journal of the American Chemical Society* **2012**, *134*, 18558–18561.

[34] X. Chang, C. Batchelor-mcauley, R. G. Compton, *Chemical Science* **2020**, *11*, 4416–4421.

[35] M. Lukaszewski, M. Soszko, A. Czerwiński, *International Journal of Electrochemical Science* **2016**, *11*, 4442–4469.

[36] X. Jiao, E. E. L. Tanner, S. V. Sokolov, R. G. Palgrave, N. P. Young, R. G. Compton, *Physical Chemistry Chemical Physics* **2017**, *19*, 13547–13552.

[37] A. E. Arrassi, Z. Liu, M. V. Evers, N. Blanc, G. Bendt, S. Saddeler, D. Tetzlaff, D. Pohl, C. Damm, S. Schulz, K. Tschulik, *Journal of the American Chemical Society* **2019**, *141*, 9197–9201.

[38] S. Daniele, I. Lavagnini, M. A. Baldo, F. Magno, *Analytical Chemistry* **1998**, *70*, 285–294.

[39] M. W. Glasscott, J. E. Dick, *Analytical Chemistry* **2018**, *90*, 7804–7808.

[40] B. M. Ahern, L. D. Burke, D. P. Casey, M. A. Horgan, L. M. Hurley, A. P. O'Mullane in Hydrogen at Surfaces and Interfaces: Proceedings of the International Symposium, **2000**, pp. 209–218.

[41] E. Gileadi, M. A. Fullenwider, J. O. Bockris, *Journal of The Electrochemical Society* **1966**, *113*, 926.

[42] N. M. Marković, H. A. Gasteiger, P. N. Ross, *Journal of Physical Chemistry* **1996**, *100*, 6715–6721.

[43] H.-H. Yang, R. L. McCreery, *Journal of The Electrochemical Society* **2000**, *147*, 3420.

[44] H. Zhang, C. Lin, L. Sepunaru, C. Batchelor-McAuley, R. G. Compton, *Journal of Electroanalytical Chemistry* **2017**, *799*, 53–60.

[45] *Oxygen and Ozone: Solubility Data Series*, (Ed.: R. Battino), Elsevier Science, **2015**.

[46] R. Chen, C. Yang, W. Cai, H.-Y. Wang, J. Miao, L. Zhang, S. Chen, B. Liu, *ACS Energy Letters* **2017**, *2*, 1070–1075.

[47] A. Schneider, L. Colmenares, Y. E. Seidel, Z. Jusys, B. Wickman, B. Kasemo, R. J. Behm, *Physical Chemistry Chemical Physics* **2008**, *10*, 1931.

[48] M. Rouhet, S. Bozdech, A. Bonnefont, E. R. Savinova, *Electrochemistry Communications* **2013**, *33*, 111–114.

[49] M. Nesselberger, S. Ashton, J. C. Meier, I. Katsounaros, K. J. J. Mayrhofer, M. Arenz, *Journal of the American Chemical Society* **2011**, *133*, 17428–17433.

[50] M. Shao, A. Peles, K. Shoemaker, *Nano Letters* **2011**, *11*, 3714–3719.

[51] S. Cherevko, N. Kulyk, K. J. J. Mayrhofer, *Nano Energy* **2016**, *29*, 275–298.

[52] R. Borup, J. Meyers, B. Pivovar, Y. S. Kim, R. Mukundan, N. Garland, D. Myers, M. Wilson, F. Garzon, D. Wood, P. Zelenay, K. More, K. Stroh, T. Zawodzinski, J. Boncella, J. E. McGrath, M. Inaba, K. Miyatake, M. Hori, K. Ota, Z. Ogumi, S. Miyata, A. Nishikata, Z. Siroma, Y. Uchimoto, K. Yasuda, K. I. Kimijima, N. Iwashita, *Chemical Reviews* **2007**, *107*, 3904–3951.

[53] J. Ustarroz, I. M. Ornelas, G. Zhang, D. Perry, M. Kang, C. L. Bentley, M. Walker, P. R. Unwin, *ACS Catalysis* **2018**, *8*, 6775–6790.

[54] J. H. Bae, R. F. Brocenschi, K. Kisslinger, H. L. Xin, M. V. Mirkin, *Analytical Chemistry* **2017**, *89*, 12618–12621.

[55] S. J. Percival, J. E. Dick, A. J. Bard, *Analytical Chemistry* **2017**, *89*, 3087–3092.

[56] J. M. Noël, Y. Yu, M. V. Mirkin, *Langmuir* **2013**, *29*, 1346–1350.

[57] R. M. Arán-Ais, Y. Yu, R. Hovden, J. Solla-Gullón, E. Herrero, J. M. Feliu, H. D. Abruña, *Journal of the American Chemical Society* **2015**, *137*, 14992–14998.

[58] A. Kongkanand, J. M. Ziegelbauer, *Journal of Physical Chemistry C* **2012**, *116*, 3684–3693.

[59] C. Adam, F. Kanoufi, N. Sojic, M. Etienne, *Electrochimica Acta* **2015**, *179*, 45–56.

[60] S. E. Fosdick, M. J. Anderson, E. G. Nettleton, R. M. Crooks, *Journal of the American Chemical Society* **2013**, *135*, 5994–5997.

[61] J. H. Park, S. N. Thorgaard, B. Zhang, A. J. Bard, *Journal of the American Chemical Society* **2013**, *135*, 5258–5261.

[62] R. G. Compton, C. E. Banks, *Understanding Voltammetry*, 3rd, World Scientific, **2018**.

[63] S. H. Lee, J. C. Rasaiah, *Journal of Chemical Physics* **2011**, *135*, 124505.

[64] R. G. Bates, G. D. Pinching, *Journal of the American Chemical Society* **1949**, *71*, 1274–1283.

[65] R. T. Ferrell, D. M. Himmelblau, *AIChE Journal* **1967**, *13*, 702–708.

[66] T. E. Crozier, S. Yamamoto, *Journal of Chemical and Engineering Data* **1974**, *19*, 242–244.

[67] Q. Chen, L. Luo, H. S. White, *Langmuir* **2015**, *31*, 4573–4581.

[68] X. Zhao, H. Ren, L. Luo, *Langmuir* **2019**, *35*, 5392–5408.

[69] L.-K. Ju, C. S. Ho, *Biotechnology and bioengineering* **1985**, *27*, 1495–1499.

[70] Z. Deng, R. Elattar, F. Maroun, C. Renault, *Analytical Chemistry* **2018**, *90*, 12923–12929.

[71] Y. Wang, J. G. Limon-Petersen, R. G. Compton, *Journal of Electroanalytical Chemistry* **2011**, *652*, 13–17.

Chapter 3

Detection and Characterization of Single Particles using Impedance Spectroscopy

Adapted with permission from: Roehrich, B.; Liu, E. Z.; Silverstein, R.; Sepunaru, L. Detection and Characterization of Single Particles by Electrochemical Impedance Spectroscopy. *The Journal of Physical Chemistry Letters* **2021**, 12 (40), 9748–9753. https://doi.org/10.1021/acs.jpclett.1c02822.

3.1 Introduction

Single-entity electrochemistry has recently emerged as a way to study the properties of single nano- and micro-particles.[1–5] Individual particles are interrogated, one by one, in order to build a bottom-up understanding that captures the heterogeneity among particles in an ensemble.[6, 7] A common scheme is the "nano-impact" technique, in which microelectrodes and low-noise equipment are used to detect single particles when they stochastically collide with an electrode.[4, 8] The current response associated with the impact event can be used, for example, to determine the size of an insulating particle.[9–13] or to monitor the activity of an electrocatalyst.[8, 14–17]

However, it remains a challenge to study complex, pseudocapacitive materials on a single-entity basis. These materials combine Faradaic (electron transfer) and non-Faradaic (ion association) charging, and are critical components of ion batteries and other emerging energy storage devices.[18–21] While careful experimental control and data analysis have allowed detection of single particles and insight into ion intercalation mechanisms.[22–27] quantitative information is difficult to obtain amperometrically. This is due to the possibility of one or several steps (e.g. electron transfer, ion transfer to and from the particle, and ion diffusion within the particle) dictating the current response, which convolutes analysis.

For that reason, electrochemical impedance spectroscopy (EIS) is widely used to characterize bulk pseudocapacitive materials.[28–32] In EIS, a small-magnitude AC voltage is applied and the current response is recorded. By varying the frequency of the AC pertur-

bation, the cell response can be studied across different time scales. Fast processes such as double-layer charging and reversible electron transfer dominate the high-frequency impedance; likewise, slow processes such as sluggish charge transfers, adsorption, and diffusion dominate the low-frequency regime.[32, 33] Thus, a single measurement can simultaneously yield information on the various Faradaic and non-Faradaic processes occurring in the electrochemical system.

While EIS is a powerful technique in the characterization of electroactive materials, it has not yet been applied on a single-entity basis due to the long measurement time of typical EIS experiments.[34] We used fast Fourier-transform EIS (FFT-EIS)[34, 35] in order to improve the time resolution to the point that single-particle impact events could be unambiguously resolved. Using a model system in which individual insulating microparticles block a redox reaction from occurring.[9] we show particle detection and sizing via time-resolved FFT-EIS. The advantage of EIS is leveraged to separate kinetic and diffusional contributions, enhancing precision in the particle size measurement and establishing an advanced characterization technique on a single-particle basis.

3.2 Rapid Acquisition of Impedance Spectra using FFT-EIS

A single impedance spectrum can take minutes to hours to measure when using a typical, frequency-response analyzer (FRA) impedance spectrometer as the impedance

at each frequency of interest must be measured individually. However, single-entity electrochemistry requires fast time resolution in order to resolve individual particle-electrode impact events: if multiple impact events occur between two consecutively sampled points, they will be combined into an apparent single impact event. In our case, particles collide with the electrode every 3.5 ± 1.0 seconds (average ± standard deviation), meaning sub-second time resolution is a requirement for the technique. Fortunately, FFT-EIS has been established as a means of rapidly acquiring impedance spectra.[35] FFT-EIS is analogous to other Fourier-transform spectroscopies (e.g. FTIR, FT-NMR) in that a perturbation voltage that is a superposition of many sinusoidal waves is applied to the working electrode and the current response is recorded.[34, 36, 37] The time-domain current and voltage are then Fourier transformed to yield the frequency-domain impedance spectrum. FFT-EIS can produce impedance spectra with high signal-to-noise ratios in a fraction of the time of the standard FRA technique. The minimum measurement time is limited by the lowest applied frequency: a full period of f_{min} is required to calculate the impedance at that frequency, so $t_{min} = 1/f_{min}$. For example, a spectrum from 50 kHz to 1 Hz can be acquired in 1 s.[35] Limitations on this technique are discussed in the Supporting Information and in previous reports.[38]

Our implementation of FFT-EIS is based on that described by Popkirov and Schindler.[39] Briefly, we applied a time-domain perturbation that contained 17 superimposed sine waves, ranging in frequency from 17 kHz to 100 Hz and with phases selected to avoid excessive constructive interference, which could lead to a non-linear impedance

response (Table 3.6.1 shows applied frequencies and phases). The AC amplitude was 50 mV because it provided the highest S/N without introducing nonlinearities to our impedance data (Figures 3.4 and 3.6, Table 3.6.1). This perturbation signal was added to a DC bias, the formal potential of the redox reaction, and applied to the working electrode of our three-electrode cell (a cyclic voltammogram is shown in Figure 3.6). The applied voltage and the current response were recorded at a sampling rate of 100 kHz. After the measurement, the time-domain signals were split into sequential time intervals (100 ms) and the impedance spectrum was calculated for each time slice. This yielded a series of sequential, rapidly time-resolved impedance spectra suitable for single-entity detection.

3.3 Particle Impacts Observed by FFT-EIS

Carboxylate-functionalized polystyrene microparticles ($r_b = 0.92 \pm 0.07$ μm, see Figure 3.7) were chosen as a simple model system to demonstrate single particle detection by FFT-EIS. Under the low-electrolyte conditions used here (0.5 mM KCl), the microbeads are expected to migrate to the working electrode due to their negative surface charge and the electric field generated by the anodic working electrode, as reported privously.[9] We chose an initial particle concentration of 36 fM to observe around 10 impacts in each 45 s measurement. In doing so, we were able to eliminate occurrences of two or more particles impacting within the same 100 ms spectral measurement time: the probability of this occurring, considering our observed impact frequency of 0.3 s^{-1} and a Poisson

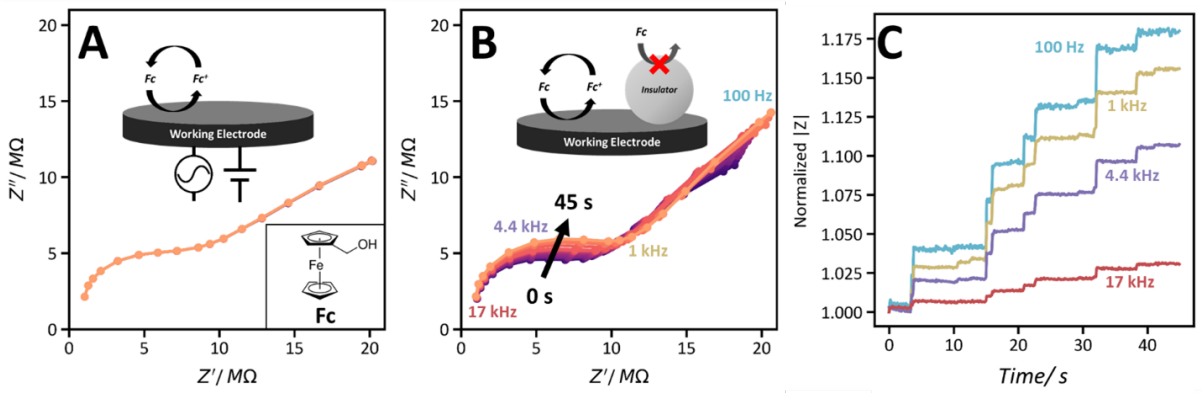

Figure 3.1: Individual insulating polystyrene particles are detected using FFT-EIS when they randomly collide with an ultramicroelectrode. (A) 45 sequential impedance spectra, measured each second for 45 s. Only one spectrum is visible because all 45 coincide with each other, demonstrating no noticeable drift during the experiments. (B) 45 seconds of sequential spectra, recorded in the presence of 36 fM polystyrene microbeads ($r_b = 0.92 \pm 0.07$ μm). Inset: schematic of the "blocking" scheme. (C) The same data as B, plotted as the total impedance versus time for four frequencies, which are indicated in B). The impedance is normalized to the initial impedance for each frequency to highlight the relative effects of the particles across the frequency spectrum. Here, a full impedance spectrum was recorded every 100 ms. Impedance spectra were measured using a carbon fiber disk ultramicroelectrode ($r_e = 2.76$ μm) immersed in 2 mM ferrocenemethanol (FcMeOH) and 0.5 mM KCl, biased at the FcMeOH formal potential (0.194 V vs saturated calomel electrode, applied as 0.12 V vs Ag) with a ±50 mV AC perturbation.

process, is 0.04% (see Supporting Information). It is worth noting that the predicted collision frequency based solely on Brownian motion would be around 10^{-5} s^{-1}.[40, 41] This extremely low frequency is far too low to be adequate for practical experimental measurements and validates the use of low electrolyte concentration that induce the electromigration process mentioned above.

Figure 3.1A shows impedance spectra collected using the FFT-EIS technique from a carbon fiber disk ultramicroelectrode (UME) immersed in 2 mM ferrocenemethanol (FcMeOH) and 0.5 mM KCl in the absence of polystyrene particles (the UME has a

radius of r_e=2.76 μm as shown in Figure 3.8). FcMeOH is a fully reversible outer-sphere redox probe, chosen due to its stability. This beneficial stability is apparent from the overlap of 45 s of impedance spectra in Figure 3.1A – the impedance is constant over the measurement duration in the absence of particles, allowing facile particle impact detection. Once the extremely dilute microparticles were injected into the solution the spectra changed over time, tending towards higher impedances (Figure 3.1B). This is due to the nature of the "blocking"-type scheme used, in which insulating particles discretely adsorb to an electrode and hinder the oxidation of the redox probe (FcMeOH) at the electrode and therefore increase the impedance.[9, 10, 42] When we plotted the total impedance at select frequencies versus time, we observed staircase-like responses at each frequency (Figure 3.1C). Each "step" on the staircase is caused by a single microbead adsorbing to the electrode. Because the frequencies in Figure 3.1C were selected to span the entire impedance spectrum, this result indicates that the beads affect both the fast (high frequency) and slow (low frequency) electrode processes.

We next fit the impedance spectra to examine the effect of each bead on the capacitive, resistive, and diffusional processes occurring at the ultramicroelectrode/single-particle interface. We fit each time-resolved impedance spectrum to the equivalent circuit shown in Figure 3.2A (inset) in order to extract time-resolved equivalent circuit parameters. While many arbitrary equivalent circuits can fit a given set of impedance data, we chose this modified Randles circuit due to its previous success in fitting impedance spectra from microdisc electrodes and the physical interpretability of its parameters.[43–46] The

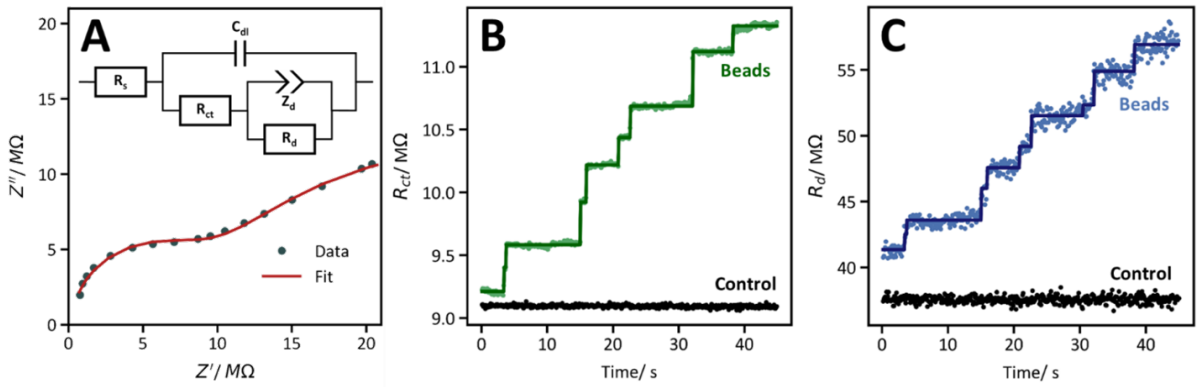

Figure 3.2: Fitting EIS spectra to an appropriate equivalent circuit enables quantification of individual particles' effects on charge transfer and FcMeOH mass transport. A) One representative impedance spectrum (points) with the best fit (curve) to the inset equivalent circuit. B, C) Equivalent circuit elements R_{ct} (charge transfer resistance, B) and R_d (diffusional resistance, C) versus time. Both R_{ct} and R_d remain constant in the absence of beads (black curves); when 36 fM of microparticles (r_b=1 μm) is added both R_{ct} and R_d discretely increase (green and blue curves, respectively). A step-preserving algorithm was used to discretize the data into a staircase-type response (for a detailed description of the step quantification process, see the Supporting Information).

circuit contains terms to account for the solution resistance R_s, the charge-transfer resistance associated with FcMeOH oxidation R_{ct} and the double layer capacitance C_{dl}. The nonlinear diffusion to the microelectrode is modelled by a constant phase element Z_d (a Warburg-like element) in parallel with a diffusional resistance R_d (sometimes referred to as R_{nl}).[43–45] This model provided an excellent fit to our experimental data as shown in Figure 3.2A (typical parameters are given in Table 3.6.2 and an alternative equivalent circuit that yielded a poor fit is shown in Figure 3.9).

3.4 Quantifying Effects of Blocking Particles on Charge Transfer and Diffusion at a Microelectrode

While all five parameters are observed to change over time after bead addition, here we focus on R_{ct} and R_d in order to probe the relative effects of the beads on the fast charge-transfer process and slower FcMeOH diffusion, respectively. A full discussion of the other parameters, including observed discrete changes in the double layer capacitance, is given in the Supporting Information (Figure 3.10). Both R_{ct} and R_d remain constant in the absence of particles (Figure 3.2B, C controls) but discretely increase in the presence of the microbeads. Each discrete increase in R_{ct} is attributed to an individual bead adsorbing to the electrode surface and blocking the contact area from exchanging charge with the solution. The resulting decrease in the electrode's surface area A corresponds to an increase in R_{ct} as shown by Equation 3.1,

$$R_{ct} = \frac{RT}{nFAj_0} \tag{3.1}$$

where R is the gas constant, T the temperature, n the number of electrons transferred, F Faraday's constant, and j_0 the exchange current density.[47] On the other hand, R_d increases because each bead affects the mass transport of the redox probe, FcMeOH, to and from the electrode surface. R_d is used to account for nonlinear diffusion to microelectrodes, and has been reported as inversely proportional to the steady-state,

diffusion limited current.[43] Insulating particles, such as the polystyrene beads used in this model system, are known to block the flux of redox probe to the electrode.[9, 10, 48] Thus, the discrete increases in R_d are consistent with previous amperometric results. R_{ct} and R_d were then transformed into stairstep-like responses (solid lines, Figure 3.2B and C) to extract the discrete effect of each bead (see Figure 3.11 for details on the step quantification process).

We sought to quantify the size of each microbead to demonstrate the capability of SE-EIS to measure meaningful physical parameters. Equation 3.1 can be manipulated to show that the relative change in R_{ct} is directly proportional to the relative change in electrode area, i.e. $\Delta R_{ct}/R_{ct} = -\Delta A/A$. As R_d is inversely proportional to the diffusion-limited current i_l, a similar relationship holds between R_d and i_l. Both $\Delta A/A$ and $\Delta i_l/i_l$ are proportional to the size of the particle, so $\Delta R_{ct}/R_{ct}$ and $\Delta R_d/R_d$ give two separate measures of the individual particles' size – one which utilizes a "fast" process (charge transfer) and one which is from a "slow" process (diffusion). We measured several hundred particle-electrode impact events and quantified $\Delta R_{ct}/R_{ct}$ and $\Delta R_d/R_d$ for each event. Distributions of these two parameters are shown in Figure 3.3A.

Despite the highly monodisperse microparticles used in this study (Figure 3.7), we observed a relatively broad distribution of $\Delta R_d/R_d$ (Figure 3.3A). This is predominantly caused by the heterogeneous distribution of flux to microelectrodes. The small size of microelectrodes creates a radial diffusion layer (compared to the linear diffusion to a planar macroscopic electrode) which causes a relatively higher flux of redox species to

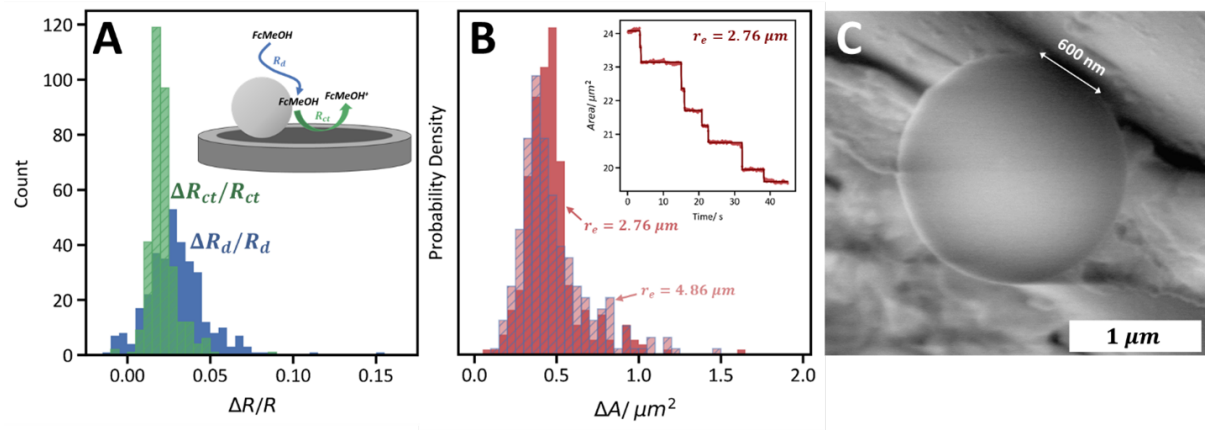

Figure 3.3: Quantitative impedance analysis of single-particle impact data. (A) Histograms of $\Delta R_d/R_d$ and $\Delta R_{ct}/R_{ct}$, each containing data from N = 337 steps. Inset: schematic depicting the different properties measured by R_d (FcMeOH diffusion) and R_{ct} (FcMeOH oxidation kinetics). (B) Direct measurement of single particles' footprints on the electrode. Histograms of ΔA for r_b=1 μm beads measured on carbon ultramicroelectrodes with r_e=2.76 μm (solid, N = 337) and 4.86 μm (dashed, N = 294). Despite a shift in relative step sizes $\Delta R_{ct}/R_{ct}$ (Figure 3.14), the two histograms overlap significantly. Inset: staircase response when plotting electrode area versus time, showing the direct measurement of ΔA. (C) SEM micrograph showing a side view of a bead adsorbed to the electrode surface. The contact diameter is around 0.6 μm.

the electrode's edge compared to its center.[12, 49, 50] This means that a bead that lands near the edge of the electrode will block more redox probe flux than one that lands near the center, creating position-based convolutions in the measured $\Delta R_d/R_d$ and in amperometric $\Delta I/I_{ss}$ (Figure 3.12). However, these artifacts are only present in the diffusion-based R_d parameter. R_{ct} is independent of diffusion effects and relates to the electron-transfer kinetics, which should be uniform across the electrode surface. Thus, we observe a much sharper distribution in $\Delta R_{ct}/R_{ct}$: the relative decrease in electrocatalytic surface area is independent of the bead's location on the electrode. This result highlights the main advantage of EIS, namely, its ability to isolate electrochemical processes that occur on different timescales. In this model system, it allows for increased precision in particle sizing by separately analyzing the particles' effects on redox kinetics and FcMeOH diffusion.

A further advantage of EIS in this system is that it allows for direct measurement of the particle-electrode contact area. Typical amperometric particle sizing relies on relative changes in current, i.e. $\Delta I/I_{ss}$. Accurate conversion to particle size requires an empirical geometric factor to account for the flux heterogeneity described above.[12] and is further convoluted because particles which arrive later will have smaller relative effects (i.e. smaller $\Delta I/I_{ss}$) than the first particles.[51] Single-entity EIS lets us bypass these factors by directly converting the measured R_{ct} into the current electrode area A via Equation 3.1, using the previously-measured exchange current density (Table 3.6.4). From there, the electrode surface area can be measured as a function of time (Figure

3.3B inset) and the change in surface area ΔA can be directly measured for each impact event. Analysis of the same dataset used in Figure 3.3A yields the distribution in ΔA shown in Figure 3.3B (solid histogram). The most probable ΔA is around 0.5 μm^2. This value represents the footprint of the bead on the electrode. Notably, the distribution in ΔA remains similar when measured using a larger working electrode (r_e=4.86 μm, Figure 3.3B dashed histogram) even though there is a significant difference in the relative step sizes $\Delta R_{ct}/R_{ct}$ and $\Delta R_d/R_d$ (Figures 3.13, 3.14). Thus, ΔA is a physically meaningful measure of each particle's footprint on the electrode, which is independent of the electrode size or the bead's location at the electrode surface.

This electrochemically measured sub-micron contact area is further corroborated using scanning electron microscopy (SEM) imaging of a bead adsorbed to the electrode surface (experimental conditions are discussed in the Supporting Information). As shown by the cross-sectional micrograph in Figure 3.3C, the contact between the bead and the electrode spans 0.6 μm. This yields a contact area of 0.3 μm^2, in good agreement with the particle footprints measured by EIS. Other imaged beads appeared deformed on the electrode surface, deviating from the expected spherical geometry (Figure 3.15). These deformations may increase or decrease the particle-electrode contact area, possibly explaining the width of the distribution seen in Figure 3.3C. In principle, the fact that the bead's contact area at the electrode surface is comparable between the two methods is encouraging and further validates the applicability of using impedance spectroscopy at the nanoscale.

3.5 Conclusions

In conclusion, we have demonstrated single-particle detection using time-resolved electrochemical impedance spectroscopy. The advantage of EIS is its ability to separate electrochemical processes that occur on different timescales; here, this advantage was leveraged to measure the footprint of individual polystyrene microparticles as they adsorbed to an electrode surface. EIS enhanced precision in sizing by isolating problematic diffusional "edge" effects to the R_d parameter, yielding a sharp distribution in the kinetic R_{ct}. Furthermore, real-time monitoring of the electrode surface area A directly yields each particle's contact area with the electrode; measured ΔA values agree well with SEM imaging. This approach engenders deeper insights from single-entity data, even in a simple blocking-type model system. In the future, the frequency analysis afforded by EIS will prove invaluable in studying single pseudocapacitive microparticles, electrocatalysts, and other energy-relevant materials.

3.6 Supporting Information

3.6.1 Experimental

Materials: Solutions of ferrocenemethanol (AK Scientific, 98%), $Ru(NH_3)_6Cl_3$ (Acros Organics, 98%), and potassium chloride (Sigma-Aldrich, ≥99.0%) were prepared using MilliQ water (≥18.2 MΩ·cm). 1 μm radius polystyrene beads were purchased from Invitrogen (batch number 1348481).

Electrochemical measurements: All measurements were performed using an EPC10 Double Patch Clamp Amplifier (HEKA Electronik, Lambrecht, Germany) in the three electrode configuration. A platinum wire was used as the counter electrode and a silver wire as a pseudoreference electrode. The working electrodes used were carbon disks with radii 2.76 and 4.86 μm (purchased from CH Instruments and BASi, respectively), as measured electrochemically by $Ru(NH_3)_6^{3+}$ reduction. The electrochemical cell was placed inside well-grounded dual Faraday cages to reduce external electromagnetic noise. The EPC10 "C-fast" function was used to measure and correct for stray capacitances which would be detrimental to the impedance measurements. "C-fast" was measured with all three electrodes inside the electrochemical cell, but before the addition of electrolyte solution to the cell. This corrects for parasitic instrumental and cabling capacitances, defects in the working electrode, etc; but does not affect the capacitance associated with the electrode/electrolyte interface.

All measurements were performed using 2 mM FcMeOH and 0.5 mM KCl. For measurements using beads, 10 μL of stock solution (18.27 pM) was added to 5 mL of FcMeOH solution to yield a final bead concentration of 36 fM. The beads were dispersed in the solution by sonication. Before each 45 s impedance measurement, the working electrode was polished on 1 μm, 0.3 μm, and 0.05 μm alumina slurry (Buehler) sequentially for 1 minute each. A silver wire was chosen as the pseudoreference electrode because electrolyte leaks from conventional reference electrodes (i.e. saturated calomel, Ag/AgCl in KCl, etc.)[52] can significantly change the ionic strength of the weakly-supported (0.5 mM KCl) analyte solution. Changes in ionic strength could affect both the particle impact frequency, which is controlled by electromigration, as well as the charge-transfer kinetics.

FFT-EIS: The FFT-EIS waveform was created using a simple Python script that adds together multiple time-domain sine waves. Details of the nature of the waveform are given in the next section. The script output the waveform in ASCII format, which was imported into the potentiostat control software (PATCHMASTER) and used to create a custom stimulus file. This file set the AC potential of the working electrode during EIS measurements, the second channel of the potentiostat was used to add a constant DC bias to the AC waveform. The AC waveform was filtered at 500 kHz before it was applied to the working electrode. In measurements, the voltage and current were sampled at 100 kHz after the current was filtered using a 30 kHz Bessel filter.

Later, the recorded time-domain voltage and current were split into predefined time intervals (100 ms). They were Fourier transformed using a custom Python script, and the impedance spectrum was calculated for each time segment. The 30 kHz Bessel filter has a noticeable impact on the high-frequency impedance, so each impedance spectrum was corrected for the filter's transfer function by the following procedure: the impedance spectrum of a 10 MΩ resistor was measured and saved. |Z| and phase (ϕ) correction factors were determined at each frequency such that the corrected spectrum had |Z| = 10 MΩ and $\phi = 0$ at all frequencies. These correction factors were then applied to every measured impedance spectrum.

Finally, each impedance spectrum was fit to the equivalent circuit using MEISP software (Kumho Petrochemical Co. Ltd.) to extract time-resolved equivalent circuit parameters.

Cross-sectional SEM imaging: The contact area between the beads and the electrode was evaluated from SEM (Apreo C FEG from ThermoFisher). The electrode was first immersed in the typical FcMeOH solution, and +100 mV (vs Ag wire) was applied until a single particle impact event was observed in the current versus time trace. The electrode was then dried in air overnight before SEM imaging. Images were acquired using a low vacuum detector (LVD) operating in a low vacuum operation mode. The differential pressure between the specimen chamber and the gun column is controlled using water vapor which in this experiment was set to 50 Pa. This type of imaging mode has enabled

us to mitigate charging of the uncoated sample while maintaining good image resolution using an intermediate accelerating voltage of up to 10 kV.

Index	Frequency/ Hz	Phase/ degree
1	100	0
2	110	143
3	170	4
4	250	136
5	370	250
6	520	129
7	750	12
8	1000	164
9	1300	-5
10	2100	46
11	3100	78
12	4400	-53
13	6400	134
14	9000	25
15	11000	59
16	13000	50
17	17000	154

Table 3.1: Frequencies (and phases) used to construct the multi-sine EIS waveform.

We adopted our EIS waveform from that reported by Popkirov and Schindler.[35] removing every other frequency in order to increase S/N by concentrating the perturbation power into fewer frequencies. The time-domain waveform was calculated by Equation 3.2,

$$v(t) = \sum_{j=1}^{17} a_j \sin 2\pi f_j t + \phi_j \tag{3.2}$$

Where a_j is the amplitude, f_j the frequency (from Table 3.6.1), and ϕ_j the phase (from Table 3.6.1) of the j^{th} sine wave. Typically, a_j was the same for all frequencies (an exception is discussed below, for the r_e=4.86 μm electrode). The summed waveform v(t) was then normalized to the desired AC amplitude. For example, a ±50 mV AC

amplitude means that the maximum of v(t) is 50 mV and the minimum -50 mV, giving a 100 mV peak-to-peak.

The chosen frequency range was sufficient to resolve both the charge-transfer (high frequency) and diffusional features of FcMeOH oxidation on the carbon ultramicroelectrodes used in this study. Spectral acquisition with a lowest frequency of 100 Hz can in principle be accomplished in 10 ms, but we noticed unacceptable noise in measurements in this configuration. Thus, we measured spectra every 100 ms, such that each spectrum contains 10 periods of the lowest frequency (100 Hz) which significantly improves S/N. Time resolution on the order of $1/f_{min}$ may not be feasible due to these S/N considerations.

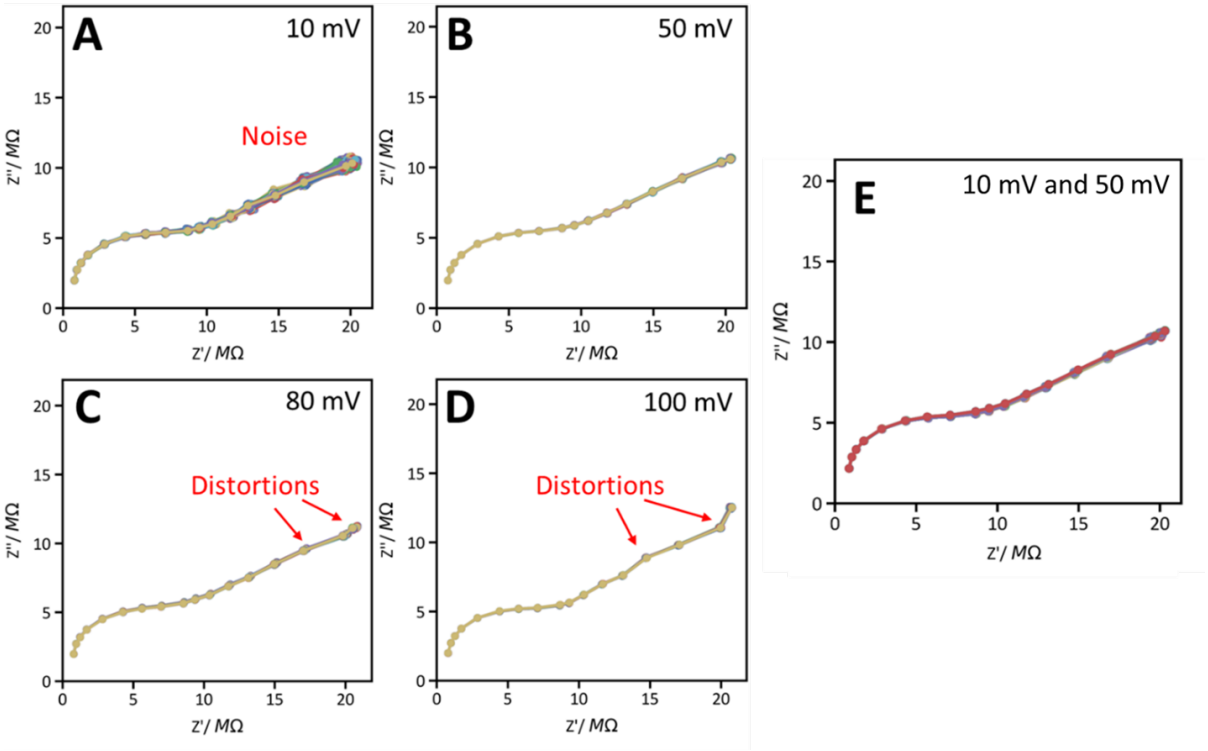

Figure 3.4: Nyquist plots measured using (A) 10 mV, (B) 50 mV, (C) 80 mV, and (D) 100 mV AC amplitude. Each measurement was recorded using an r_e=2.76 μm carbon UME in 2 mM FcMeOH and 0.5 mM KCl in the absence of beads. The DC bias was the FcMeOH formal potential (+0.12 V vs Ag, equivalently +0.194 V vs saturated calomel electrode). Each Nyquist plot contains 450 sequential spectra with 0.1 s measurement time, representing 45 s of continuous data. Noise is visible in the low-frequency dispersion in A), and distortions are visible in the low-frequency region of C and D due to either nonlinearities or current amplifier saturation. The 50 mV AC amplitude in B allows for good noise performance without causing distortions in the Nyquist plot. (E) Overlayed Nyquist plots recorded with 10 mV (yellow) and 50 mV (red) AC perturbations. Each has 10 spectra with 1 s measurement time, which was chosen to limit the noise in the 10 mV measurement (as is visible in A). The spectra overlap to the extent that the 10 mV spectrum is entirely eclipsed, showing that the 50 mV AC perturbation does not introduce significant nonlinearities compared to the 10 mV perturbation.

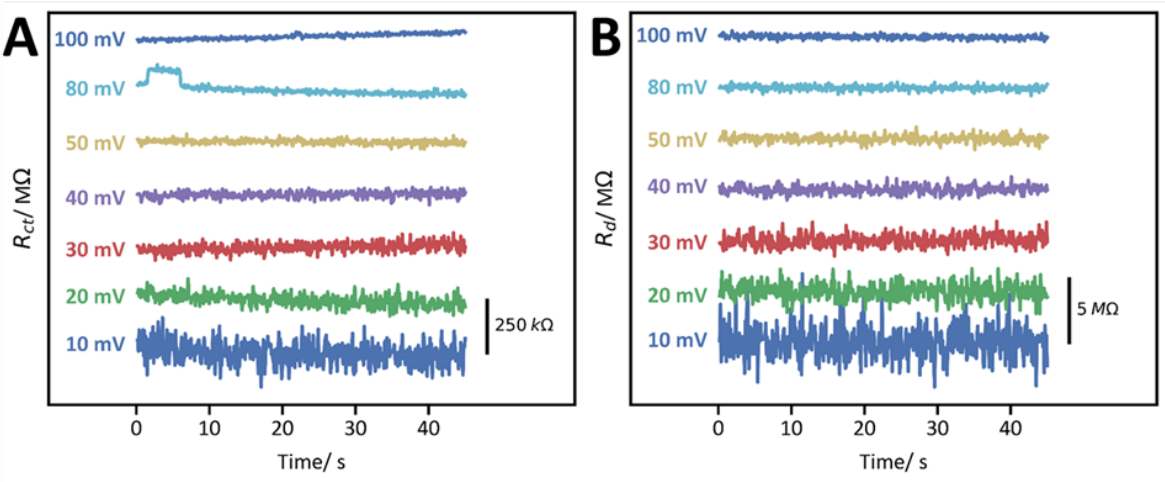

Figure 3.5: (A) R_{ct} and (B) R_d measured vs time with 7 different AC amplitudes (bottom to top: 10, 20, 30, 40, 50, 80, and 100 mV) with 100 ms sampling. Each measurement is offset to allow visualization of the noise.

AC Amplitude/ mV	R_{ct} Noise/ MΩ	R_d Noise/ MΩ
10	0.054	1.29
20	0.030	0.65
30	0.022	0.49
40	0.015	0.35
50	0.011	0.29
80 (distorted)	0.010	0.22
100 (distorted)	0.013	0.20

Table 3.2: Noise in R_{ct} and R_d as a function of AC amplitude.

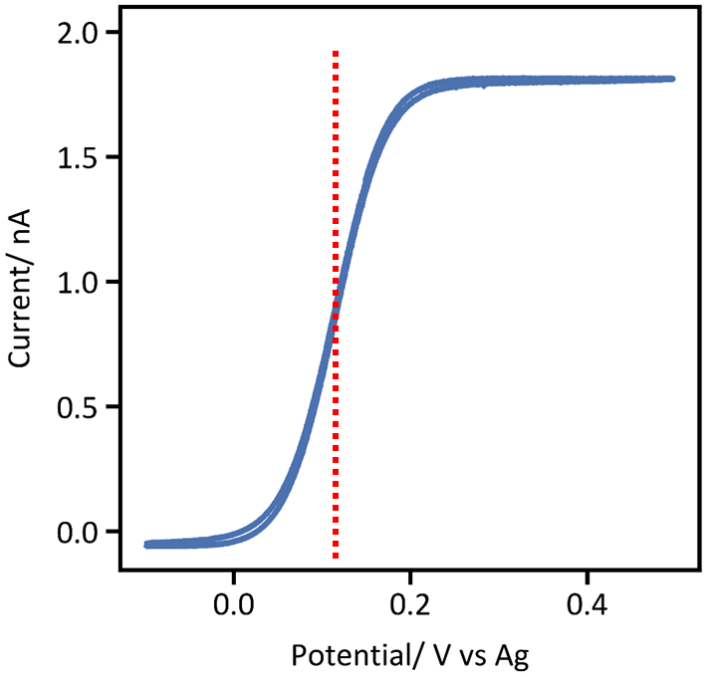

Figure 3.6: Cyclic voltammogram of 2 mM FcMeOH in 0.5 mM KCl recorded at 10 mV/s on the r_e=2.76 μm carbon fiber ultramicroelectrode. The counter electrode was a Pt wire and the pseudoreference electrode was an Ag wire. The formal potential, which was applied as the DC bias in EIS measurements, is +120 mV vs Ag as indicated by the dashed red line.

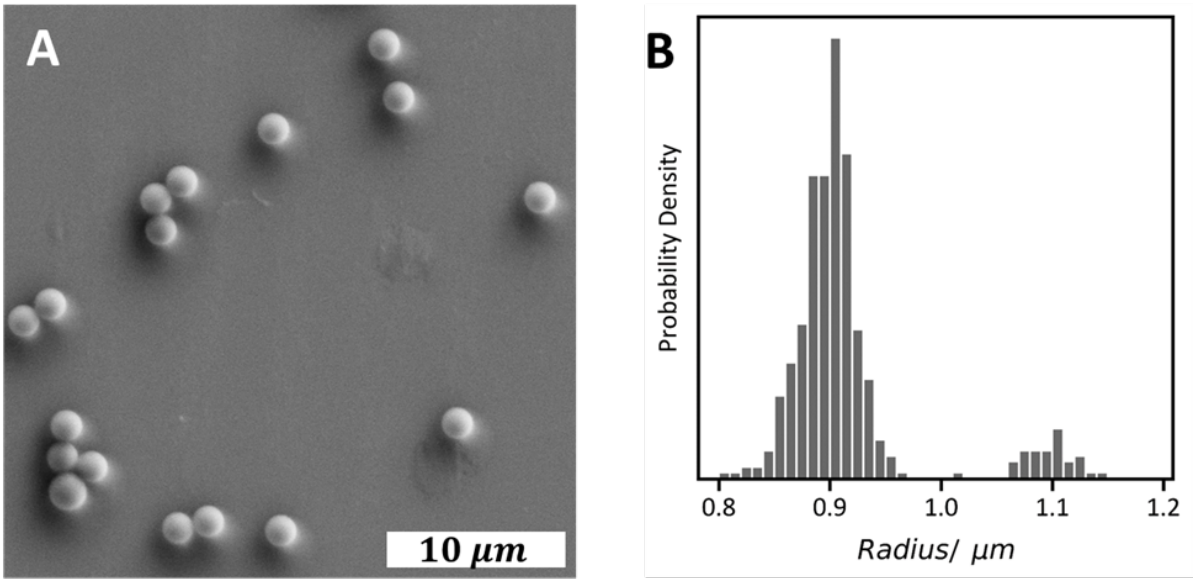

Figure 3.7: (A) Scanning electron micrograph of the r_b=1 μm beads adsorbed on a glass slide. (B) Histogram of bead radii extracted from SEM micrographs using ImageJ (N = 422).

3.6.2 Probability of Overlapping Events Calculation

We calculated the probability of two independent particles impacting within a 100 ms sampling interval. If this happened, data sampling would merge the two events into a single apparent impact. This can be modelled as a Poisson process because the events occur randomly, but with a known average frequency.[53]

$$P(n) = \frac{e^{-\lambda t}(\lambda t)^n}{n!} \tag{3.3}$$

Here, λ=0.283 s^{-1} (average over N=337 impact events), t=0.1 s, and n=2 impacts gives $P(2) = 4 \times 10^{-4}$.

$$I = 4nFDCr_e \tag{3.4}$$

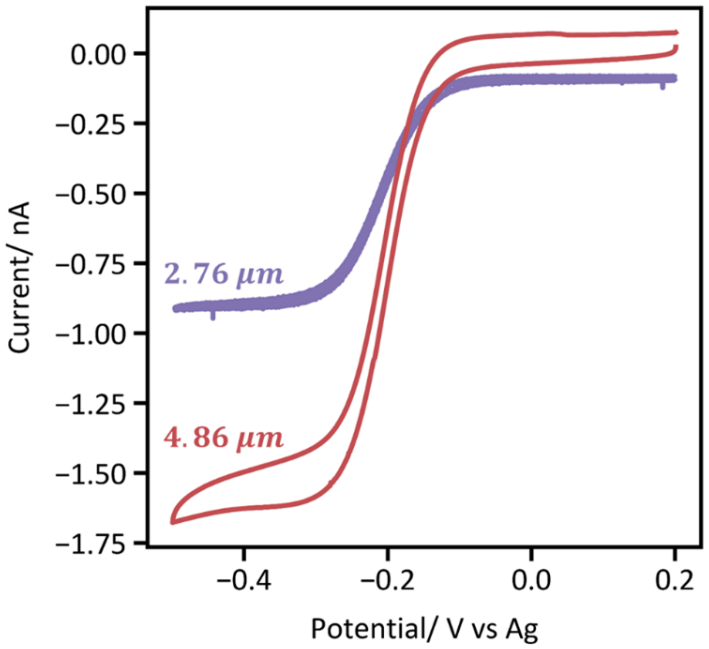

Figure 3.8: Cyclic voltammograms recorded using r_e=2.76 μm and r_e=4.86 μm carbon fiber ultramicroelectrodes in 1 mM $Ru(NH_3)_6^{3+}$ and 100 mM KCl with a scan rate of 10 mV/s. After baseline subtraction, the steady-state currents were determined to be 0.90 and 1.58 nA, respectively. Taking the diffusion coefficient of $Ru(NH_3)_6^{3+}$ as 8.43×10^{-10} m^2 s^{-1},[54] the electrode radii were calculated using Equation 3.4 .[55] Ruthenium (III) hexamine was used for electrode sizing because in the low electrolyte conditions used in the FcMeOH measurements, steady-state currents can deviate significantly due to self-induced convection at the electrode surface.[11]

R_s/ MΩ	R_{ct}/ MΩ	R_d/ MΩ	C_{dl}/ pF	Z_d/ Ω^{-1} s^{α}	α_{Z_d}
0.38	9.22	40.8	3.70	3.89	0.74

Table 3.3: Typical EIS fit parameters.

Previous reports on microelectrode EIS have used a Warburg element to describe diffusion, i.e. $\alpha_{Z_d} = 0.5$. We consistently observed α around 0.75, possibly due to self-induced

convection (caused by the low supporting electrolyte conditions used here) influencing the mass transport of the redox probe.[11]

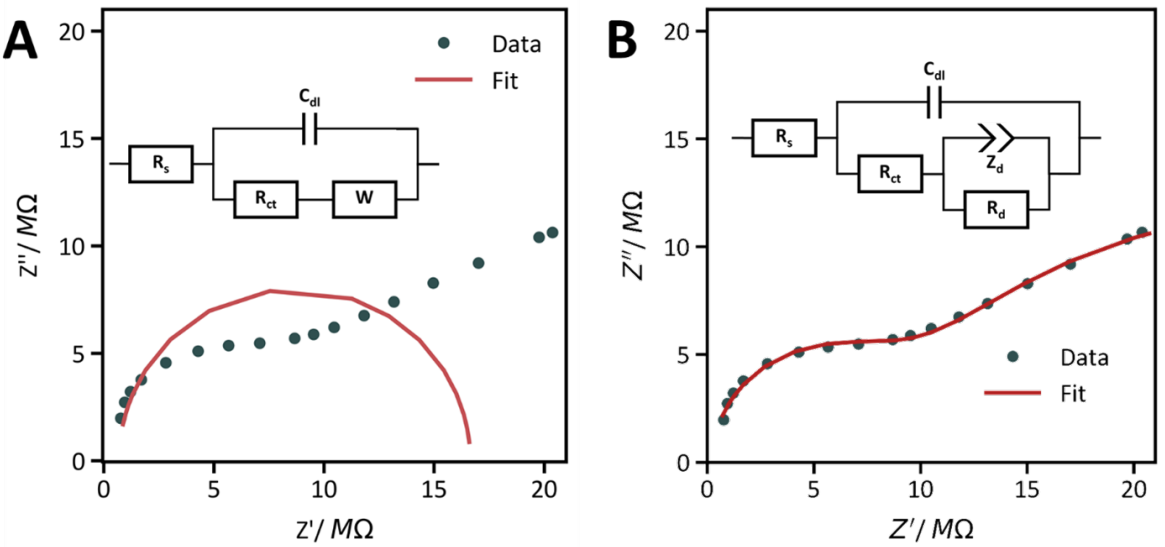

Figure 3.9: Comparison between fits from an inadequate equivalent circuit (Randles circuit, A) and the model used herein (B). The Randles circuit (A, inset) uses a Warburg element (W) to model semi-infinite linear diffusion to a macroelectrode, rendering it unsuitable for the hemispherical diffusion to a microelectrode.

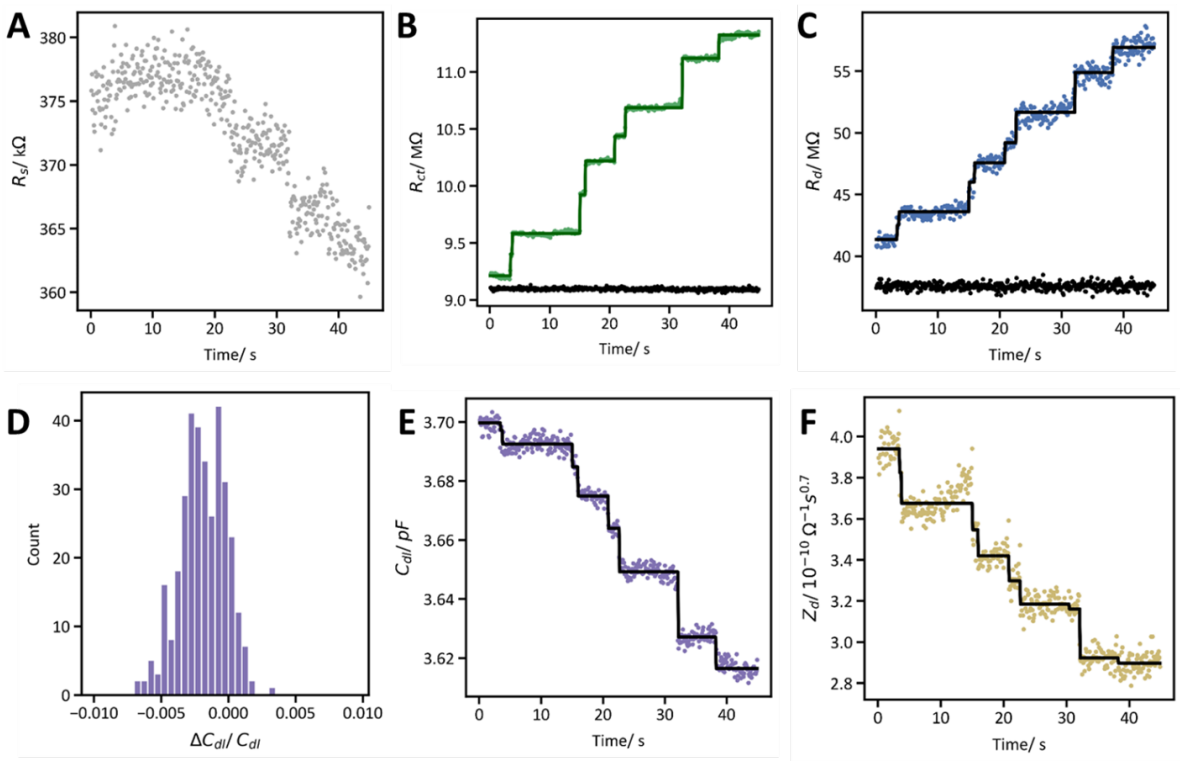

Figure 3.10: EIS equivalent circuit elements (A) R_s, (B) R_{ct}, (C), R_d, (E) C_{dl}, and (F) Z_d versus time. Data were recorded using an r_e=2.76 μm carbon UME in 2 mM FcMeOH and 0.5 mM KCl in the presence of 36 pM polystyrene microbeads (r_b=1 μm). In addition to the R_{ct} and R_d data shown in the main text, C_{dl} was analyzed using the same stair-stepping protocol. A histogram of $\Delta C_{dl}/C_{dl}$ is shown in D (N = 337 steps). The majority of bead impacts caused a small decrease in C_{dl}, likely due to the adsorbed region of the bead inhibiting double layer formation. Decreases are also seen in Z_d due to the hindered diffusion caused by the beads (F), while no discrete events are observed in R_s.

3.6.3 Step detection and quantification

From the data shown in Figure 3.1C in the main text we determined that the steps were most prominent at 100 Hz. We applied a simple stair-stepping algorithm to the 100 Hz |Z| versus time data to determine time indices where bead impacts occurred (Figure 3.11 A, red triangles). For the r_e=2.76 μm electrode steps were

picked with $\Delta|Z|/|Z| > 1\%$, while for the r_e=4.86 μm electrode steps were picked with $\Delta|Z|/|Z| > 0.5\%$ due to the smaller signals. Then, the time indices were applied to the equivalent circuit parameters (for example, R_d versus time as shown in Figure 3.11 B). The median value of the parameter between two sequential bead impacts was used to determine the step size. This approach let us extract usable data even from the relatively noisy R_d data shown in Figure 3.11B.

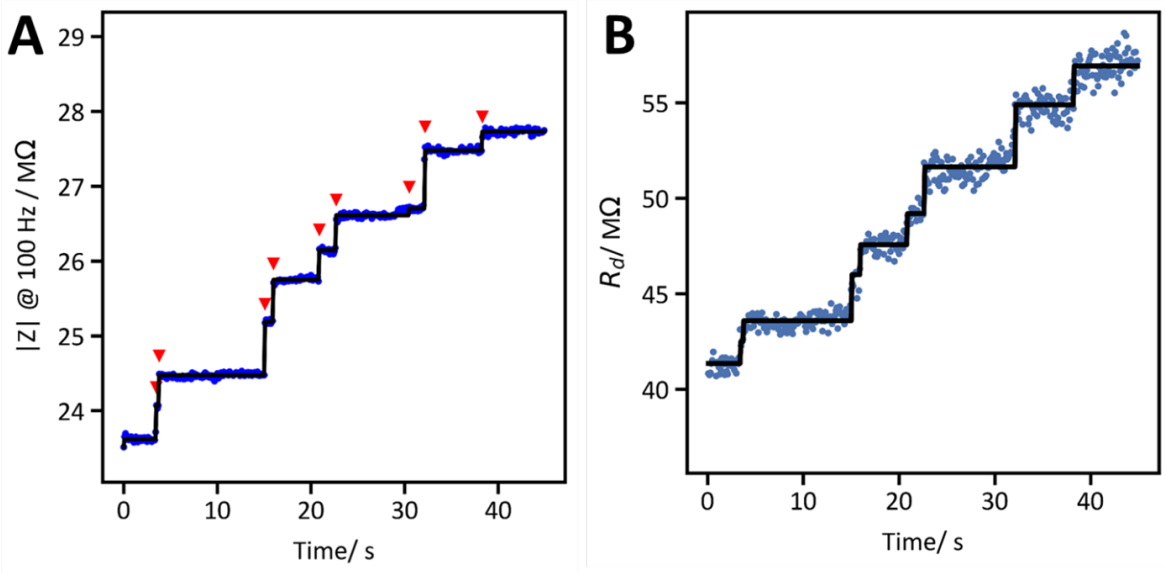

Figure 3.11: (A) Step detection algorithm applied to the 100 Hz |Z| versus time. Steps (red triangles) are picked from the data (blue points). (B) R_d versus time for the same dataset. The step times from A were used to fit a staircase response. The horizontal regions are the median value of R_d between each step.

3.6.4 Effective Exchange Current Density Calculation

The R_{ct} parameter can be related to an effective exchange current density $j_{0,eff}$ as,[47]

$$R_{ct} = \frac{RT}{nFAj_{0,eff}} \tag{3.5}$$

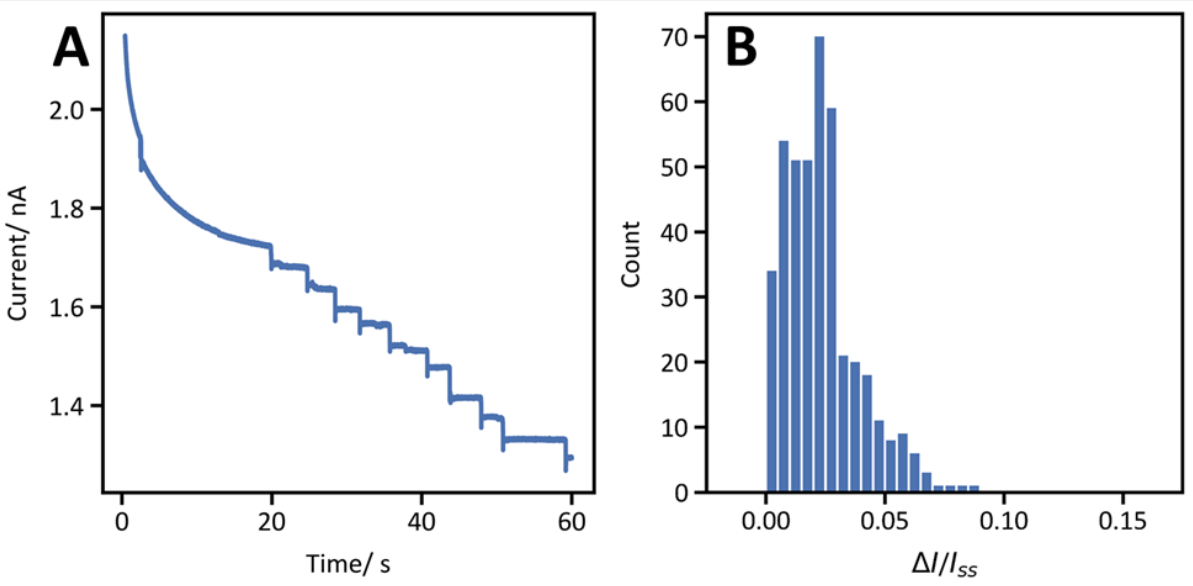

Figure 3.12: Amperometric detection of polystyrene microbeads. (A) Typical chronoamperomogram, recorded using a carbon ultramicroelectrode with r_e=2.76 μm immersed in a solution of 2 mM FcMeOH, 0.5 mM KCl and 36 fM polystyrene beads (r_b=1 μm). The working electrode was biased at +400 mV vs Ag wire, which is in the FcMeOH diffusion-limited regime. Each particle adsorption event discretely decreases current, manifesting in the steps visible in the figure. (B) Distribution of relative changes in current $\Delta I/I_{ss}$ corresponding to bead adsorption events measured using the amperometric technique (N = 419).

Where R is the gas constant (8.314 J mol^{-1} K^{-1}, T is temperature (298 K), n is the number of electrons transferred (1), F is Faraday's constant (96458 C mol^{-1}), and A is the electrode surface area. $j_{0,eff}$ is not the true exchange current density j_0 due to non-equilibrium conditions in the bulk solution (the initial conditions have no $FcMeOH^+$ in the bulk). However, it is constant over the measurement duration as seen by the control experiment in Figure 3.2B in the main text and allows relation of R_{ct} to the electrode area. Equation 3.5 was used to calculate the electrode area shown in Figure 3.3B in the main text.

Electrode radius/ μm	Area/ μm^2	R_{ct}/ MΩ	$j_{0,eff}$ / mA cm^{-2}
2.76	23.9	9.22	11.7
4.86	55.7	6.37	7.2

Table 3.4: $j_{0,eff}$ calculated from Equation 3.5

3.6.5 Comparison between 2.76 and 4.86 μm electrodes

We also used single entity EIS to measure particle impacts on an r_e=4.86 μm electrode. To avoid saturating our current amplifier, we optimized the voltage waveform such that $a_j \propto |Z|_j$ as previously described by Popkirov and Schindler.[39] This allowed a high-amplitude perturbation at low frequency (high impedance) to maximize S/N while avoiding saturating the amplifier by passing a large current at high frequencies (low impedance). The waveform used is shown in Figure 3.13.

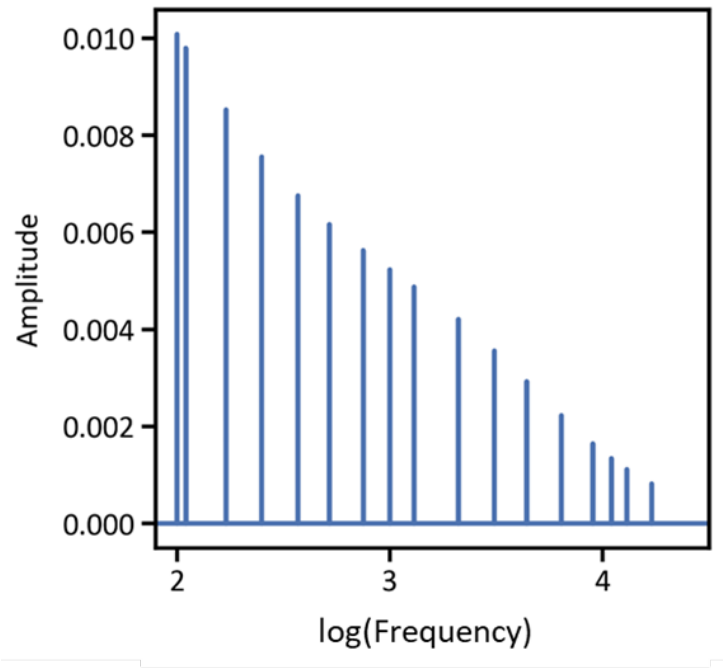

Figure 3.13: Frequency domain representation of the "optimized" waveform used with the r_e=4.86 μm. In the time domain, the summed voltage was still normalized to have a maximum of 50 mV.

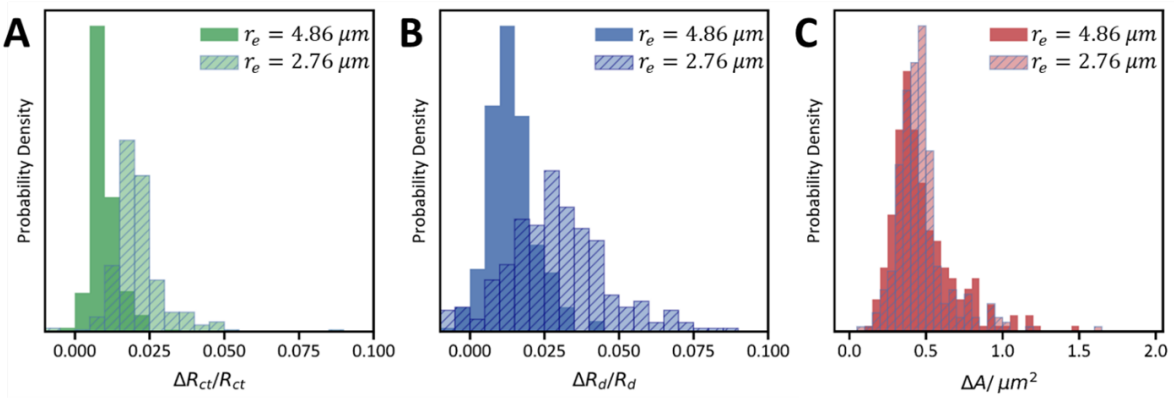

Figure 3.14: Comparisons in distributions of (A) $\Delta R_{ct}/R_{ct}$, (B) $\Delta R_d/R_d$, and (C) ΔA obtained on the r_e=2.76 μm electrode (dashed, N = 337) and those obtained on the r_e=4.86 μm electrode (solid, N = 294). The histograms shown in C are reproduced from Figure 3.3B in the main text for comparison. Data were recorded in 2 mM FcMeOH and 0.5 mM KCl in the presence of 36 pM polystyrene microbeads (r_b=1 μm). Despite shifts in $\Delta R_{ct}/R_{ct}$ and $\Delta R_d/R_d$ between the two electrode sizes, the distributions in ΔA have significant overlap below 0.5 μm^2. Relative step sizes in A and B are smaller on the large (4.86 μm) electrode because each bead has a smaller relative effect on the electrode compared to the small (2.76 μm) electrode.

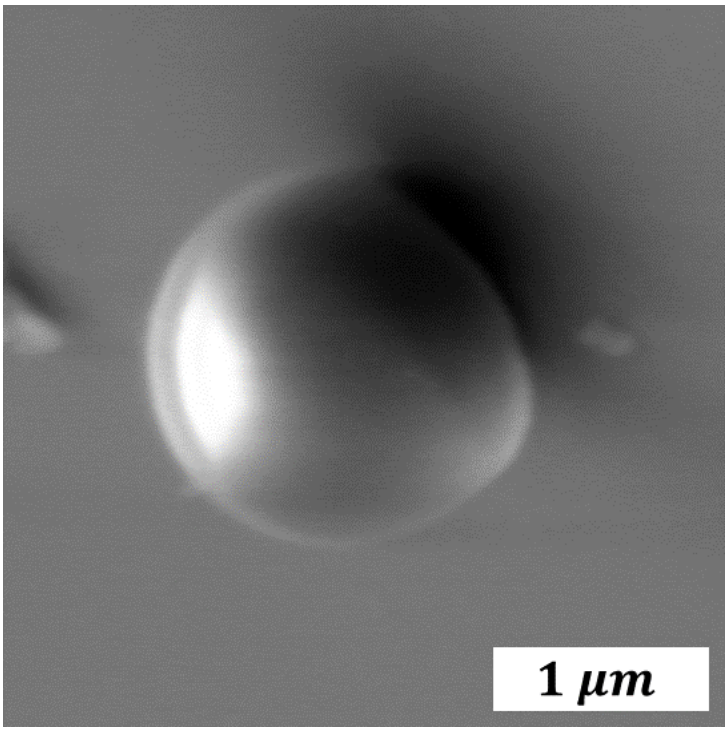

Figure 3.15: SEM micrograph of a polystyrene particle on the carbon fiber ultramicroelectrode surface. The particle is visibly deformed from the typical spherical geometry, which affects its contact area with the electrode.

References

[1] L. A. Baker, *Journal of the American Chemical Society* **2018**, *140*, 15549–15559.

[2] A. J. Bard, H. Zhou, S. J. Kwon, *Israel Journal of Chemistry* **2010**, *50*, 267–276.

[3] L. K. Allerston, N. V. Rees, *Current Opinion in Electrochemistry* **2018**, *10*, 31–36.

[4] S. V. Sokolov, S. Eloul, E. Kätelhön, C. Batchelor-McAuley, R. G. Compton, *Physical Chemistry Chemical Physics* **2017**, *19*, 28–43.

[5] S. M. Lu, Y. Y. Peng, Y. L. Ying, Y. T. Long, *Analytical Chemistry* **2020**, *92*, 5621–5644.

[6] H. Ren, M. A. Edwards, *Current Opinion in Electrochemistry* **2021**, *25*, 100632.

[7] S. Goines, J. E. Dick, *Journal of The Electrochemical Society* **2020**, *167*, 037505.

[8] Y. Xiao, F. R. F. Fan, J. Zhou, A. J. Bard, *Journal of the American Chemical Society* **2008**, *130*, 16669–16677.

[9] B. M. Quinn, P. G. V. '. Hof, S. G. Lemay, *Journal of the American Chemical Society* **2004**, *126*, 8360–8361.

[10] J. E. Dick, C. Renault, A. J. Bard, *Journal of the American Chemical Society* **2015**, *137*, 8376–8379.

[11] T. Moazzenzade, X. Yang, L. Walterbos, J. Huskens, C. Renault, S. G. Lemay, *Journal of the American Chemical Society* **2020**, DOI `10.1021/jacs.0c08450`.

[12] J. Bonezzi, A. Boika, *Electrochimica Acta* **2017**, *236*, 252–259.

[13] K. McKelvey, M. A. Edwards, H. S. White, *Journal of Physical Chemistry Letters* **2016**, *7*, 3920–3924.

[14] A. E. Arrassi, Z. Liu, M. V. Evers, N. Blanc, G. Bendt, S. Saddeler, D. Tetzlaff, D. Pohl, C. Damm, S. Schulz, K. Tschulik, *Journal of the American Chemical Society* **2019**, *141*, 9197–9201.

[15] X. Xiao, A. J. Bard, *Journal of the American Chemical Society* **2007**, *129*, 9610–9612.

[16] B. Roehrich, L. Sepunaru, *Angewandte Chemie International Edition* **2020**, *59*, 19184–19192.

[17] S. E. F. Kleijn, S. C. S. Lai, T. S. Miller, A. I. Yanson, M. T. M. Koper, P. R. Unwin, *Journal of the American Chemical Society* **2012**, *134*, 18558–18561.

[18] K. Hernández-Burgos, Z. J. Barton, J. Rodríguez-López, *Chemistry of Materials* **2017**, *29*, 8918–8931.

[19] B. D. Paulsen, K. Tybrandt, E. Stavrinidou, J. Rivnay, *Nature Materials* **2020**, *19*, 13–26.

[20] B. D. Paulsen, S. Fabiano, J. Rivnay, **2021**.

[21] I. Riess, *Solid State Ionics* **2003**, *157*, 1–17.

[22] G. Zampardi, C. Batchelor-McAuley, E. Kätelhön, R. G. Compton, *Angewandte Chemie* **2017**, *129*, 656–659.

[23] W. Xu, Y. Zhou, X. Ji, *Journal of Physical Chemistry Letters* **2018**, *9*, 4976–4980.

[24] X.-F. Zhou, W. Cheng, R. G. Compton, *Angewandte Chemie* **2014**, *126*, 12795–12797.

[25] E. Katelhon, A. Feng, W. Cheng, S. Eloul, C. Batchelor-McAuley, R. G. Compton, *Journal of Physical Chemistry C* **2016**, *120*, 17029–17034.

[26] L. Sun, D. Jiang, M. Li, T. Liu, L. Yuan, W. Wang, H. Y. Chen, *Analytical Chemistry* **2017**, *89*, 6050–6055.

[27] T. Löffler, J. Clausmeyer, P. Wilde, K. Tschulik, W. Schuhmann, E. Ventosa, *Nano Energy* **2019**, *57*, 827–834.

[28] A. R. C. Bredar, A. L. Chown, A. R. Burton, B. H. Farnum, *ACS Applied Energy Materials* **2020**, *3*, 66–98.

[29] C. Wang, L. Zhang, H. Xie, G. Pastel, J. Dai, Y. Gong, B. Liu, E. D. Wachsman, L. Hu, *Nano Energy* **2018**, *50*, 393–400.

[30] B. D. Paulsen, S. Fabiano, J. Rivnay, **2021**.

[31] W. Lai, S. M. Haile, *Journal of the American Ceramic Society* **2005**, *88*, 2979–2997.

[32] S. M. Park, J. S. Yoo, *Analytical Chemistry* **2003**, *75*, 455–461.

[33] M. E. Orazem, B. Tribollet, *Electrochemical Impedance Spectroscopy*, John Wiley & Sons, Inc., **2008**.

[34] B. Y. Chang, S. M. Park, *Annual Review of Analytical Chemistry* **2010**, *3*, 207–229.

[35] G. S. Popkirov, R. N. Schindler, *Review of Scientific Instruments* **1992**, *63*, 5366–5372.

[36] A. S. Baranski, T. Krogulec, L. J. Nelson, P. Norouzi, *Analytical Chemistry* **1998**, *70*, 2895–2901.

[37] S. H. Han, J. Rho, S. Lee, M. Kim, S. I. Kim, S. Park, W. Jang, C. H. Lee, B.-Y. Chang, T. D. Chung, *Analytical Chemistry* **2020**, *92*, 10504–10511.

[38] J. E. Garland, C. M. Pettit, D. Roy, *Electrochimica Acta* **2004**, *49*, 2623–2635.

[39] G. S. Popkirov, R. N. Schindler, *Review of Scientific Instruments* **1993**, *64*, 3111–3115.

[40] D. Shoup, A. Szabo, *Journal of Electroanalytical Chemistry* **1982**, *140*, 237–245.

[41] E. J. E. Stuart, Y. G. Zhou, N. V. Rees, R. G. Compton, *RSC Advances* **2012**, *2*, 6879–6884.

[42] E. Laborda, A. Molina, C. Batchelor-McAuley, R. G. Compton, *ChemElectroChem* **2018**, *5*, 410–417.

[43] P. Q. Li, A. Piper, I. Schmueser, A. R. Mount, D. K. Corrigan, *Analyst* **2017**, *142*, 1946–1952.

[44] P. Los, G. Zabinska, A. Kisza, L. Christie, A. Mount, P. G. Bruce, *Physical Chemistry Chemical Physics* **2000**, *2*, 5449–5454.

[45] P. G. Bruce, A. Lisowska-Oleksiak, P. Los, C. A. Vincent, *Journal of Electroanalytical Chemistry* **1994**, *367*, 279–283.

[46] A. Lasia, *Electrochemical Impedance Spectroscopy and its Applications*, Springer New York, **2014**.

[47] A. J. Bard, L. R. Faulkner, *Electrochemical Methods: Fundamentals and Applications*, 2nd ed., John Wiley & Sons, **2001**.

[48] C. Renault, S. G. Lemay, *ChemElectroChem* **2019**, 69–73.

[49] S. E. Fosdick, M. J. Anderson, E. G. Nettleton, R. M. Crooks, *Journal of the American Chemical Society* **2013**, *135*, 5994–5997.

[50] Z. Deng, R. Elattar, F. Maroun, C. Renault, *Analytical Chemistry* **2018**, *90*, 12923–12929.

[51] A. Boika, S. N. Thorgaard, A. J. Bard, *Journal of Physical Chemistry B* **2013**, *117*, 4371–4380.

[52] A. Yakushenko, D. Mayer, J. Buitenhuis, A. Offenhäusser, B. Wolfrum, *Lab on a Chip* **2014**, *14*, 602–607.

[53] R. McElreath, *Statistical Rethinking: A Bayesian Course with Examples in R and Stan*, Chapman and Hall/CRC, **2015**.

[54] Y. Wang, J. G. Limon-Petersen, R. G. Compton, *Journal of Electroanalytical Chemistry* **2011**, *652*, 13–17.

[55] R. G. Compton, C. E. Banks, *Understanding Voltammetry*, 3rd, World Scientific, **2018**.

Chapter 4

Measurement of the Impedance Spectra of Individual Pseudocapacitive Nanoparticles

Adapted with permission from: Roehrich, B.; Sepunaru, L. Impedimetric Measurement of Exchange Currents and Ionic Diffusion Coefficients in Individual Pseudocapacitive Nanoparticles. *ACS Measurement Science Au* **2024**, 10.1021/acsmeasuresciau.4c00017.

4.1 Introduction

Nanoparticles are ubiquitous in electrochemistry, but understanding their intrinsic properties is difficult using conventional electroanalytical techniques. This is because the properties of individual electrochemically active particles of the same material may differ greatly from one another due to morphology, crystallinity, composition, or other factor.[1, 2] Typical bulk characterization techniques mask these differences and provide an ensemble-averaged response. Instead, single-entity electrochemistry studies particles one by one – linking their individual properties to that of the ensemble in a bottom-up

approach to further improve the material's properties.[3–7] Motivated by this, several groups have begun applying the scanning electrochemical cell microscope (SECCM) towards the study of individual electroactive particles.[8–11] In SECCM measurements, a nano- or micro-pipette is filled with electrolyte, equipped with a counter electrode, and positioned above a conductive substrate which serves as the working electrode.[8, 12] A bias is applied between the two electrodes and the pipette is slowly lowered towards the substrate by a piezoelectric positioner until the electrolyte wets the substrate and current flows across the interface. The droplet formed between the tip of the pipette and the substrate comprises a microscopic electrochemical cell which, when interrogated electrochemically using a low-noise amplifiers,[13, 14] yields a response which is unique to that particular region of the substrate.[15] For single-particle studies, nanoparticles are dispersed on the conductive substrate prior to the SECCM experiment. When the droplet contains an electroactive nanoparticle, that individual particle's thermodynamic and kinetic properties can be measured. Because of this simple and elegant mode of operation, SECCM has been applied to study a wide range of electroactive materials including the activity of various electrocatalysts,[2, 16–18] charge storage in individual pseudocapacitors,[19, 20] and the intercalation of ions in battery active materials.[21–23] Its powerful compatibility with complementary microstructure imaging and characterization techniques which measure topography, morphology, or composition can offer unprecedented insight into structure-property relationships at the nanoscale.[17, 24–28]

To date, the vast majority of SECCM experiments have relied on either amperometry (measuring current at a constant potential) or voltammetry (measuring current as the potential is swept) for their electrochemical analysis. In both techniques, however, the measured current is inherently a convolution of several independent processes – including electron transfer, double-layer capacitance, and mass transport, amongst others – and separating their contributions is challenging. Electrochemical impedance spectroscopy (EIS), in contrast, readily deconvolutes between these phenomena based on their relative timescales.[29–31] The advantages of EIS are particularly pronounced in systems with a strong coupling between electronic and ionic conductivity, such as those found in batteries and supercapacitors, due to its ability to decouple the relative rates of electron and ion transport.[32] In EIS, the electrochemical cell is perturbed by a small-amplitude, sinusoidal (alternating current, AC) voltage. The impedance (Z) of the cell is intimately related to the frequency of the AC sine wave – at high frequencies, Z is dictated by "fast" processes such as double layer formation and rapid electron transfer reactions, while at low frequencies Z is determined by the rates of sluggish mass transport or pseudocapacitive intercalation.

Here, we demonstrate the measurement of impedance spectra of individual pseudocapacitive nanoparticles. We chose Prussian blue (PB) as a model system – while first reported as a dye in the early 1700s,[33] Prussian blue (and its derivatives) has attracted recent interest as a low-cost material for sodium- and potassium-ion battery cathodes due to its coupling of $Fe^{II/III}$ redox with alkali metal ion intercalation.[34–36] The kinetics of

the redox reaction (i.e., the exchange current) and the rate which ions diffuse through the PB lattice are both critically important to the energy-storage performance of the material, yet are not well understood at the nanoscale. In particular, and despite extensive work over the past two decades, significant debate remains in the literature over the diffusion coefficient of sodium ions within the PB lattice – reported values range over a staggering seven orders of magnitude.[37] To explore this, we measured the impedance spectra of isolated Prussian blue nanocubes using a multi-sin, fast Fourier transform (FFT) technique.[38] This technique enables rapid measurement (within seconds) of the impedance spectra, mitigating potential thermodynamic and mechanical drifts which could arise during the SECCM measurement process. We show that the impedance spectrum of a single Prussian blue nanoparticle deconvolutes its electron transfer reaction and ion mobility kinetics. By recording spectra of over a dozen particles in the SECCM configuration, we can evaluate the intrinsic heterogeneity in the exchange current and ion diffusivity and show that these rates can vary by one to two orders of magnitude, respectively, even amongst particles synthesized in the same batch.

4.2 Impedance Measurements in the Scanning Electrochemical Cell Microscope

Prussian blue nanocubes were synthesized via the hydrothermal method[39] and drop-cast on a glassy carbon (GC) substrate to form a highly diluted surface layer. The

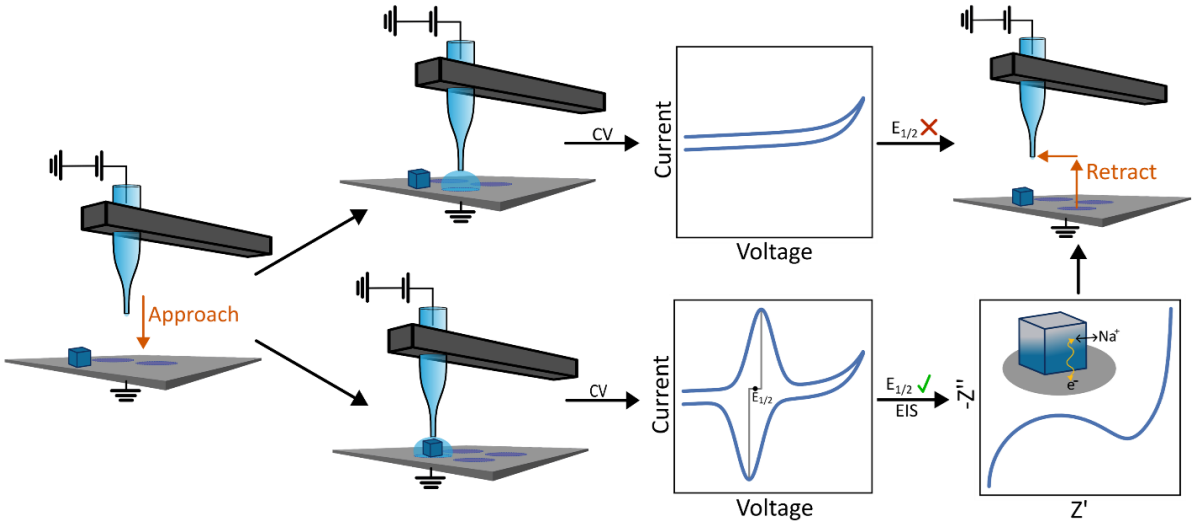

Figure 4.1: Steps required for single particle FFT-EIS measurements. The SECCM probe is moved towards the surface until its electrolyte wets the surface. After contact, a cyclic voltammogram is recorded and analyzed to determine if it contains a pair of oxidation and reduction waves. If it does, $E_{1/2}$ is determined as the midpoint between the two peak potentials and applied as the DC bias for a subsequent EIS measurement. After acquiring the impedance spectrum (or if no peaks were detected in the CV), the probe is retracted and moved to the next location.

morphology of the particles and their dispersion on GC was characterized by SEM (Figure 4.10). We performed SECCM using borosilicate glass pipettes which were pulled to a tip diameter of 3-5 μm (Figure 4.9), filled with 0.1 M NaCl, and fitted with an Ag/AgCl quasi-reference counter electrode (the potential of the Ag/AgCl wires in 0.1 M NaCl were typically +44 mV vs SCE). The general steps performed in each SECCM experiment are shown in Figure 4.1. At a series of predefined locations above the substrate, the micropipette was slowly lowered by a piezoelectric positioner until the droplet contacted the surface.[40] Movement was immediately halted, then a cyclic voltammogram was recorded and automatically analyzed by the controlling Python program. If the program determined that a PB nanoparticle was present (based on the presence of reversible redox

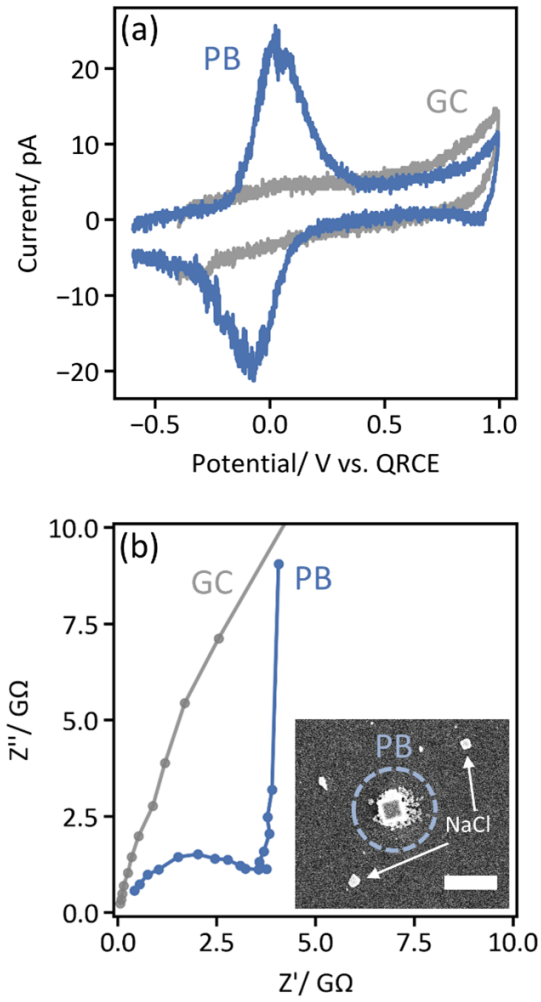

Figure 4.2: The impedance spectrum of a single Prussian blue nanoparticle is clearly distinguishable from the background. (a) Cyclic voltammograms (1 V/s) recorded when the SECCM probe was positioned over the bare glassy carbon substrate ("GC", gray) and when the droplet encompassed a Prussian blue nanoparticle ("PB", blue). The redox waves visible for the PB NP are attributed to the $Fe^{II}Fe^{II}/Fe^{II}Fe^{III}$ couple, i.e., the transition between Prussian white and Prussian blue. (b) Impedance spectra recorded using the FFT technique at the same locations. $E_{1/2}$ (-20 mV vs the Ag/AgCl QRCE for this particle) was applied as the DC bias for both EIS experiments, and the impedance was measured at 18 frequencies between 1 Hz and 1 kHz with an AC amplitude of 50 mV_{pp} (Figure 4.8). The impedance magnitudes recorded on the PB NP falls in the range of GΩ, yet are still significantly smaller than those recorded on the bare substrate at the same frequencies. Inset: an SEM image of the same PB NP. Salt deposits left behind by nearby SECCM hopping points are indicated. The scale bar is 2 μm.

waves, *vide infra*), an impedance spectrum was recorded before the pipette was retracted and moved to the next location.

Cyclic voltammograms obtained when the SECCM probe was positioned over an individual PB nanocube contained characteristic peaks associated with quasi-reversible, surface-bound, redox activity. The SECCM held the substrate at -600 mV for 5 s after contact was established. If the PB NP was present, this step reduced the particle into the $Fe^{II} - Fe^{II}$ (Prussian white) state. Then, the voltage was swept to +1 V vs Ag/AgCl and back at a scan rate of 1 V/s (the high scan rate was chosen to minimize the total time of the SECCM experiment). No redox features were observed if the micropipette was in contact with the bare glassy carbon substrate (Figure 4.2a, gray), while a pair of quasi-reversible waves is visible if the droplet contained a PB nanoparticle (Figure 4.2a, blue). These peaks correspond to the one-electron oxidation of the particle to the $Fe^{II} - Fe^{III}$ (Prussian blue) state. The half-wave potential of this reaction (for this particle, -20 mV vs Ag/AgCl|0.1M NaCl or 30 mV vs SCE) is similar to that previously reported for sodium-containing Prussian blue.[41] Furthermore, the symmetric shape of the waves is as expected for quasi-reversible, surface-bound electrochemistry.[42, 43]

The impedance spectrum of the same nanoparticle contains features which deconvolute the electronic and ionic components that underly the overall electrochemical reaction. EIS was performed using a multi-sin waveform which contained 18 frequencies spanning 1 Hz to 1 kHz. We chose to use the multi-sin, fast Fourier transform technique to minimize the acquisition time of each spectrum – a full spectrum, averaged over 5 cycles of the

lowest frequency, was measured in 5 s.[38, 44, 45] The waveform (Figure 4.8) was normalized to have an amplitude of 50 mV_{pp} and applied with a DC bias set as $E_{1/2}$ from the NP's cyclic voltammogram. The measured impedance spectrum, when represented as a Nyquist plot, contains a semicircle in the high-frequency regime while trending towards large imaginary impedance in the low-frequency limit (Figure 4.2b). These features are characteristic of an ion-intercalating material and qualitatively match those observed in bulk PB films.[46] Because the reduction/oxidation reactions occur at iron centers within the Prussian blue crystal lattice, electron transfer must be accompanied by (sodium) ion intercalation to maintain charge neutrality. At high frequencies, the current response (and thus the measured impedance) is limited by electron transport to surface and near-surface iron centers to which ion transport is facile. At lower frequencies, sodium ions have more time to diffuse further into the crystal lattice and the impedance is dictated by their transport. At all but the highest frequencies we examined (where solution resistance dominates), the impedance measured in the presence of the PB NP (Figure 4.2b, blue) is much lower than that measured in its absence (Figure 4.2b, gray). As current flows through the path of least impedance, this means the contribution of the background to the measured impedance spectrum is small.

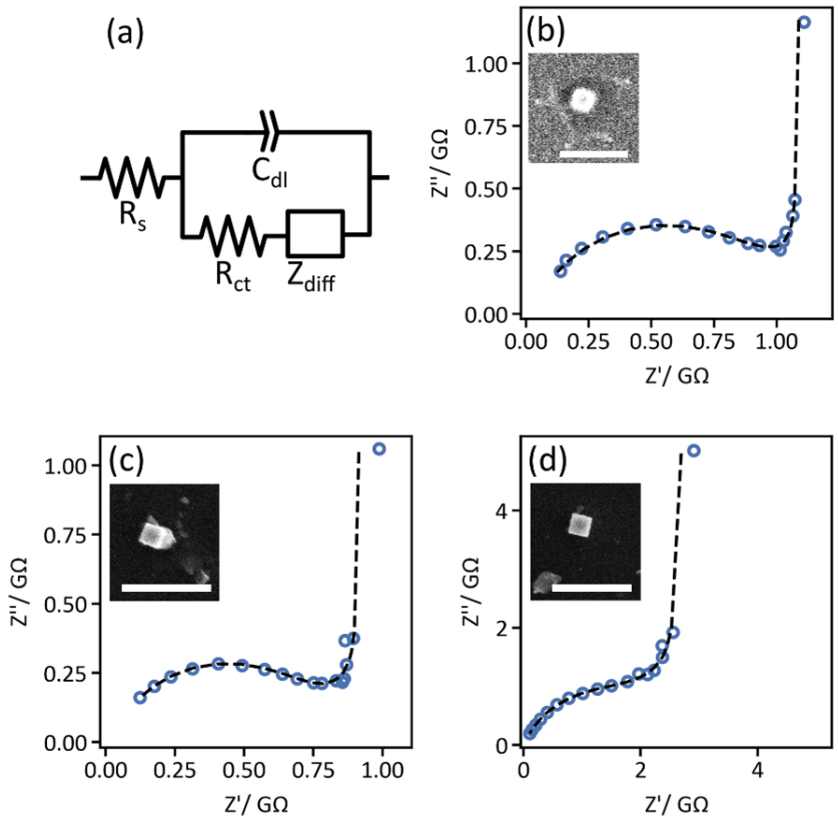

Figure 4.3: Impedance spectra measured from individual Prussian blue nanocubes are described well by a simple equivalent circuit model. (a) The equivalent electronic circuit used for fitting impedance spectra, with resistors accounting for the solution (R_s) and charge-transfer (R_{ct}) resistances, a constant phase element representing the double-layer capacitance (C_{dl}), and a diffusion element modelling the transport of sodium ions within the nanocube (Z_{diff}).[47] (b-d) EIS data (open circles) and equivalent circuit fits (dotted curves) for three representative PB nanoparticles. Insets are SEM images of each particle which produced the respective impedance spectrum (scale bars are 2 μm).

4.3 Comparison of Impedance Spectra Between Particles

We used equivalent circuit modelling to extract relevant physical parameters from each individual Prussian blue nanoparticle. The simple, four-element equivalent circuit (Figure 4.3a) accounts for the bulk solution resistance (R_s), the double-layer capacitance

(C_{dl}), the charge-transfer resistance between the glassy carbon electrode and the PB NP (R_{ct}) and diffusion of sodium ions within the PB NP (Z_{diff}). The double-layer capacitance was modelled as a constant phase element because it includes contributions from both the nanoparticle and the glassy substrate support – their capacitances, while different, are parallel and thus indistinguishable pathways for current to flow. The value of α, which dictates the phase of the constant phase element, was typically 0.8 due to these bifurcated capacitive pathways (an ideal capacitor has $\alpha = 1$). Meanwhile, to approximate the diffusion of ion intercalation in our cubic particles, we adopted a finite-space Warburg element model for a spherical particle which accounted for the complementary effects of ion diffusion and pseudocapacitive intercalation.[47, 48] The net equivalent circuit (Figure 4.3a) provided excellent fits ($R^2 > 0.99$) to each impedance spectrum we measured from 16 individual PB (three representative particles are shown in Figure 4.3b-d, the full data set is shown in Figures 4.11, 4.13, and Table 4.12).

Based on the charge-transfer resistance (R_{ct}) and diffusional impedance (Z_{diff}) obtained from each particle's impedance spectrum, we were able to estimate the exchange current density (j_0) and ionic diffusion coefficient (D_{Na}). The exchange current density, j_0 was calculated from the fitted value of R_{ct} and the contact area ($A_{contact}$, estimated by SEM) between the individual nanoparticle and the carbon substrate:

$$R_{ct} = \frac{RT}{nFA_{contact}j_0} \tag{4.1}$$

Where R is the gas constant, T is temperature, n is the number of electrons (1), and F is Faraday's constant. We found that j_0 fell in the range of 10-200 Am^{-2}. As a

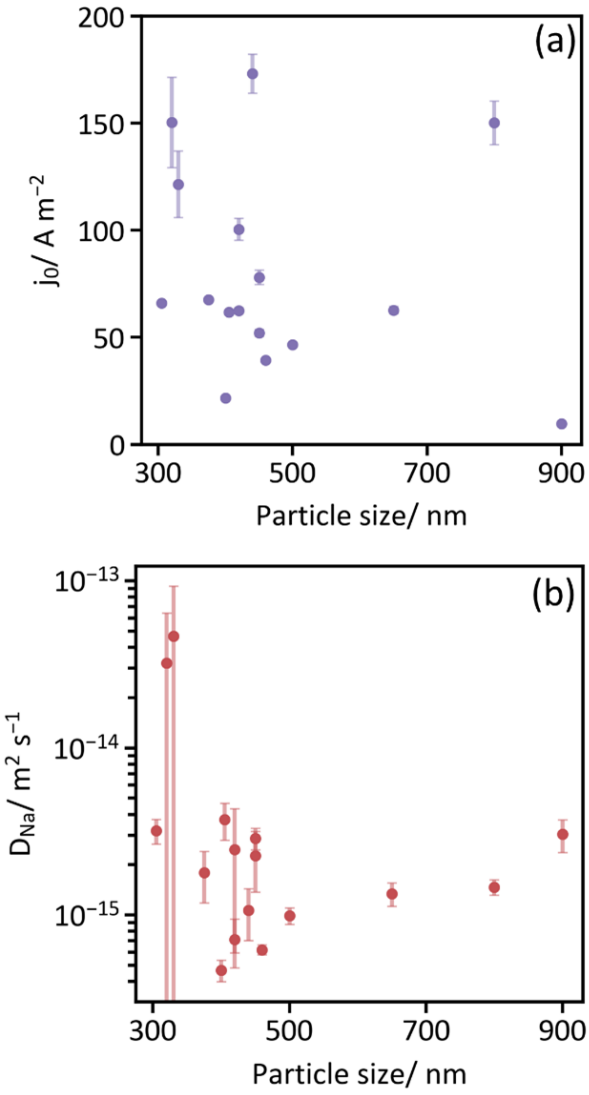

Figure 4.4: Exchange current densities and sodium ion diffusivities vary by more than an order of magnitude between particles but are not correlated to particle size. (a) Exchange current density (j_0, normalized to particle-substrate contact area, estimated by SEM) and (b) diffusion coefficient (D_{Na}) as a function of particle size. Here, particle size refers to the average of the two side lengths estimated by SEM. Error bars represent the uncertainty associated with the equivalent circuit fit.

point of comparison, these values are on the order of the highest reported exchange current densities for lithium-ion cathode materials.[49] The high j_0 measured for PB may be due to its relatively higher conductivity and enhanced electrochemical reversibility.

Likewise, the diffusional impedance was parameterized into an effective resistance R_d and an intercalation capacitance C_d (which is strongly correlated with the charge passed in the voltammogram as shown in Figure 4.14), yielding a time constant τ from which the diffusion coefficient can be calculated:[50, 51]

$$\tau = R_d C_d \tag{4.2}$$

$$D_{Na} = \frac{l^2}{3\tau} \tag{4.3}$$

where l is the characteristic diffusion length. In this case, we set l=20 nm for all particles regardless of particle size due to several recent reports showing that the diffusion length in Prussian blue particles is likely on the order of tens of nanometers.[37, 52] We note that choosing a different value of l would shift the distribution of diffusion coefficients to higher or lower values without changing their dispersity, as shown by Equation 4.3. Indeed, inconsistent choices of l are likely a major reason for the wide range of diffusion coefficients reported in the literature. With this choice of l, the values of D_{Na} we obtained ($\sim 10^{-13} - 10^{-15} \mathrm{m^2 s^{-1}}$) fall well within the broad range of previously reported values.[37]

By comparing the exchange current densities (Figure 4.4a) and solid-state diffusion coefficients (Figure 4.4b) obtained from over a dozen individual nanocubes, we can begin to assess the inherent heterogeneity in these parameters across the material. Surprisingly, although all Prussian blue particles originated from the same synthetic batch, j_0 and D_{Na} vary by factors of 20 and 100, respectively. This implies that in a hypothetical battery cathode, one active PB particle can undergo reversible electrochemistry up to twenty times faster than its neighbor, or may transport sodium ions one hundred times

slower than a better-performing particle elsewhere in the electrode. Evidently, neither j_0 nor D_{Na} trend with particle size (Figure 4.4), nor are they strongly correlated to each other (Figure 4.15). This phenomenon mirrors a recent observation in individual mesoporous NMC522 particles by Min et. al, who found no correlation between either electron transfer or diffusion timescales with secondary particle size.[53] The authors suggested the particle-to-particle variability observed was due to either different degrees of electrolyte penetration within the secondary particle or inherent heterogeneity between the primary particles.[53] As we are dealing with primary particles which presumably have little electrolyte permeation, our results suggest such variability is inherent. While further work is needed to understand the physical origin of these differences, significant improvements can be made in the active material if particles with high exchange currents and ionic diffusivities can be targeted synthetically.

We performed several experiments to verify the stability and linearity of our measurements. We first tested the linearity of our spectra by measuring sequential impedance spectra with AC amplitudes increasing from 10 – 200 mV_{pp} on two individual particles (Figure 4.5). For both particles, the spectra overlap regardless of AC amplitude and do not contain significant distortions at high amplitudes, verifying that the spectra measured herein at 50 mV_{pp} are due to a linear current-voltage relationship. To verify the stability of our impedance spectra, we took sequential measurements at single particles. So long as the particle was in stable electrical contact with the support, the measured impedance spectra did not significantly drift over a one-minute time span

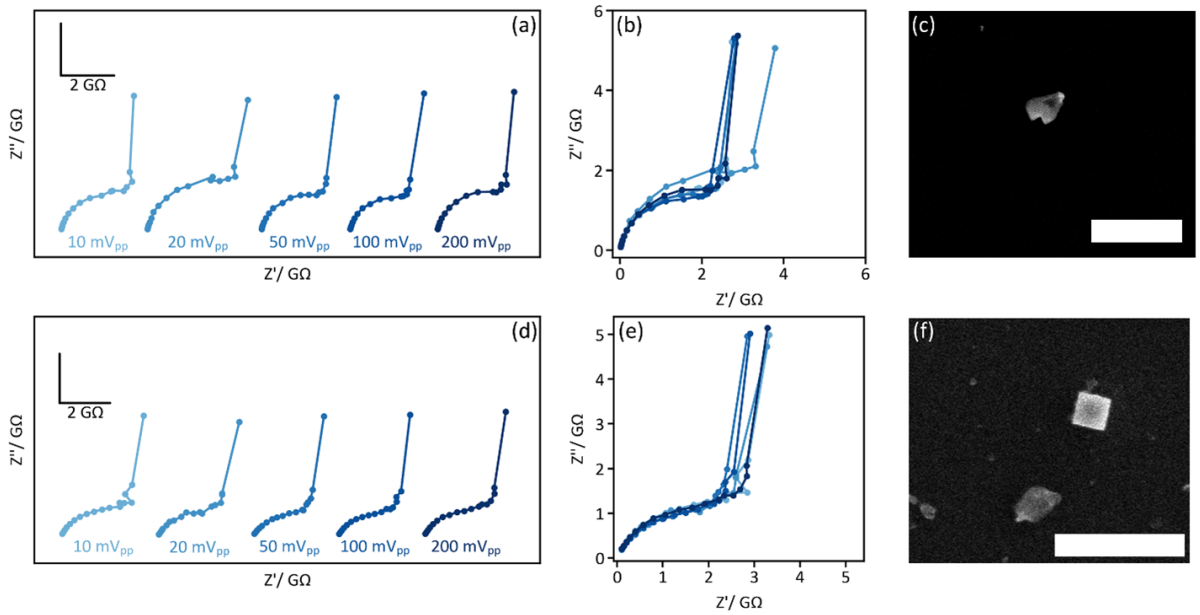

Figure 4.5: The measured impedance spectra are not significantly affected by the choice of AC amplitude in the range of 10 – 200 mV_{pp}. We measured impedance spectra on two particles with amplitudes of 10, 20, 50, 100, and 200 mV_{pp} (a, d). All five spectra overlap with one another (b, e) and do not display an obvious trend with AC amplitude or noticeable distortions at high amplitudes, either of which would suggest a non-linear response. The particles interrogated are shown in (c) and (f), scale bars are 2 μm.

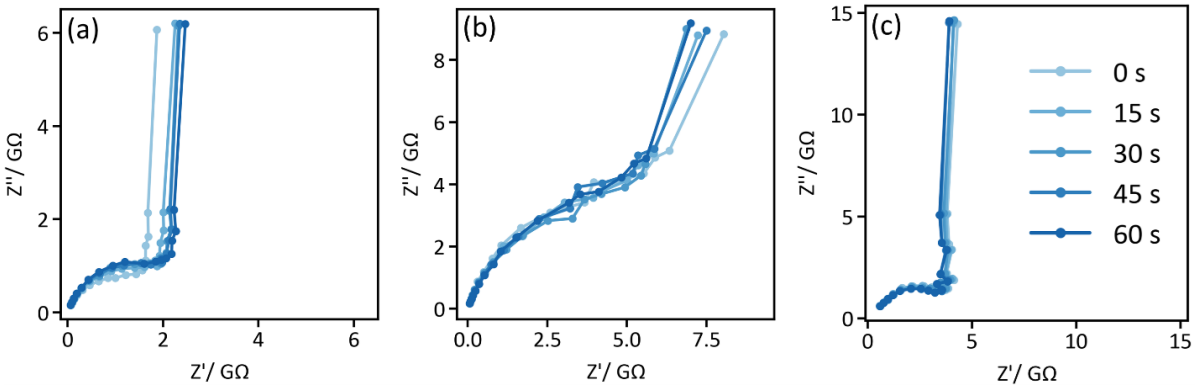

Figure 4.6: We measured impedance spectra every 15 s for a total of 60 s for three different particles. While the impedance of the first particle (a) drifted a small amount, the other two (b, c) were stable over the one-minute measurement. The drift visible in (a) is small compared to that observed in other particles (*vide infra*), which were excluded from analysis.

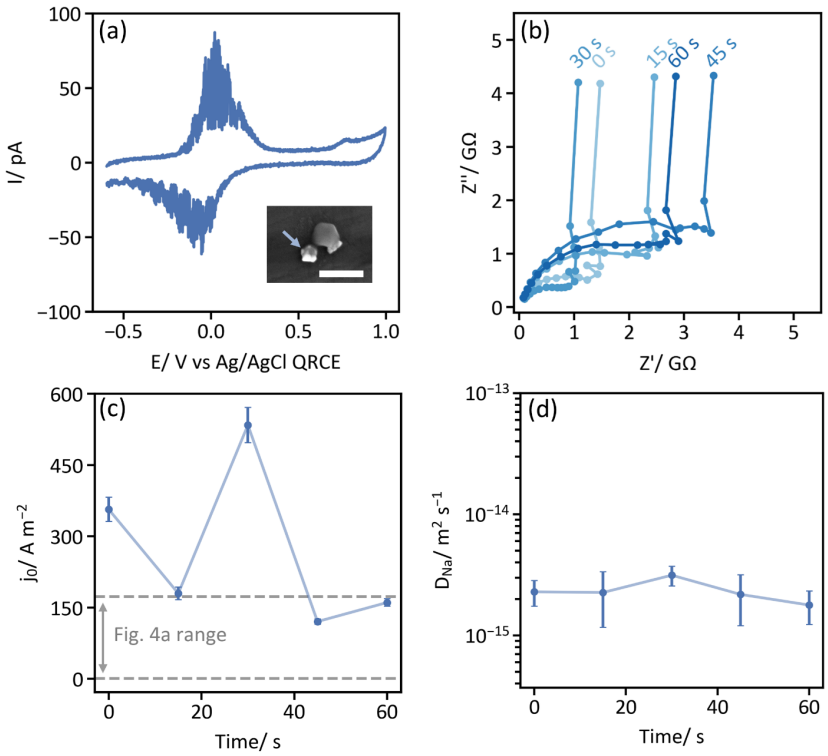

Figure 4.7: Cyclic voltammetry (a) and time-resolved impedance (b) of a PB nanoparticle which evidently had poor electrical contact with the glassy carbon substrate. Noisy spikes are visible in the voltammogram, while the impedance spectrum shifts sporadically in time. This is also visible in the fitted values of (c) j_0, which shift randomly across a wide range, while values of (d) D_{Na} remain relatively constant. Interestingly, the apparent values of j_0 for this small ($l \approx 240$nm) nanoparticle are much higher than those shown in Figure 4.4a, the range of which is represented in (c). This particle and several others which showed similarly noisy voltammograms were excluded from our analysis. Error bars in (c) and (d) reflect the uncertainty in the equivalent circuit fit.

(Figure 4.6). While collecting our data set, we measured several particles which did, however, display significant drift - an example of a particle with poor electrical contact and a non-stationary impedance is shown in Figure 4.7. The highly fluctuating values of R_{ct} observed in that case suggest that the measured resistance is influenced not only by the electrochemical rate constant as discussed above, but also by a contact resistance between the particle and the glassy carbon substrate. These resistances are in series and

cannot be readily deconvoluted, meaning that differing particle-electrode contact qualities may contribute to the heterogeneity observed in j_0.[54] Still, the values of D_{Na} were constant within error, meaning that their heterogeneity seen in Figure 4.4B is not affected by the contact resistance but is rather intrinsic to the particles themselves. While the contact resistance remains an open question, these results taken together validate the stationarity and linearity of our EIS data and support their physical interpretability.

4.4 Conclusions

In conclusion, we have demonstrated the rapid measurement of the impedance spectra of individual, isolated, pseudocapacitive Prussian blue nanoparticles using SECCM. Despite the impedance falling in the range of GΩ, the impedance spectrum of a single particle is easily distinguishable from the background, and the spectra are stationary and linear when measured using the multi-sin, FFT method. Single-particle spectra are well-described by an equivalent circuit incorporating both electronic conductivity and ion transport within the particle, yielding values for the exchange current density and ionic diffusivity for each nanoparticle. We found that these parameters vary by more than an order of magnitude, even amongst particles from the same synthetic batch.

We foresee EIS coupled to SECCM as a valuable tool for future single-particle studies. It should prove more generally applicable than related optical measurements of single nanoparticle impedance,[52, 55, 56] which rely on the material's optical properties changing with voltage – a material-specific phenomenon which may be small or nonexistent

for some materials. Our method, which uses current as a direct measurement of the impedance, is universal to any electroactive material. Meanwhile, the range of spatial resolutions possible in SECCM will enable measurements on regions of particles, primary particles, and small ensembles of particles to complement established secondary-particle microscale measurements.[1, 53, 57, 58] When combined with the high-throughput nature of SECCM (particularly if combined with "smart" probe positioning to target isolated nanoparticles),[22, 59] these benefits will enable rapid screening of structure-property relationships at the single-particle level for batteries, pseudocapacitors, and electrocatalysts.

4.5 Supporting Information

4.5.1 Experimental

Preparation of Prussian Blue Nanocubes: All materials were used as received without further purification. Sodium ferrocyanide decahydrate (0.972g, Acros Organics) was dissolved in 100 mL MilliQ water. 2 mL 37% HCl (Fisher) was added and the solution was stirred at 60 °C for 4 hours.[39] The deep blue precipitate was recovered by filtration, washed with water and ethanol for three times each, then dried in a vacuum oven at 60 °C overnight.

To prepare samples for SECCM analysis, NPs were suspended at 0.1 mg/mL in water. The suspension was dispersed using a high-power tip sonicator for 20 s, then diluted by

a factor of 3 with isopropanol. 10 μL of this solution were dropped onto a clean glassy carbon substrate (Ted Pella) and allowed to dry at 50 °C. Glassy carbon substrates were prepared by polishing sequentially on 1, 0.3, and 0.05 μm alumina then on a clean, wet polishing pad before sonication in isopropanol and water.

Pipette Fabrication: Pipettes were fabricated from filamented borosilicate capillaries (BF120-94-15, Sutter Instruments) using a Sutter P-2000. The following parameters were used to pull pipettes of approximately 3 μm tip diameter: HEAT 350 FIL 3 VEL 40 DEL 220 PULL 0. The radii of several representative pipettes were confirmed using SEM (Figure 4.9).

Ag/AgCl wires were created by soldering a short length of silver wire (0.005", 99.9%, Thermo Scientific) to a gold connector pin. Wires were soaked overnight in household bleach (Clorox, 3.5%) to form an AgCl coating, then rinsed with water. The wires' potentials were measured in 100 mM NaCl and found to be 43.76 $\pm$ 0.54 mV vs saturated calomel electrode (SCE, error represents the standard deviation between four independent wires). Immediately prior to each SECCM experiment, a pipette was filled with electrolyte (100 mM NaCl) using a MicroFil needle. An Ag/AgCl wire was inserted and secured in place using heat-shrink tubing, which also served to minimize electrolyte evaporation from the back of the pipette.

Scanning Electrochemical Cell Microscope: SECCM was performed using a home-built instrument which ran using a custom Python program (available at https://github.com/SepLabUCSB/SECM). The substrate of interest was placed on an

XYZ microscope stage which was equipped with coarse piezoelectric positioners on the Z axis (for rough positioning of the stage while approaching the pipette) and on the Y axis (for moving the probe to new locations on the substrate). The pipette was mounted above the stage and connected to a closed-loop XYZ piezoelectric positioner (Newport XYZ100SG) for fine control. During experiments, the substrate and pipette tip were enclosed in a plastic container, fabricated from the conical end of a 50 mL centrifuge tube. Humidified argon was flowed into an inlet in the container (and out through the top) to maintain a humid environment near the pipette tip and minimize droplet evaporation.[15]

All electrochemical measurements were performed using a HEKA EPC-10 USB. The Ag/AgCl quasi-reference counter electrode within the pipette was grounded and the (glassy carbon) substrate served as the working electrode. In an SECCM experiment, the GC substrate was mounted to an SEM stub using copper tape and biased at -600 mV. The EPC-10 "C-fast" function was run after the probe was mounted but prior to beginning the approach towards the substrate. This function measures the stray capacitance in circuit (arising from the cables, amplifier, pipette glass, etc.), afterwards, the potentiostat uses a compensation circuit to eliminate this capacitance from measurements. We recorded C-fast when the probe was not in contact with the surface to assure the compensation did not eliminate the double layer or electrochemical capacitance of the surface. The probe was moved towards the substrate in 10 nm steps (equivalently, 0.8 μm/s), the current was recorded at each step, and probe movement was halted as soon as the current magnitude

rose above a preset threshold (typically 8 pA) which indicated the droplet had wet the surface. Then, cyclic voltammetry was performed at a scan rate of 1 V/s and analyzed in real time by the controlling Python program. The program searched for oxidation and reduction peaks with prominences greater than 5 pA. If both oxidation and reduction peaks were detected (suggesting the presence of a PB particle), the half wave potential of the peaks was calculated and applied as a DC bias, and an impedance spectrum was recorded using the Fourier transform technique (*vide infra*). Then, the pipette was retracted from the surface by 5 μm and moved above the next point. Typically, a 16 x 16 grid of points spanning 75 μm x 75 μm was acquired in a single experiment. The stage was subsequently automatically moved using the coarse Y-axis piezoelectric motor to acquire a new grid of datapoints in a new location. After a series of SECCM experiments, the GC substrate was transferred to a scanning electron microscope (SEM, ThermoFisher Apreo C) for imaging.

Fast Fourier Transform Impedance Spectroscopy: Impedance spectroscopy was performed using the FFT technique, introduced by Popkirov and Schnidler.[38] Briefly, an AC waveform containing 18 frequencies of interest (spanning 1 Hz to 1 kHz) was generated by summing together sine waves at each frequency,

$$v(t) = \sum_j a_j \sin 2\pi f_j t + \phi_j \tag{4.4}$$

Where a_j is the amplitude and ϕ_j is the phase at each frequency f_j. While phases were randomized, each sine wave's amplitude was optimized to maximize signal-to-noise.[44] The resulting waveform is shown in the Supporting Information (Figure 4.8). This wave-

form was added to a DC bias (determined as the midpoint between the oxidation and reduction peaks detected in a particle's cyclic voltammogram and filtered at 100 kHz by a 2-pole Bessel filter. The voltage and current (filtered by sequential 10 kHz and 5 kHz 6-pole Bessel filters) were recorded for 5 s and Fourier transformed to obtain an impedance spectrum which averaged over 5 complete cycles of the lowest frequency, 1 Hz. The low-pass filters we applied caused a small phase shift at the highest measured frequencies, which we corrected for by calibrating against the spectrum of a known 10 MΩ resistor as we previously described.[45] Impedance spectra were fit using MEISP software (Kumho Petrochemical, Ltd.). We represent all impedance spectra as Nyquist plots, where Z' is the real component and Z" is the negative of the imaginary component of the impedance.

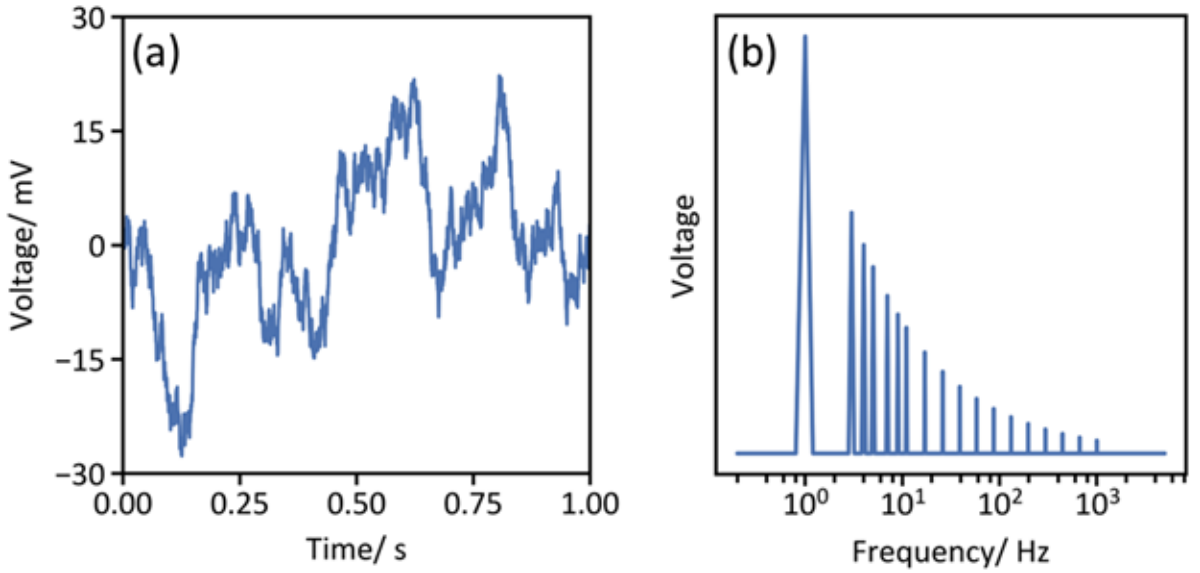

Figure 4.8: Representations of the waveform used for FFT-EIS measurements in the (a) time and (b) frequency domains. The waveform was scaled to have a 50 mV peak-to-peak amplitude in the time domain. The perturbation amplitude was a function of frequency in order to maximize S/N, as the electrochemical cell has higher impedance at low frequencies. Thus, a larger voltage at low frequency and a smaller voltage at high frequency are necessary to make the current output similar at all frequencies.1 The phase at each frequency was randomized.

4.5.2 Particle and Electrode Characterization

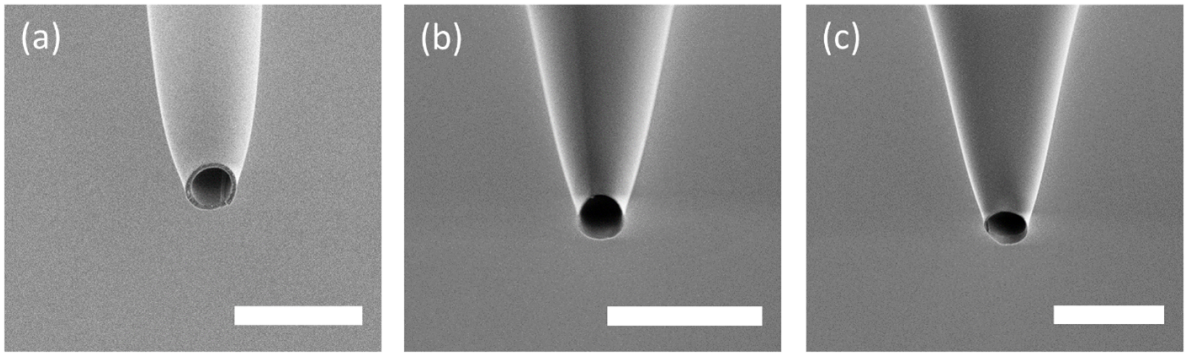

Figure 4.9: (a-c) Scanning electron micrograph of three representative micropipettes. Scale bars represent 10 μm. The pipette was pulled from 1.2 mm O.D., 0.94 mm I.D., filamented borosilicate glass (BF120-94-15, Sutter) using a P-2000 pipette puller. The pull parameters were HEAT 350 FIL 3 VEL 40 DEL 220 PULL 0.

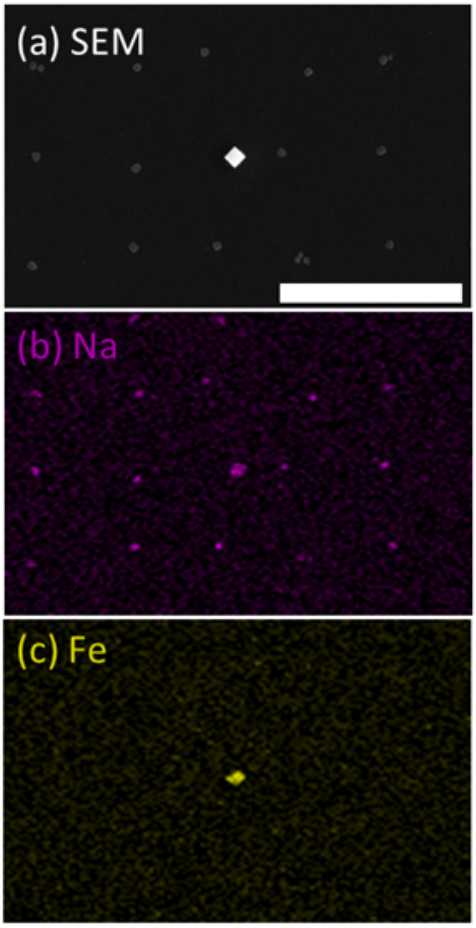

Figure 4.10: Energy-dispersive X-ray spectroscopy (EDS) distinguishes between Prussian blue nanoparticles and the grid of NaCl deposits left behind by SECCM experiments. Images were acquired using a ThermoFisher Apreo C scanning electron microscope operating at 10 kV with a current of 3.2 nA. (a) Under these imaging conditions the PB particle has high contrast compared to the (carbon) background and the NaCl deposits in the secondary electron micrograph. (b) Spatially-resolved EDS confirms the presence of sodium across the grid of locations probed in the SECCM experiment. A large sodium signal is also seen at the particle's location due to the sodium intercalated in its crystal lattice. (c) Iron is only detected at the particle, distinguishing it from similarly-sized salt deposits.

4.5.3 Data from 16 Prussian Blue Nanoparticles

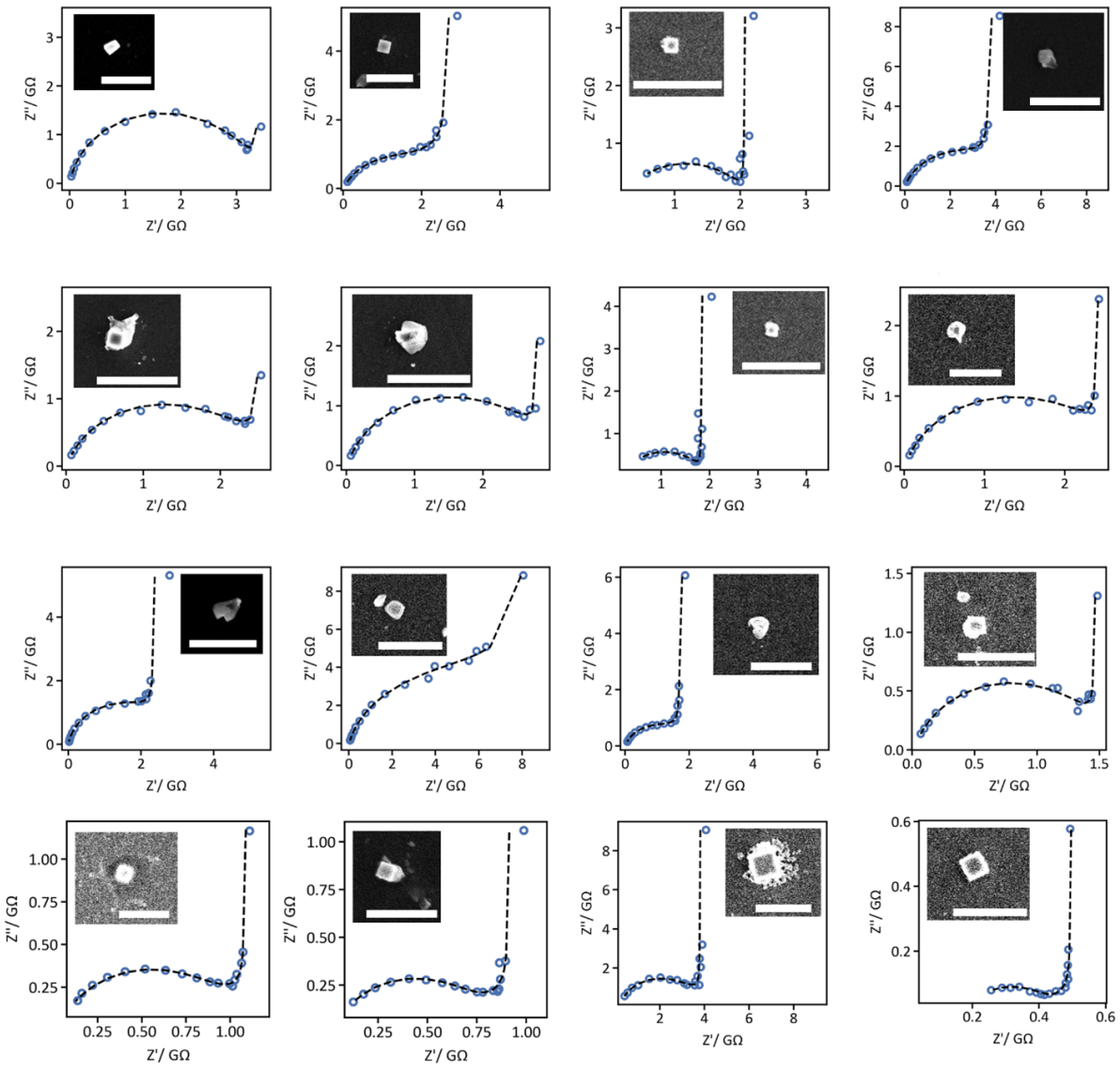

Figure 4.11: Impedance spectra (open circles), equivalent circuit fits (dashed curves), and SEM images (insets) of the 16 individual nanoparticles studies herein. All SEM scale bars are 2 μm.

Side 1 Length (nm)	Side 2 Length (nm)	R_s (MΩ)	R_{ct} (GΩ)	Q_{dl} (pF $s^{\alpha-1}$)	α	R_d (GΩ)	C_d (pF)	D (m^2 s^{-1})	j_0 (A m^{-2})
650	650	23.82	0.97	5.47	0.77	0.742	133.91	1.34E-15	62.7
330	330	189.17	1.94	2.02	0.74	0.059	48.43	4.66E-14	121.5
320	320	216.22	1.67	1.93	0.75	0.115	36.10	3.21E-14	150.4
900	900	205.09	3.30	0.72	0.88	2.578	17.03	3.04E-15	9.6
800	800	172.19	0.27	10.54	0.73	0.336	271.47	1.46E-15	150.1
420	420	17.19	1.45	5.05	0.82	0.446	121.61	2.46E-15	100.4
450	450	13.43	1.63	3.90	0.84	1.973	23.48	2.88E-15	78.0
440	360	19.30	7.48	3.38	0.85	16.042	17.81	4.67E-16	21.7
450	450	14.38	2.44	4.01	0.83	0.887	66.43	2.26E-15	51.9
440	310	18.26	2.79	3.49	0.85	0.960	77.49	1.79E-15	67.5
420	420	8.64	2.33	4.22	0.82	1.461	127.99	7.13E-16	62.5
305	305	18.06	4.19	3.74	0.81	2.580	16.19	3.19E-15	66.0
440	440	19.00	0.77	4.96	0.78	0.830	150.61	1.07E-15	173.1
500	500	16.06	2.20	4.83	0.78	4.644	29.06	9.88E-16	46.6
540	380	6.65	3.19	2.13	0.92	1.354	159.00	6.19E-16	39.3
490	320	4.59	2.65	3.91	0.91	1.312	27.28	3.73E-15	61.7

Figure 4.12: Fitted equivalent circuit parameters.

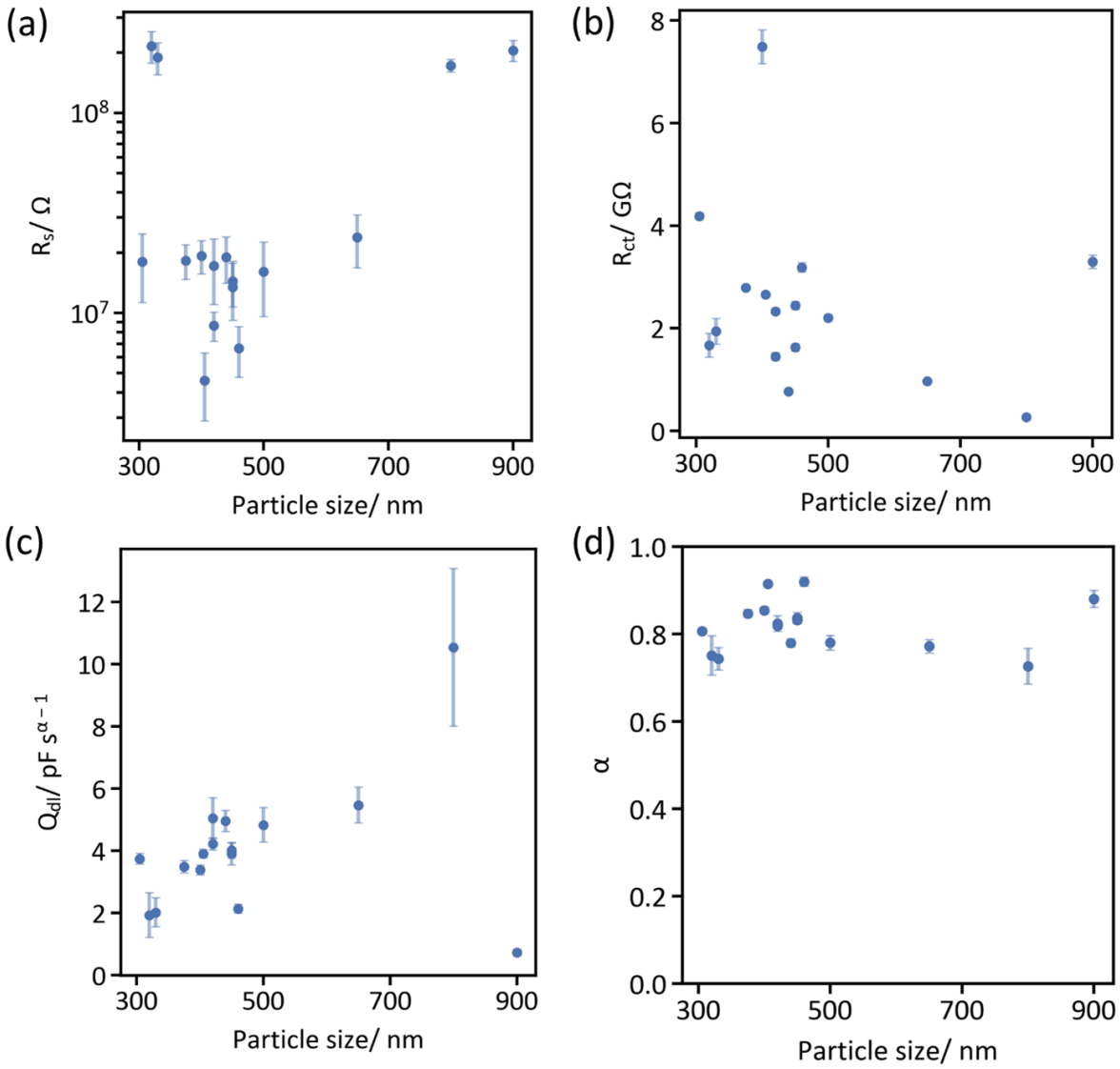

Figure 4.13: Equivalent circuit parameters plotted as a function of particle size. If a particle deviated from the cubic morphology, "particle size" refers to the average side length measured by SEM. (a) solution resistance, (b) charge-transfer resistance, (c) magnitude of double-layer capacitance constant phase element, and (d) CPE α parameter.

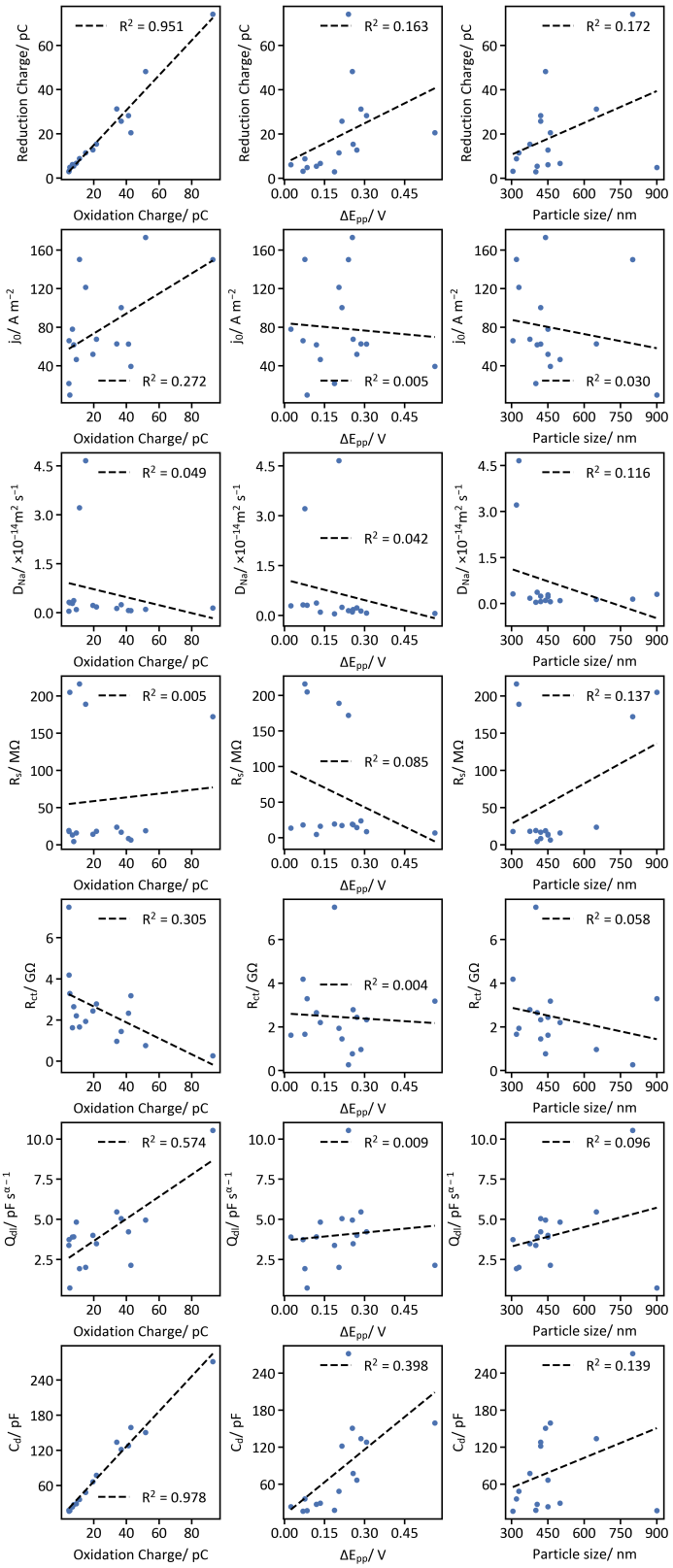
Reduction Charge/ pC
Oxidation Charge/ pC
ΔEpp/ V
Particle size/ nm
R² = 0.951
R² = 0.163
R² = 0.172
j0/ A m⁻²
R² = 0.272
R² = 0.005
R² = 0.030
DNa/ ×10⁻¹⁴m² s⁻¹
R² = 0.049
R² = 0.042
R² = 0.116
Rs/ MΩ
R² = 0.005
R² = 0.085
R² = 0.137
Rct/ GΩ
R² = 0.305
R² = 0.004
R² = 0.058
Qdl/ pF s^α−1
R² = 0.574
R² = 0.009
R² = 0.096
Cd/ pF
R² = 0.978
R² = 0.398
R² = 0.139

Figure 4.14: Correlation coefficients between various parameters extracted from single particle voltammograms, impedance spectra, and SEM. Oxidation charge: integrated charge from oxidative peak in CV. Reduction charge: integrated charge from reductive peak in CV. ΔE_{pp}: peak-to-peak separation extracted from CV. Particle size: particle side length measured by SEM. j_0: exchange current density. D_{Na}: sodium ion diffusion coefficient. R_s: solution resistance fitted from EIS. R_{ct}: charge transfer resistance fitted from EIS. Q_{dl}: magnitude of double layer capacitor element fitted from EIS. C_d: limiting low-frequency intercalation capacitance extracted from EIS diffusion model.
Most of these parameters (including those combinations not shown here) are not correlated to one another; here we discuss those that do show weak or strong correlations. The oxidation and reduction charge integrated from cyclic voltammograms are strongly related ($R^2 = 0.951$) to one another, as expected. Furthermore, they are strongly correlated ($R^2 = 0.978$) to the limiting, zero-frequency intercalation capacitance (C_d) extracted from the EIS diffusion model because both parameters are measures of the total (accessible) capacity of the particle. Interestingly, large Cd is also associated with larger peak-to-peak separations (ΔE_{pp}) in CV ($R^2 = 0.398$). This may be related to iR drop within the particle, as larger currents (larger charges and larger capacities) will cause larger iR drops and thus higher peak-to-peak separations.

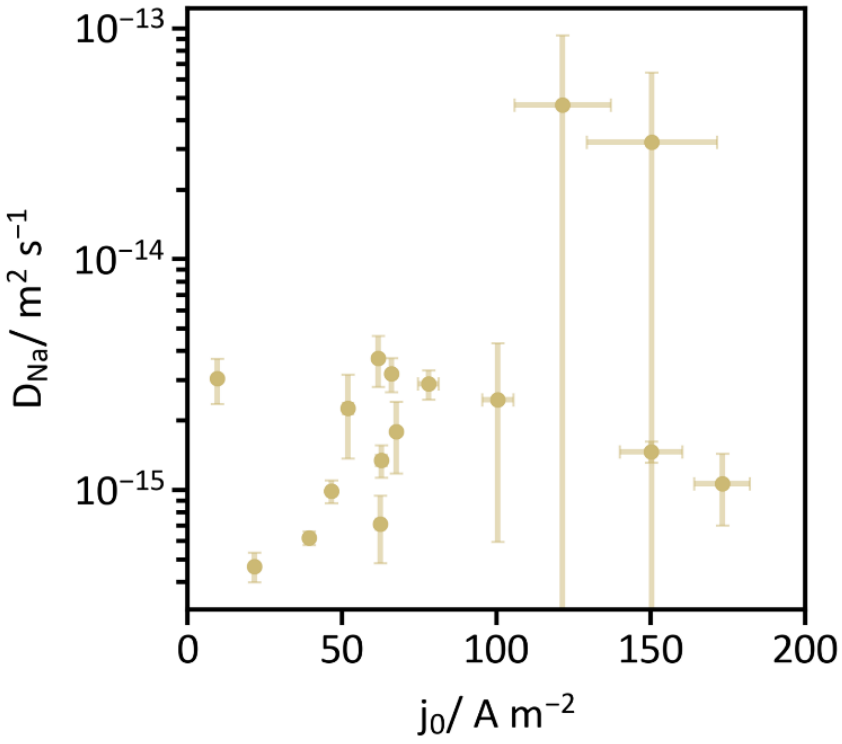

Figure 4.15: Relationship between D_{Na} and j_0 for the 16 particles studied herein. The two parameters are not correlated to one another.

References

[1] M. Kang, C. L. Bentley, J. T. Mefford, W. C. Chueh, P. R. Unwin, *ACS Nano* **2023**, *17*, 21493–21505.

[2] P. Saha, M. M. Rahman, C. M. Hill, *Journal of Physical Chemistry C* **2023**, *127*, 9059–9066.

[3] L. A. Baker, *Journal of the American Chemical Society* **2018**, *140*, 15549–15559.

[4] S. Goines, J. E. Dick, *Journal of The Electrochemical Society* **2020**, *167*, 037505.

[5] W. Xu, Y. G. Zhou, *Current Opinion in Electrochemistry* **2023**, *38*, 101221.

[6] T. Sun, Y. Yu, B. J. Zacher, M. V. Mirkin, *Angewandte Chemie International Edition* **2014**, *53*, 14120–14123.

[7] X. Xu, D. Valavanis, P. Ciocci, S. Confederat, F. Marcuccio, J.-F. Lemineur, P. Actis, F. Kanoufi, P. R. Unwin, *Analytical Chemistry* **2023**, *95*, 319–356.

[8] O. J. Wahab, M. Kang, P. R. Unwin, *Current Opinion in Electrochemistry* **2020**, *22*, 120–128.

[9] C. L. Bentley, *Electrochemical Science Advances* **2022**, *2*, 1–18.

[10] Y. Takahashi, Y. Kobayashi, Z. Wang, Y. Ito, M. Ota, H. Ida, A. Kumatani, K. Miyazawa, T. Fujita, H. Shiku, Y. E. Korchev, Y. Miyata, T. Fukuma, M. Chen, T. Matsue, *Angewandte Chemie International Edition* **2020**, *59*, 3601–3608.

[11] S. Varhade, E. B. Tetteh, S. Saddeler, S. Schumacher, H. B. Aiyappa, G. Bendt, S. Schulz, C. Andronescu, W. Schuhmann, *Chemistry – A European Journal* **2023**, *29*, e202203474.

[12] K. L. Anderson, M. A. Edwards, *Analytical Chemistry* **2023**, *95*, 8258–8266.

[13] C. Batchelor-McAuley, J. Ellison, K. Tschulik, P. L. Hurst, R. Boldt, R. G. Compton, *Analyst* **2015**, *140*, 5048–5054.

[14] J. Yao, K. D. Gillis, *Analyst* **2012**, *137*, 2674–2681.

[15] N. Ebejer, M. Schnippering, A. W. Colburn, M. A. Edwards, P. R. Unwin, *Analytical Chemistry* **2010**, *82*, 9141–9145.

[16] T. Tarnev, H. B. Aiyappa, A. Botz, T. Erichsen, A. Ernst, C. Andronescu, W. Schuhmann, *Angewandte Chemie - International Edition* **2019**, *58*, 14265–14269.

[17] X. Lu, M. Li, Y. Peng, X. Xi, M. Li, Q. Chen, A. Dong, *Journal of the American Chemical Society* **2021**, *143*, 16925–16929.

[18] M. Li, K.-h. Ye, W. Qiu, Y. Wang, H. Ren, **2022**, DOI 10.1021/jacs.2c00506.

[19] M. B. Cabré, D. Spurling, P. Martinuz, M. Longhi, C. Schröder, H. Nolan, V. Nicolosi, P. E. Colavita, K. McKelvey, *Nature Communications* **2023**, *14*, 1–7.

[20] C. Gao, Y. Li, J. Zhao, W. Sun, S. Guang, Q. Chen, **2023**, DOI 10.1021/acs.analchem.3c00255.

[21] B. Tao, I. J. McPherson, E. Daviddi, C. L. Bentley, P. R. Unwin, *ACS Sustainable Chemistry and Engineering* **2023**, *11*, 1459–1471.

[22] E. B. Tetteh, D. Valavanis, E. Daviddi, X. Xu, C. S. Santos, E. Ventosa, D. Martín-Yerga, W. Schuhmann, P. R. Unwin, *Angewandte Chemie - International Edition* **2023**, *62*, DOI 10.1002/anie.202214493.

[23] B. Tao, L. C. Yule, E. Daviddi, C. L. Bentley, P. R. Unwin, *Angewandte Chemie - International Edition* **2019**, *58*, 4606–4611.

[24] C. L. Bentley, M. Kang, F. M. Maddar, F. Li, M. Walker, J. Zhang, P. R. Unwin, *Chemical Science* **2017**, *8*, 6583–6593.

[25] I. M. Ornelas, P. R. Unwin, C. L. Bentley, *Analytical Chemistry* **2019**, *91*, 14854–14859.

[26] H. E. M. Hussein, G. Wood, D. Houghton, M. Walker, Y. Han, P. Zhao, R. Beanland, J. V. Macpherson, *ACS Measurement Science Au* **2022**, *2*, 439–448.

[27] B. D. B. Aaronson, C. H. Chen, H. Li, M. T. M. Koper, S. C. S. Lai, P. R. Unwin, *Journal of the American Chemical Society* **2013**, *135*, 3873–3880.

[28] X. Xu, D. Martín-Yerga, N. E. Grant, G. West, S. L. Pain, M. Kang, M. Walker, J. D. Murphy, P. R. Unwin, *Small* **2023**, *19*, 1–10.

[29] A. C. Lazanas, M. I. Prodromidis, *ACS Measurement Science Au* **2023**, *3*, 162–193.

[30] A. Lasia, *Electrochemical Impedance Spectroscopy and its Applications*, Springer New York, **2014**.

[31] J. R. Macdonald, W. B. Johnson in *Impedance Spectroscopy*, John Wiley & Sons, Ltd, **2018**, pp. 1–20.

[32] A. R. C. Bredar, A. L. Chown, A. R. Burton, B. H. Farnum, *ACS Applied Energy Materials* **2020**, *3*, 66–98.

[33] J. Frisch, *Miscellanea Berolinensia ad incrementum Scientiorum* **1710**, *1710*, 377–378.

[34] J. Peng, W. Zhang, Q. Liu, J. Wang, S. Chou, H. Liu, S. Dou, *Advanced Materials* **2022**, *34*, 2108384.

[35] M. Pasta, C. D. Wessells, R. A. Huggins, Y. Cui, *Nature Communications* **2012**, *3*, 1149.

[36] K. Hurlbutt, S. Wheeler, I. Capone, M. Pasta, *Joule* **2018**, *2*, 1950–1960.

[37] A. I. Komayko, N. A. Arkharova, D. E. Presnov, E. E. Levin, V. A. Nikitina, *Journal of Physical Chemistry Letters* **2022**, *13*, 3165–3172.

[38] G. S. Popkirov, R. N. Schindler, *Review of Scientific Instruments* **1992**, *63*, 5366–5372.

[39] Y. You, X.-L. Wu, Y.-X. Yin, Y.-G. Guo, *Energy Environ. Sci.* **2014**, *7*, 1643–1647.

[40] C. L. Bentley, M. Kang, P. R. Unwin, *Current Opinion in Electrochemistry* **2017**, *6*, 23–30.

[41] C. A. Lundgren, R. W. Murray, *Inorganic Chemistry* **1988**, *27*, 933–939.

[42] A. J. Bard, L. R. Faulkner, *Electrochemical Methods: Fundamentals and Applications*, 2nd ed., John Wiley & Sons, **2001**.

[43] R. G. Compton, C. E. Banks, *Understanding Voltammetry*, 3rd, World Scientific, **2018**.

[44] G. S. Popkirov, R. N. Schindler, *Review of Scientific Instruments* **1993**, *64*, 3111–3115.

[45] B. Roehrich, E. Z. Liu, R. Silverstein, L. Sepunaru, *The Journal of Physical Chemistry Letters* **2021**, *12*, 9748–9753.

[46] J. J. García-Jareño, J. J. Navarro, A. F. Roig, H. Scholl, F. Vicente, *Electrochimica Acta* **1995**, *40*, 1113–1119.

[47] J. P. Meyers, M. Doyle, R. M. Darling, J. Newman, *Journal of The Electrochemical Society* **2000**, *147*, 2930.

[48] E. Barsoukov, J. H. Kim, J. H. Kim, C. O. Yoon, H. Lee, *Solid State Ionics* **1999**, *116*, 249–261.

[49] V. Miß, A. Ramanayagam, B. Roling, *ACS Applied Materials & Interfaces* **2022**, *14*, 38246–38254.

[50] M. D. Levi, D. Aurbach, *Journal of Physical Chemistry B* **2004**, *108*, 11693–11703.

[51] M. Janssen, J. Bisquert, *The Journal of Physical Chemistry C* **2021**, *125*, 15737–15741.

[52] B. Niu, W. Jiang, B. Jiang, M. Lv, S. Wang, W. Wang, *Nature Communications* **2022**, *13*, DOI 10.1038/s41467-022-30058-4.

[53] J. Min, L. M. Gubow, R. J. Hargrave, J. B. Siegel, Y. Li, *Energy and Environmental Science* **2023**, *16*, 3847–3859.

[54] W. Wei, T. Yuan, W. Jiang, J. Gao, H.-y. Chen, W. Wang, **2020**, DOI 10.1021/jacs.0c06171.

[55] T. Liu, M. Li, Y. Wang, Y. Fang, W. Wang, *Chemical Science* **2018**, *9*, 4424–4429.

[56] R. C. Evans, Z. N. Nilsson, J. B. Sambur, *Analytical Chemistry* **2019**, *91*, 14983–14991.

[57] Y. Takahashi, T. Yamashita, D. Takamatsu, A. Kumatani, T. Fukuma, *Chemical Communications* **2020**, *56*, 9324–9327.

[58] X. Li, N. Li, K.-L. Zhang, J. Huang, S. Jiao, H.-S. Chen, W.-L. Song, *Angewandte Chemie International Edition* **2022**, *100083*, DOI 10.1002/anie.202205394.

[59] P. Saha, J. W. Hill, J. D. Walmsley, C. M. Hill, *Analytical Chemistry* **2018**, *90*, 12832–12839.

Chapter 5

Interrogation of Electrochemical Aptamer Based Sensors using Impedance Spectroscopy

Adapted with permission from: Roehrich, B.; Leung, K. K.; Gerson, J.; Kippin, T. E.; Plaxco, K. W.; Sepunaru, L. Calibration-Free, Seconds-Resolved In Vivo Molecular Measurements Using Fourier-Transform Impedance Spectroscopy Interrogation of Electrochemical Aptamer Sensors. *ACS Sensors* **2023**, 8 (8), 3051–3059. https://doi.org/10.1021/acssensors.3c00632.

5.1 Introduction

The availability of sensors able to measure the concentrations of specific molecules in the body in real time would revolutionize the monitoring of health and the diagnosis and treatment of disease. By providing a real-time window into plasma drug concentrations, for example, such an advance would significantly improve the individualization of pharmacological treatments.[1] Motivated by this promise, we and others have been developing electrochemical aptamer-based (EAB) sensors.[2–7] EAB sensors are comprised of a gold electrode on which a sub-monolayer of target-recognizing, redox reporter-modified, nucleic acid aptamers are deposited via thiol-on-gold self-assembled monolayer formation.[6] Introduction of the specific target molecule triggers a conformational change in this aptamer, altering the distance between the redox reporter and the electrode surface, changing, in turn, the rate of electron transfer (k_{et}) from the attached redox reporter (Figure 5.1). This change in k_{et}, which, to date, has been monitored using a range of electrochemical approaches, thus reports on the target concentration in real-time without the addition of exogenous reagents. Of note, this signal transduction mechanism does not rely on the chemical transformation of the target, rendering the approach general. Consistent with this, EAB sensors have been shown to support the high-frequency, real-time measurement of multiple drugs,[7–10] metabolites,[11, 12] and protein biomarkers,[3, 13, 14] both in vitro and in vivo.

A variety of electrochemical interrogation methods, including cyclic voltammetry (CV),[15] chronoamperometry,[16] AC voltammetry,[3, 4, 17] square wave voltammetry

(SWV)[7, 18] and intermittent pulse amperometry[19] have been employed in the interrogation of EAB sensors. While each of these has advantages and disadvantages,[20] SWV has seen the most widespread use in vivo. This is because, measuring sequential square wave voltammograms at two different frequencies enables drift correction in an approach called kinetic differential measurements (KDM).[21] Using KDM, which employs the difference between SWV measurements taken at two frequencies to subtractively remove drift, we have achieved multi-hour measurements of multiple target molecules in situ in the veins of living animals.[7, 8, 22] The resulting need to collect two square wave voltammograms per measurement point, however, reduces the time resolution of such measurements to, typically, 6 to 22 s.[6, 7, 9, 11, 22] And because it relies on the monitoring of peak currents, SWV-based interrogation is also susceptible to sensor-to-sensor fabrication variation arising from differences in the number of methylene blue modified aptamers placed on each. Because of this, sensors employing SWV must be individually calibrated before use.

Here we demonstrate electrochemical impedance spectroscopy (EIS) as an alternate EAB sensor interrogation method, one that does not require calibration and achieves superior time resolution. EIS is widely used in biosensing due to the depth of information it provides on the electrode-electrolyte interface.[23–26] In this approach, the impedance between the working electrode and the counter electrode is measured as a function of frequency. At higher frequencies, this impedance informs on rapid processes, such as the formation of the electrochemical double layer. Impedances measured at lower

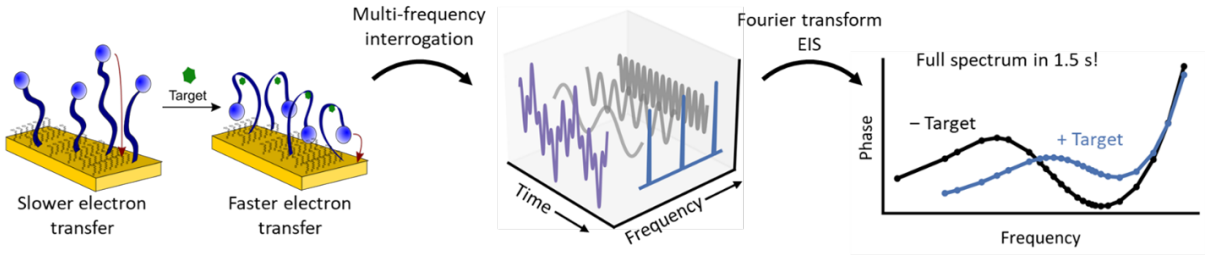

Figure 5.1: (left) EAB sensors rely on the target-induced conformational change of a DNA aptamer to produce a change in electron transfer kinetics. Upon target binding, the redox label is brought closer to the electrode, increasing the electron transfer rate constant. (middle) The resulting change in electron transfer rate can be rapidly measured using fast Fourier transform electrochemical impedance spectroscopy (FFT-EIS). In this, sinusoidal oscillations of several different frequencies are summed and the resultant waveform is applied as an AC voltage perturbation to the working electrode of the EAB sensor. (right) Fourier transform of the applied, multi-frequency, voltage and the current response yields a full impedance spectrum rapidly enough to support real-time sensor interrogation with time resolution limited (here to less than 2 s) by the lowest frequency sinusoidal perturbation employed.

frequencies, in contrast, are typically associated with slower processes, such as electron transfer, adsorption and intercalation events, as well as mass transport.[27–29] Despite the broad insights EIS can provide, its adaptation to the interrogation of EAB sensors has had relatively little investigation.[30, 31] For example, in the broadest study to date, impedimetric phase shift at a single frequency (rather than the collection of an entire impedance spectrum) was used to monitor changing target concentrations in real-time.[31] But while such phase monitoring achieves exceptional, 300 ms, time resolution, this single-frequency approach required the calibration of individual sensors and was not demonstrated to work in vivo. Here we have taken a different approach to employ EIS in the interrogation of EAB sensors. Specifically, we have used fast Fourier transform electrochemical impedance spectroscopy (FFT-EIS) to simultaneously measure

the impedance of in vivo EAB sensors at multiple frequencies, yielding both rapid time resolution and the depth of information contained in a full impedance spectrum.[32–35] With this, we can estimate k_{et} – and from that, the target concentration – every few seconds (here less than 2 s), providing a method of in-vivo sensor interrogation that is both more-highly-time-resolved and calibration-free.

5.2 Impedimetric Characterization of EAB Sensors In Vitro

In EIS, a sinusoidal oscillating voltage on top of a set DC bias is applied to the working electrode and the (sinusoidal) current response is recorded.[29] The impedance, Z, at a particular frequency ω is defined as the ratio between voltage and current at that frequency (Equation 5.1),[24] with the "lag" between the voltage perturbation and the current response quantified as the phase shift ϕ.

$$Z(\omega) = \frac{|V| \sin \omega t}{|I| \sin \omega t + \phi} = |Z| e^{i\phi} \tag{5.1}$$

Here, |V| and |I| are the amplitudes of the voltage and current, respectively, ω is the frequency, i is the square root of -1, and |Z| is the magnitude of the impedance. The primary benefit of EIS (and its label of "spectroscopy") arises from the measurement of Z across a wide range of frequencies (e.g., millihertz to kilohertz). Specifically, frequency-dependent impedance measurements can be used to characterize processes ranging from

the rapid charging of the electric double layer at high frequencies to electron transfer reactions and molecular diffusion occurring on much longer time scales.[27, 36]

In applications such as ours –the real-time measurement of specific molecules in the living body– a limitation of EIS is that its time resolution is typically rather poor. Specifically, with traditional, "frequency-sweep" EIS, each frequency, f, interrogated requires at least 1/f measurement time. Given this, the measurement of spectra down to frequencies of order 1 Hz requires total acquisition times of at least ten seconds. FFT-EIS, however, retains the information contained in the entire frequency range while significantly decreasing this acquisition time. It does so by measuring the impedance at all frequencies simultaneously.[32, 34, 35, 37] In our implementation of FFT-EIS, the applied voltage perturbation is a superposition of 18 sine waves spanning the desired frequency range. Due to the (approximate) linearity of electrochemical systems over small voltage changes,[27] the resulting current response is a superposition of the current response at each applied frequency. A Fourier transform of the recorded voltage and current data thus yields an impedance spectrum.[33, 35] Using this approach, we can collect a complete impedance spectrum in the time scale defined by the slowest applied frequency ($t_{spectrum} \geq 1/f_{min}$). For example, an impedance spectrum spanning 18 frequencies from 1 Hz to 1 kHz, which would require 23 s to collect on our potentiostat (Autolab PGStat128N) using traditional EIS, can be measured in 1.8 s using our FFT-EIS implementation.

The impedimetric properties of EAB sensors, which are sensitive to target concentration, can be rapidly measured using FFT-EIS to enable highly time-resolved molecular

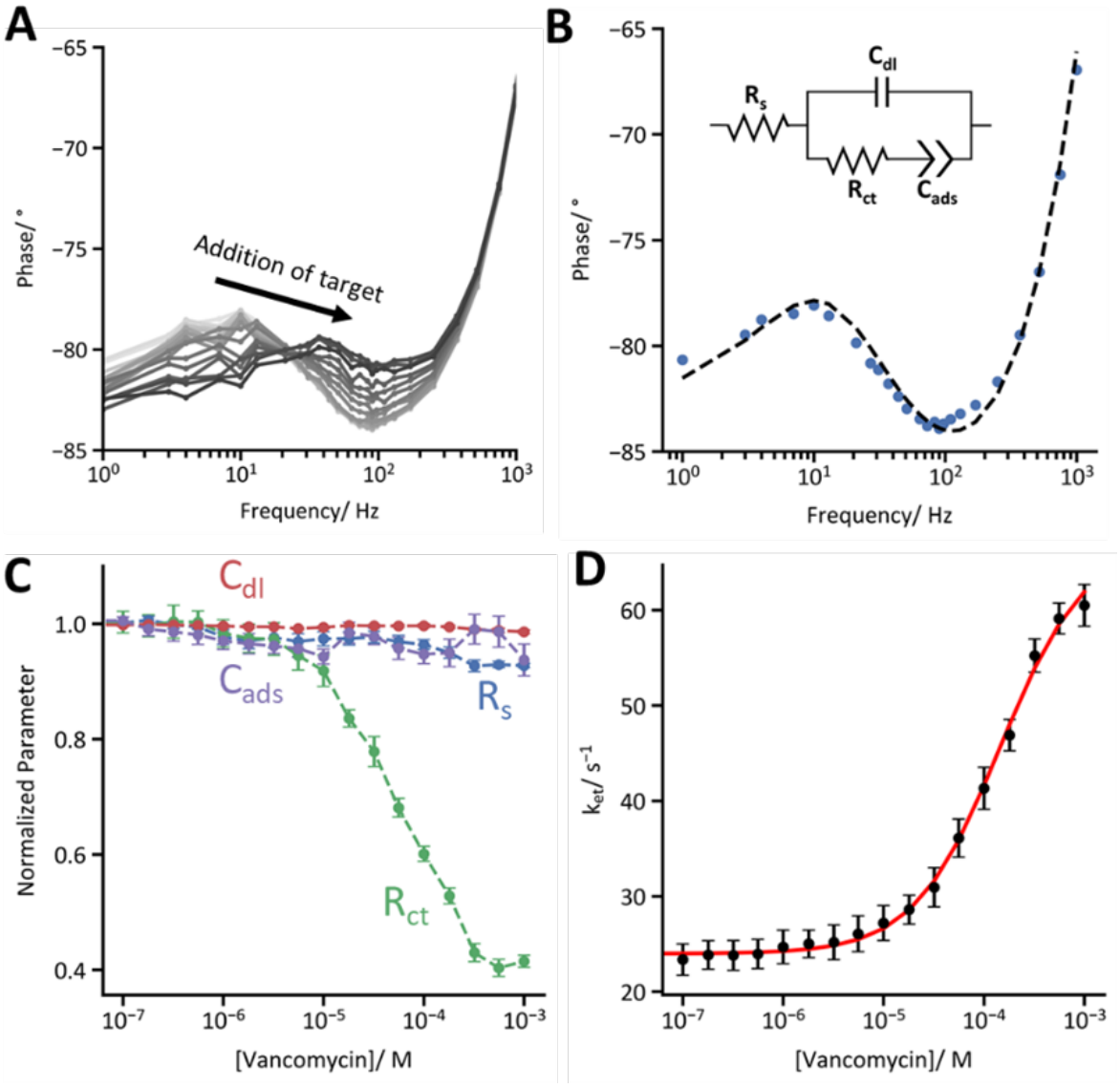
A
Phase/ °
Addition of target
Frequency/ Hz
B
Phase/ °
C_{dl}
R_s
R_{ct}
C_{ads}
Frequency/ Hz
C
Normalized Parameter
C_{dl}
C_{ads}
R_s
R_{ct}
[Vancomycin]/ M
D
k_{et}/ s^{-1}
[Vancomycin]/ M

Figure 5.2: When used to interrogate an EAB sensor, FFT-EIS is able to rapidly correlate electrochemical impedance to the concentration of a target molecule. (A) Here, a vancomycin-detecting EAB sensor was immersed in whole bovine blood at 37 °C and exposed to increasing quantities of its target. This induced a conformational change in the aptamer which caused a shift in the impedance spectrum, as resolved by FFT-EIS. (B) To analyze such FFT-EIS data we employ equivalent circuit modelling, using a circuit model comprised of resistors representing the bulk solution resistance (R_s) and the Faradaic electron transfer between the electrode and the methylene blue moieties (R_{ct}), as well as capacitors representing the electrochemical double layer (C_{dl}) and the pseudocapacitance between the electrode surface and the surface-bound methylene blue (C_{ads}).[38] We used the transfer function of this circuit to fit our experimentally measured data. The data presented here were collected from a vancomycin-detecting sensor immersed in whole bovine blood at 37°C in the absence of vancomycin. (C) Challenging the EAB sensor with increasing concentrations of its vancomycin target reveals that increasing target concentration predominantly impacts (here, decreases) R_{ct} (in this figure, the error bars represent standard deviations across four independently fabricated and interrogated sensors). (D) The electron transfer rate k_{et} can be approximated from R_{ct} and C_{ads} using Equation 5.4. The resulting binding curve fits a Hill-Langmuir isotherm with a dissociation constant $K_D = 144 \pm 31$ μM (the latter reflects estimated 95% confidence intervals).

measurements.[8, 39, 40] To demonstrate this, we used a previously-reported aptamer to fabricate an EAB sensor targeting the antibiotic vancomycin.[8] We then applied the half-wave potential ($E_{1/2}$) of the sensor's methylene blue redox reporter as the DC bias (prior to each experiment, we determine $E_{1/2}$, which is typically around -0.285 V versus Ag/AgCl, using cyclic voltammetry; Figure 5.6). We then used FFT-EIS to record impedance spectra as the sensor was immersed in whole bovine blood at 37 °C. When the spectrum obtained in the absence of target molecule is displayed as a Bode plot (phase versus frequency;[29] Figure 5.2A, black trace), a local maximum is observed around 10 Hz, reflecting the electron transfer rate between the methylene blue and the electrode surface.[31] As expected (given that the rate of electron transfer between the methylene blue and the electrode increases upon target binding),[31] this peak steadily shifts to

higher frequencies when the sensor is exposed to increasing vancomycin concentrations. To determine the origin of this concentration-dependent shift, we applied equivalent circuit modelling[23, 24] using a simple, four-element equivalent circuit that has previously been used to represent the surface-tethered redox species seen in EAB sensors (Figure 5.2B).[31, 38, 41] This circuit consists of a resistor, modeling bulk solution resistance (R_s), that is in series with the three other components: a capacitor, representing interfacial double-layer capacitance (C_{dl}), in parallel with a resistor, representing the Faradaic charge transfer resistance (R_{ct}), and a capacitor (C_{ads}), representing the surface-attached methylene blues. To better account for the rough, non-ideal surface of the EAB sensor, the latter is modeled as a constant phase element, rather than a true capacitor.[42] This model fits our FFT-EIS data quite well ($\chi^2 \approx 0.015$, Figure 5.2B), suggesting that this four-component circuit is an adequate description of the physics of our sensors.

The components of the equivalent circuit behave as expected in response to increasing vancomycin concentrations. R_s, C_{dl}, and C_{ads}, for example, are effectively independent of vancomycin concentration. R_{ct}, in contrast, decreases with increasing vancomycin concentration (Figure 5.2C). This presumably arises due to the increased rate of electron transfer between the electrode and the bound, folded aptamer, as R_{ct} is inversely proportional to k_{et}:[38]

$$R_{ct} = \frac{2RT}{F^2 A \Gamma k_{et}} \tag{5.2}$$

Here, R is the gas constant, T is temperature, F is Faraday's constant, A is the electrochemical surface area of the working electrode, and Γ is the surface coverage of the

redox-active molecule. Other than k_{et}, all of these variables are constant during a given experiment, and thus the decrease in R_{ct} is entirely attributed to an increase in k_{et}. Since, in turn C_{ads} is given by [38]

$$C_{ads} = \frac{F^2 A \Gamma}{4RT} \tag{5.3}$$

k_{et} can be calculated from the R_{ct} and C_{ads} as [38]

$$k_{et} = \frac{1}{2R_{ct}C_{ads}} \tag{5.4}$$

Given that the rate of electron transfer from the methylene blue depends on whether the aptamer is target bound, k_{et} should trace a Langmuir-Hill isotherm when plotted versus vancomycin concentration. As expected, it does (Figure 5.2D). The resulting monotonic relationship can be used to convert k_{et} into estimates of vancomycin concentration in a manner that is calibration-free. Specifically, k_{et} is independent of the number of surface-bound methylene blue species. It thus is independent of important sensor-to-sensor sources of fabrication variability, such as changes in the surface area of the electrode (Figure 5.7), or the aptamer packing density, which would change the number of methylene blues and thus the absolute Faradaic current. Because of this, a k_{et} versus vancomycin concentration calibration curve measured for a single sensor can be applied to all other sensors utilizing the same aptamer, obviating the need to calibrate each individual sensor.

5.3 Quantification of Plasma Vancomycin in Living Rats

FFT-EIS interrogation of EAB sensors supports the rapid measurement of specific molecules in the living body. To demonstrate this, we bundled aptamer-modified gold wire working electrodes with platinum counter and silver-silver chloride reference electrodes in a 20-gauge catheter (Figure 5.3A), and surgically inserted the resulting three-electrode sensor into the right jugular vein of an anesthetized rat.[43] We then measured full impedance spectra (containing 18 frequencies between 1 Hz and 1 kHz; Figure 5.8) every 1.8 s for 2.5 hr. Of note, the magnitude of the impedance increases over time in vivo (Figure 5.3B). This contrasts with the relatively unchanging impedance we observed in whole blood in vitro (Figure 5.9), suggesting that the mechanisms by which EAB sensors degrade may differ between the two conditions. Fitting the time-resolved spectra indicates that this change in impedance is associated with a steady increase in R_{ct} and a corresponding decrease in C_{ads} (Figure 5.3C). This presumably occurs due to the non-specific adsorption of proteins and cells to the electrode and/or aptamer loss (although reductive stripping of aptamers should be minimized by the narrow potential window in EIS),[44] which we expect will increase R_{ct} and decrease C_{ads} by reducing the number of methylene blue reporters that can access the electrode surface. In contrast, k_{et} does not drift (Figure 5.3D), indicating that whatever causes impedance to drift does not affect the electron transfer kinetics of the aptamers that remain electrochemically accessible.

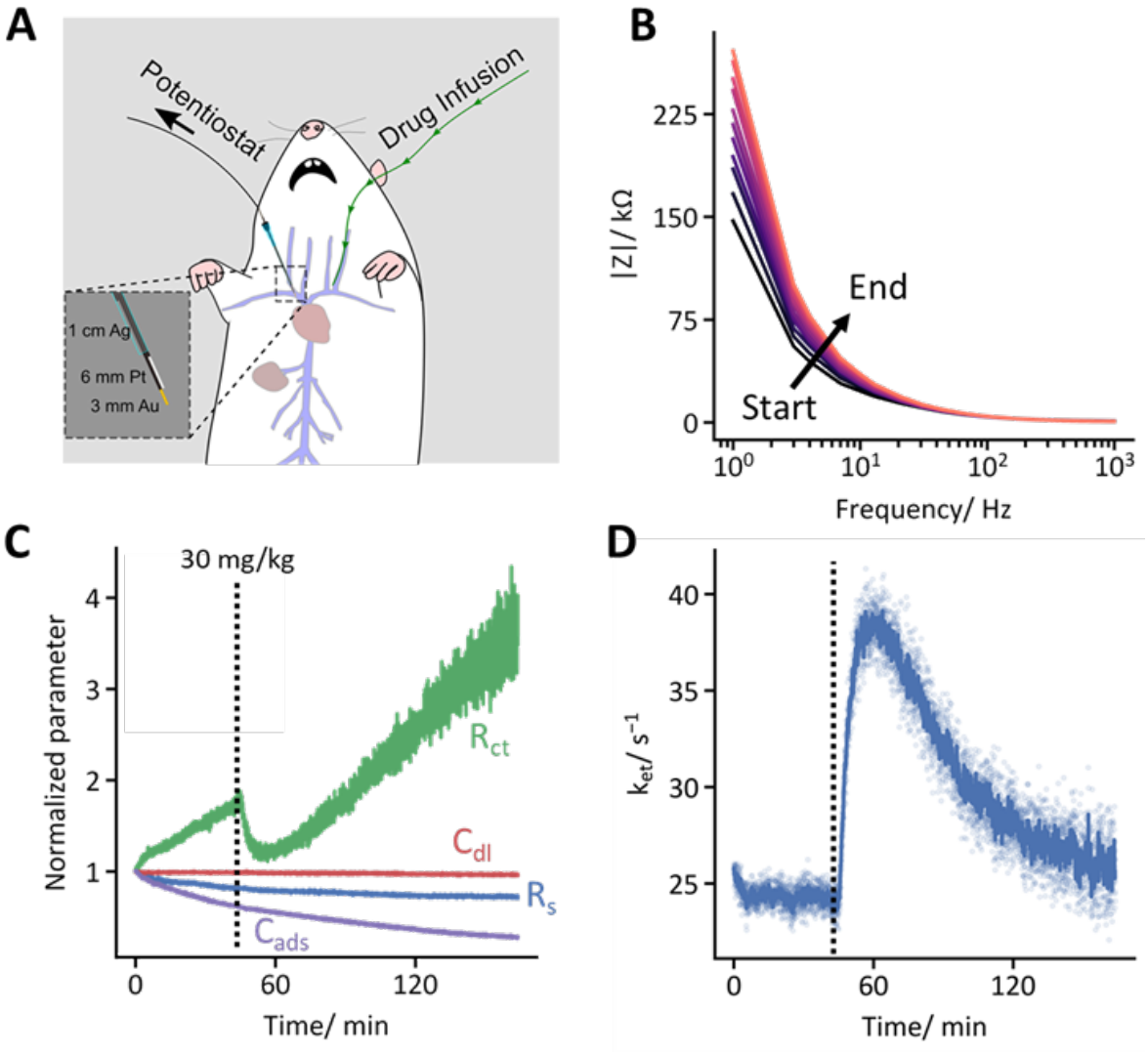
A
Potentiostat
Drug Infusion
1 cm Ag
6 mm Pt
3 mm Au
B
|Z| / kΩ
225
150
75
0
End
Start
10^0
10^1
10^2
10^3
Frequency/ Hz
C
30 mg/kg
Normalized parameter
4
3
2
1
R_{ct}
C_{dl}
R_s
C_{ads}
0
60
120
Time/ min
D
k_{et}/ s^{-1}
40
35
30
25
0
60
120
Time/ min

Figure 5.3: FFT-EIS supports high-frequency, real-time measurements in the living body. (A) In vivo EAB sensors are comprised of an aptamer-functionalized gold working electrode, a platinum counter electrode, and an Ag/AgCl reference electrode, each bound in heat-shrink tubing and inserted via a catheter into the right jugular vein of an anesthetized rat. (B) Using FFT-EIS, we measured impedance spectra every 1.8 s by applying the formal potential of methylene blue as the DC bias and the necessary multi-sine waveform as an AC perturbation. The magnitude of the impedance, |Z|, increased over the duration of the experiment, particularly at low frequencies. Presumably, this is due to fouling caused by nonspecific adsorption of proteins, cells, or small molecules to the sensor surface. (C) Fitting the spectra reveals that this drift is correlated with an immediate, steady increase in R_{ct} and a corresponding decrease in C_{ads}. Upon injection of 30 mg/kg vancomycin, however, only R_{ct} is responsive. (D) Calculation of k_{et} reveals that this parameter is stable prior to drug infusion, indicating the intrinsic electron transfer rate constant of the unbound state of the aptamer is unaffected by whatever is causing R_{ct} and C_{ads} to drift. Upon drug infusion, however, k_{et} rises suddenly, indicating a larger population of the target-bound state of the aptamer. After the infusion is concluded, k_{et} falls as the drug is excreted by the kidneys and the unbound aptamer again dominates. Here, the raw data (light blue points) are smoothed using a 13-s rolling average (dark blue trace).

While this is perhaps surprising given the likelihood of electrode fouling occurring in vivo, this drift resistance agrees with the exceptional baseline stability (for $>$ 24 h in 37°C whole blood) previously reported for phase-interrogated EAB sensors in vitro.[31] Upon the infusion of 30 mg/kg vancomycin, however, k_{et} rapidly rises as the aptamer shifts to its target-bound conformation (Figure 5.3D). Following the end of the infusion, k_{et} returns to its baseline value as the drug is removed from the plasma via the kidneys. This said, the signal-to-noise ratio does fall at later stages of the experiment, presumably due to the loss of aptamers.

FFT-EIS interrogation of EAB sensors provides a highly-time-resolved window into molecular physiology and pharmacokinetics (Figure 5.4A). To demonstrate this, we placed sensors into the jugular veins of three rats. Prior to drug infusion, we measured

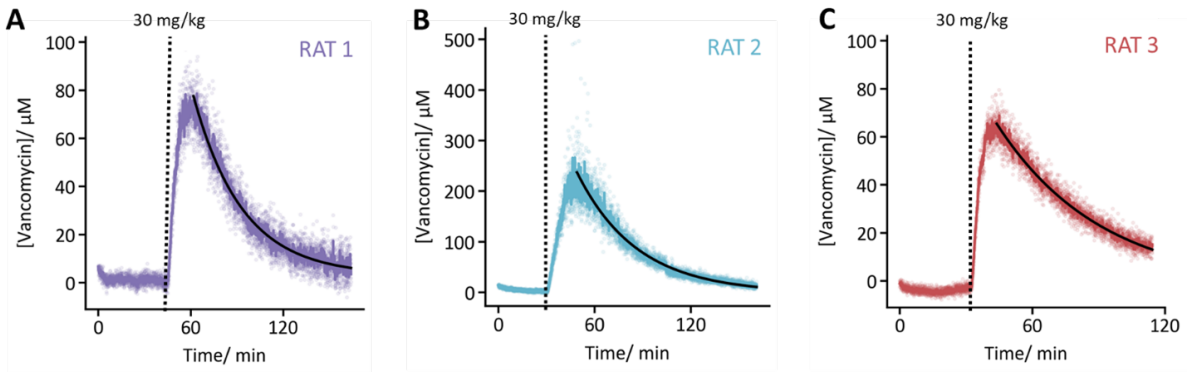

Figure 5.4: Using FFT-EIS to interrogate EAB sensors yields rapidly time-resolved molecular measurements in the living body. (A – C) Experiments in three separate animals confirm the absence of the drug pre-infusion, and show the expected concentration spike. Here, the raw data (light points; 1.8 s resolution) are smoothed using a seven-point (13 s) rolling average (darker trace). The antibiotic concentration decayed monoexponentially (fits shown as black traces) after each dosing, with time constants of (A) 33.1 ± 0.5 min, (B) 37.3 ± 0.7 min, and (C) 47.4 ± 1.3 min (95% confidence intervals). Of note, the initial k_{et} values of 25.1 ± 0.5 s^{-1}, 27.0 ± 0.5 s^{-1}, and 23.3 ± 0.4 s^{-1} are similar (errors reflect the standard deviation of the first one hundred data points) despite variable aptamer loadings (calculated from C_{ads} to be 1.08 ± 0.03 pmol, 0.61 ± 0.02 pmol, and 0.74 ± 0.02 pmol). Thus, k_{et} is relatively insensitive to small changes in aptamer packing.

vancomycin concentrations fluctuating tightly around zero (mean ± one standard deviation = 1.1 ± 1.7 μM). While this is a marginally higher noise than seen for the same in vivo sensor when interrogated using square wave voltammetry (± 1 μM),[43] the present EIS technique allows for seven-fold faster data acquisition – application of a seven point rolling average reduces our noise to just ±0.8 μM. Following infusion of the drug, its concentration is observed to rise to maxima of 70 to 250 μM before decreasing exponentially with a time constant of 32 to 47 min. The decay rates observed between three independent animals are similar to our previous observation and reflect

each animal's unique physiology,[8] highlighting the benefit of using EAB sensors to individualize clinical dosing.

5.4 Real Time Quantification of Plasma Phenylalanine

To demonstrate the general applicability of FFT-EIS as an EAB sensor interrogation technique, we next applied it to a sensor against the endogenous target phenylalanine (Figure 5.5). Specifically, after calibrating a phenylalanine-detecting EAB sensor[11] in vitro (details on the sensor calibration can be found in the Supporting Information, Figure 5.11), we used FFT-EIS interrogation to measure the molecule's concentration in the jugular veins of anesthetized rats. Doing so, we observed baseline phenylalanine concentrations of 41 $\pm$ 10 μM (the latter reflects one standard deviation) in a fasted animal and 39 $\pm$ 6 μM in a non-fasted animal, values in line with previous reports.[11, 45] Upon two intravenous infusions of additional phenylalanine, we observed rapid rises to peak concentrations of 300 to 400 μM followed by rapid decays back to baseline in the fasted animal. Fitting the decay transients to the previously-reported biexponential model of phenylalanine kinetics[11] yielded time constants of $\tau_1 = 0.2 \pm 0.1$ min and $\tau_2 = 3.8 \pm 0.2$ min for the first injection, and $\tau_1 = 1.7 \pm 0.1$ min and $\tau_2 = 20 \pm 2$ min for the second (ranges are 95% confidence intervals), suggesting that the animal's ability to rapidly store additional phenylalanine may have been saturated after the first challenge.

In a non-fasted animal, in contrast, we measured a higher peak concentration (around 600 μM) and a slower decay (τ_1 = 3.3 $\pm$ 0.1 min and τ_2 = 35 $\pm$ 7 min) to a higher, slowly decaying baseline following phenylalanine challenge,[11] discrepancies that align with previous, in vivo measurements of phenylalanine kinetics in fasted and non-fasted rats.[11]

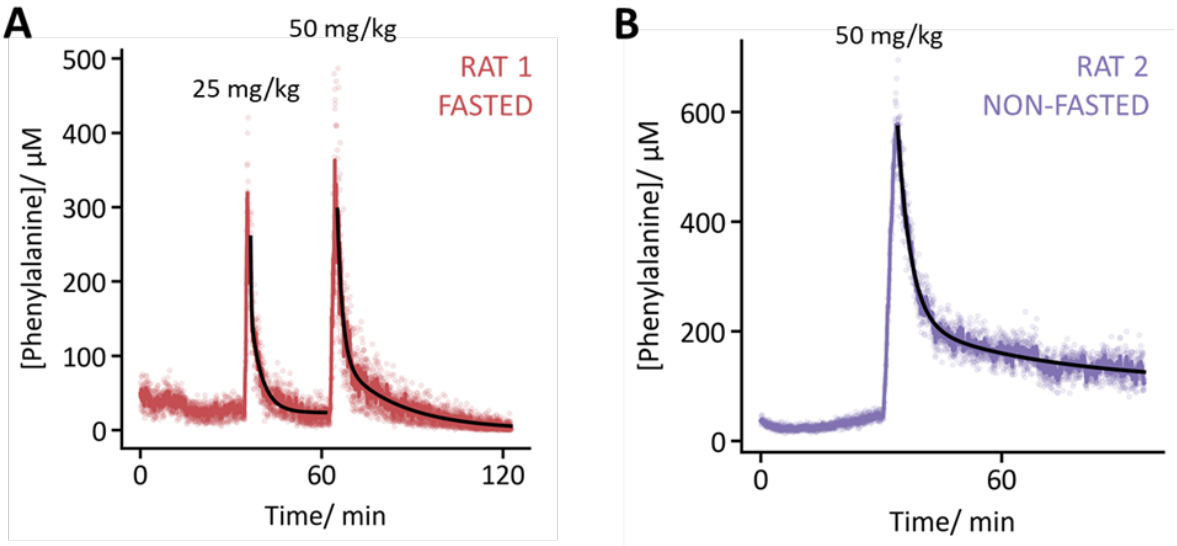

Figure 5.5: Using FFT-EIS to interrogate phenylalanine-detecting EAB sensors we have monitored this metabolite in situ in the jugulars of live rats with 1.8 s resolution. (A) A fasted animal was infused with two sequential doses of phenylalanine. In both cases, the concentration of free phenylalanine in the blood quickly decayed back to the pre-infusion baseline (41 $\pm$ 10 μM, 31 $\pm$ 9 μM, and 25 $\pm$ 10 μM before injection, after the first injection, and after the final injection, respectively). (B) In contrast, the return to the post-infusion baseline was slower in a non-fasted animal, which is consistent with previous reports regarding phenylalanine homeostasis.[11] Here, the raw data (light points) are smoothed using a 13-s rolling average (darker trace). Concentration decay transients were fit to a two compartment (i.e., biexponential) model (black traces).

5.5 Conclusions

Looking forward, we believe it may prove possible to improve EIS-interrogated EAB sensors still further. For example, using a thinner monolayer,[46] a shorter DNA strand,[47] or a more rapidly electron-transferring redox reporter would increase k_{et}, thus raising the lowest frequency that needs to be sampled and, with that, improving time resolution. Likewise, further studies should focus on longer duration experiments and experiments in awake animals which, while rendered difficult due to animal welfare concerns,[7] are necessary for improving sensor longevity and translating EAB technology to the clinic.

We have established FFT-EIS as a rapid, reliable, calibration-free method of interrogating EAB sensors, both in vitro and in vivo. Specifically, we have demonstrated the ability of FFT-EIS to measure the electron transfer rate associated with EAB sensors and used this to determine the concentration of their molecular targets with a time resolution of just 1.8 s. Because this approach uses k_{et} as a means of monitoring target concentration, rather than absolute current, it is independent of both sensor-to-sensor fabrication variation and the drift arising due to fouling in biological fluids, rendering the technique suitable for performing calibration-free in vivo measurements. In support of this, we used vancomycin- and phenylalanine-detecting EAB sensors to successfully monitor plasma concentrations of these targets in the veins of live animals, with time resolution of better than 2 s and without requiring the calibration of each, individual sensor.[11] When combined with the modularity of aptamers, the benefits associated with

impedimetric interrogation of EAB sensors could improve our understanding of pharmacokinetics and metabolism, and play an important role in the future of personalized medicine.

5.6 Supporting Information

5.6.1 Experimental

Materials. In-vitro sensors were made using 0.2 mm diameter gold wire (99.99%, Thermo Fisher) insulated with polyolefin heat-shrink tubing (0.05",0.017", 0.007", McMaster-Carr). For in-vitro tests, we used a commercial Ag/AgCl(s) reference electrode (and a commercial platinum reference electrode CH Instruments Inc). Intravenous sensors used for in-vivo measurements were made using 0.2 mm diameter gold wire, 0.005 in. diameter platinum wire (99.99% purity, A-M Systems) and 0.005 in. diameter silver wire (99.99% purity, A-M Systems). The insulation used for these sensors was polytetrafluoroethylene heat-shrink (HS Sub-Lite-Wall, 0.02, 0.005, 0.003±0.001 in, black, Zeus Inc.) Sodium hydroxide, 6-mercapto-1-hexanol, Tris (2-carboxyethyl) phosphine, sulfuric acid, phenylalanine, and the phenylalanine assay kit were obtained from Sigma Aldrich. Phosphate buffered saline (PBS) was diluted from a 20x stock purchased from Santa Cruz Biotechnologies. Vancomycin-HCl was purchased from VWR. Methylene blue- and $HO-C_6S-S-C_6-$modified DNA sequences were purchased from Integrated DNA Technologies (Coralville, Iowa); their sequences are listed in Table

Name	Sequence and modifications
Vancomycin	$HS - C_6 - CGAGGGTACCGCAATAGTACTTATTGTTCGCCTATTGTGGGTCGG - MB$
Phenylalanine	$HS - C_6 - CGACCGCGTTTCCCAAGAAAGCAAGTATTGGTTGGTCG - MB$

Table 5.1: The DNA sequences employed in this study.

5.6.1. We chose these sequences due to (a) their reliability in previous EAB studies, (b) the fact that the K_Ds of these aptamers overlap with the physiologically relevant ranges of their target molecules, and (c) that both yield stable, high signal gain EAB signals when interrogated using SWV.[11, 39]

Sensor fabrication. In vitro sensors were made by shrink wrapping gold wire with polyolefin and leaving 3 mm of the wire exposed. These sensors were made ahead of time and required no additional steps prior to electrochemical cleaning. We constructed our intravenous sensors as previously reported.[43] Briefly, they are made using gold, platinum and silver wires. These wires were individually insulated with polytetrafluoroethylene heat-shrink and bundled together in a staggered manner with the gold wire at the bottom, followed by the platinum and then the silver wire. The exposed lengths of each wire were 3 mm, 6 mm, and 1 cm, respectively. Once bundled together, the intravenous, three-electrode sensors were immersed overnight in household bleach (Clorox, sodium hypochlorite 7.5%) to chlorinate the silver electrode. The three electrodes were subsequently rinsed with Millipore water prior to electrochemical cleaning.

Prior to aptamer deposition, we electrochemically cleaned the gold working electrode in NaOH followed by roughening in H_2SO_4 using a CH1040C potentiostat. The cleaning

involved cycling the potential between -1.0 V and -2 V at 2 V/s 1000 times while the electrodes were immersed in 0.5 M NaOH.[48] This was followed by roughening in 0.5 M H_2SO_4 with the application of 20 ms pulses at 0 V and 2.2 V 32000 times as previously done to increase the electrode's microscopic surface area.[49] The electrodes were subsequently analyzed by cyclic voltammetry in 0.5 M H_2SO_4 (between 1.5 and -0.35 V at 1 V/s) to determine their electroactive surface area.[50]. Intravenous sensors that were to be used in vivo were inserted into a 20G catheter (Becton, Dickinson and Company) at this point.

To functionalize the working electrode we first reduced the disulfide bond in the stock alkanethiol-and-methylene-blue modified aptamer by combining 14 μL of 10 mM tris (2-carboxyethyl) phosphine with 2 μL of 100 μM DNA for 1 h in the dark. We then rinsed the electrochemically cleaned and roughened gold electrodes with Millipore water and immersed them for 1 h in 500 nM reduced DNA in PBS. The electrodes were then transferred to a 10 mM solution of 6-mercapto-1-hexanol in PBS and stored overnight before use.

Electrochemical measurements. All electrochemical measurements were carried out using a three-electrode setup. In our in vitro experiments, we employed a Ag/AgCl (saturated KCl, CH Instruments Inc.) reference electrode and a platinum wire counter electrode (CH Instruments Inc.). In vivo, we used a silver wire coated with silver chloride (as described above) as our reference electrode and a platinum wire counter electrode.

All electrochemical measurements were performed using an Autolab PGStat128N (Metrohm). The potentiostat was configured in "high stability mode" with a current range of ± 1 μA, which affects the filter characteristics. For FFT-EIS measurements, the multi-sin waveform was generated by a DG812 arbitrary waveform generator (Rigol Technologies) and fed into the potentiostat's external voltage input using a BNC connection. Our voltage waveform consisted of a superposition of 18 sine waves at logarithmically spaced frequencies ranging from 1 Hz to 1 kHz. The amplitude and phase of each sinusoidal oscillation were optimized for maximum signal-to-noise as discussed in the Supporting Information,[34, 37] and the summed waveform was scaled to have a peak-to-peak amplitude of 25 mV. The potentiostat's native software (NOVA) was used to set the DC bias – the formal potential of methylene blue, as measured by cyclic voltammetry – on top of the AC perturbation. Voltage and current were recorded at 70 kHz using an SDS1202X-E oscilloscope (Siglent Technologies). After each oscilloscope frame (1.4 s) was collected, the current and voltage data were transferred to the host computer, Fourier transformed, saved, and displayed on a GUI for real-time monitoring. Data recording and processing were controlled by a custom Python program. Further details on the chosen waveform and artifact correction are described in Supporting Information (Table 5.6.2, Figure 5.8, Figure 5.10).

We fit impedance spectra to the equivalent circuit model using MEISP 3.0 (Kumho Petrochemical Co. Ltd.) after each experiment. As discussed in the main text, the adsorption pseudocapacitance C_{ads} was modelled as a constant phase element, given by

Equation 5.5 (i is the imaginary number, ω is frequency, and n is the constant phase parameter). The parameter n was fixed at 0.84 for all fits to improve consistency in the fitted C_{ads} values.

$$Z_{C_{ads}}(\omega) = \frac{1}{C_{ads}(i\omega)^{n\times 90^\circ}} \tag{5.5}$$

In vivo measurements. All in vivo experiments were performed in male Sprague-Dawley rats (4-5 months old, Charles River Laboratories of Santa Cruz, CA). The rats weighed between 350-500 g and were pair-housed in a standard light cycle room (12:12 regular light cycle with lights on at 8AM). They were allowed ad libitum access to food and water and the Institutional Animal Care and Use Committee (IACUC) of the University of California at Santa Barbara approved our experimental protocol which adhered to the guidelines given by the NIH Guide for Care and Use of Laboratory Animals (8th edition, National Academy Press, 2011).

Prior to the measurement, we anesthetized the rats using 4% isofluorane in a Plexiglas anesthesia chamber. Anesthesia was then maintained via a nose cone for the entire duration of the experiment at a level of 2-2.5% isofluorane. The neck was shaved and bi-lateral incisions were made in order to surgically isolate the left and right jugular veins. After isolation, each vein was tied off using sterile 6-0 silk sutures (Fine Science Tools, Foster City, CA) A small incision was then made in each vein using spring-loaded microscissors that allowed us to insert the sensor-containing catheter into the right jugular vein and an infusion line into the left jugular vein. Both the sensor and drug infusion catheter were anchored in place using two sterile 6-0 silk sutures (Fine Science Tools, Foster City, CA).

Prior to the measurement, the wires in the sensor were adjusted such that the counter and working electrode were exposed outside of the 20G catheter into the vein as previously described43, and we infused 30 units of heparin through the infusion line immediately after insertion of the sensor and prior to any recordings. To intravenously dose the rats at 30 mg/kg we injected a precalculated volume of 0.05 M vancomycin solution using a syringe pump (KD Scientific) as previously described.[7]

5.6.2 Supplementary Figures

Frequency/ Hz	Normalized Amplitude	Phase/ °
1	1.00	4
3	0.64	-27
4	0.58	151
7	0.48	93
10	0.43	6
13	0.40	180
21	0.34	187
31	0.29	182
44	0.26	26
64	0.22	175
90	0.19	54
110	0.17	143
170	0.14	4
250	0.12	136
370	0.10	250
520	0.08	129
750	0.07	12
1000	0.06	164

Table 5.2: Frequencies, amplitudes, and phases used to construct the multi-frequency perturbation waveform.

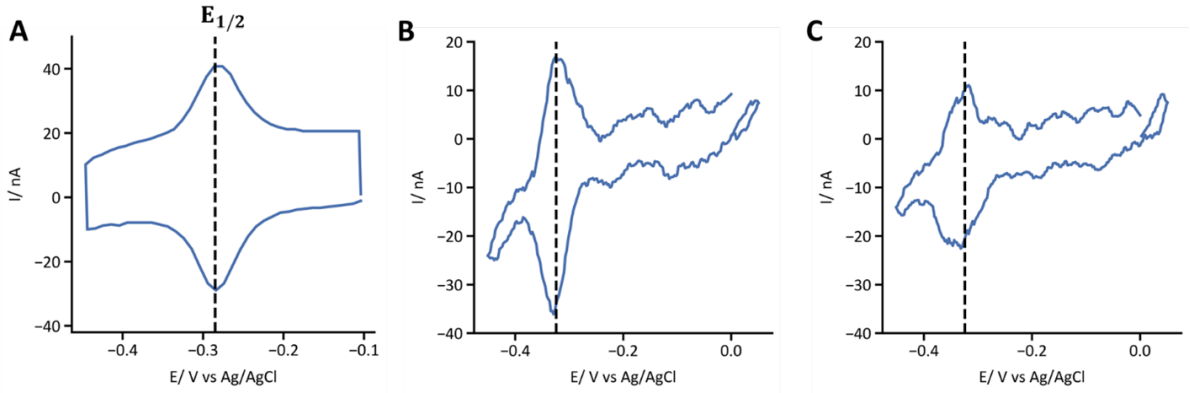

Figure 5.6: (A) Cyclic voltammogram recorded from a vancomycin-detecting EAB sensor in 1X PBS plus 2 mM $MgCl_2$. The voltammogram was recorded at 25°C with a scan rate of 100 mV/s. The half wave potential (the mean voltage between the reductive and oxidative peak potentials), $E_{1/2}$, was determined to be -285 mV versus Ag/AgCl. We recorded cyclic voltammograms prior to all EIS experiments in order to determine $E_{1/2}$, which was applied as the DC bias during EIS. (B) In vivo, $E_{1/2}$ (black dashed line) is -324 mV; this difference arises from the use of an anodized silver wire as the reference electrode rather than the fritted, single junction reference electrode used in vitro. (C) Shown is a cyclic voltammogram recorded in vivo at the end of a vancomycin dosing experiment. While the peak area is reduced (presumably due to monolayer loss),[44] $E_{1/2}$ remains at -324 mV.

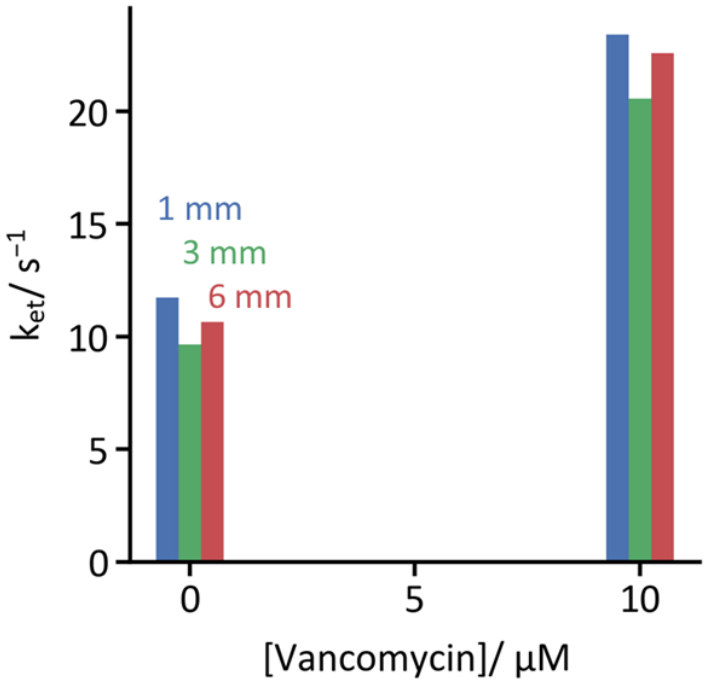

Figure 5.7: Electron transfer rate constants (k_{et}) recorded for vancomycin-sensing electrodes immersed in phosphate-buffered saline at 25 °C. The electrodes were fabricated with variable lengths of exposed gold wire (1, 3, and 6 mm) before they were subjected to the roughening and aptamer deposition procedures outlined in the experimental section. Both in the absence of vancomycin and when challenged with 10 μM of vancomycin, the recorded k_{et} values are tightly clustered and there is no systematic trend with electrode size, verifying the theoretical prediction that k_{et} is independent of electrode surface area. We note that these k_{et} values are lower than those presented in Figure 5.2D because this experiment was performed at 25 °C.[39]

We based our multi-sine waveform on the optimizations reported by Popkirov and Schindler,[37] and on our previous report.[35] A set of 18 logarithmically-spaced frequencies were chosen which were integer multiples of the fundamental frequency (1 Hz), avoiding any second harmonics. Phases were chosen in order to minimize constructive interference as previously described.[37] Amplitudes were set to create a similar current output at every frequency (i.e., $V(\omega) \propto |Z|(\omega)$). This strategy significantly increases signal-to-noise by applying higher voltage amplitudes at low frequencies, where (in an electrochemical cell) current is typically lower than at high frequencies. Using the frequencies f, amplitudes a, and phases ϕ listed (Table 5.6.2), the waveform was digitally synthesized as:

$$v(t) = \sum_j a_j \sin 2\pi f_j t + \phi_j \tag{5.6}$$

The optimized waveform used in this study is shown in the frequency domain in Figure 5.6A and in the time domain in Figure 5.6B. In the time domain, the peak-to-peak amplitude of the summed waveform was set to be 25 mV. The digital waveform was saved to a Rigol DG812 arbitrary waveform generator, which output the waveform at 100 kHz into the voltage input of the Autolab PGStat128N.

The low-pass current filter applied by the potentiostat may affect the measured impedance spectra, and should be corrected for. To do this, we measured the impedance spectrum of a 10 kΩ resistor (Figure 5.10A). While we expect a constant impedance of 10 kΩ and a constant phase of 0° for this resistor, we measure a phase shift that reaches 7° at 1 kHz. This is caused by the tail of the low-pass filter, which cannot be directly controlled on the potentiostat used in this study but which is affected by the choice of current range. Subsequently, impedance spectra were corrected using this reference spectrum as shown in Equations 5.7 and 5.8:

$$|Z| = \frac{|Z|_{measured}(\omega)}{|Z|_{ref}(\omega)} \tag{5.7}$$

$$\phi(\omega) = \phi_{measured}(\omega) - \phi_{ref}(\omega) \tag{5.8}$$

Re-recording the impedance spectrum of the same 10 kΩ resistor and applying this correction procedure yielded the expected 10 kΩ |Z|, 0° phase across the entire spectrum (Figure 5.10B).

$$k_{et} = k_{et,0} + (k_{et,max} - k_{et,0})\frac{[Phe]^n}{K_D^n + [Phe]^n} \tag{5.9}$$

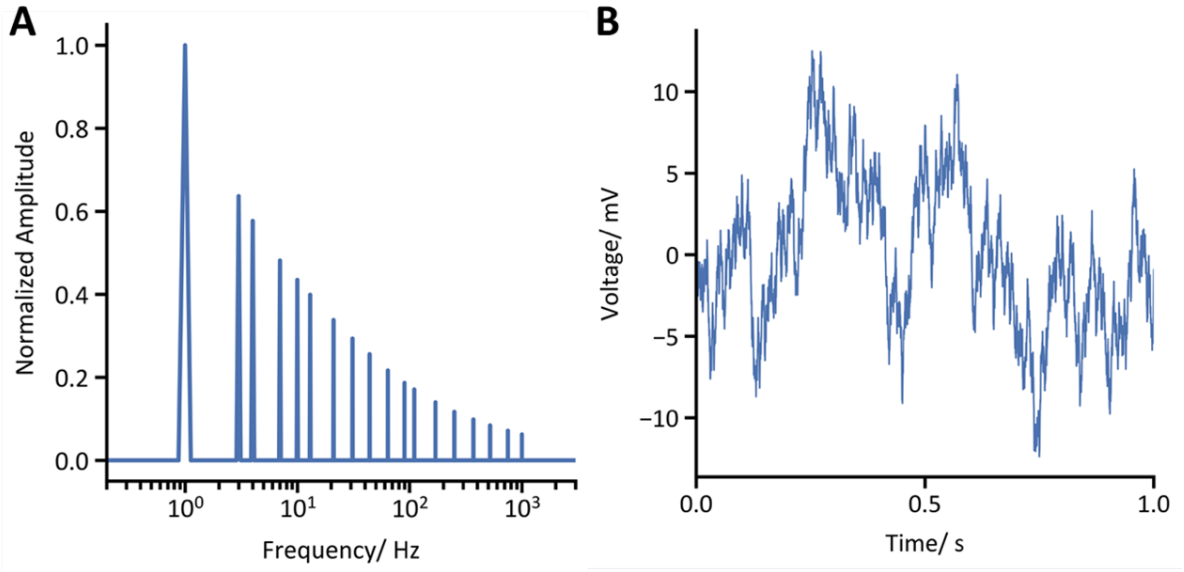

Figure 5.8: (A) Frequency- and (B) time-domain representations of the multi-sine EIS waveform we employed.

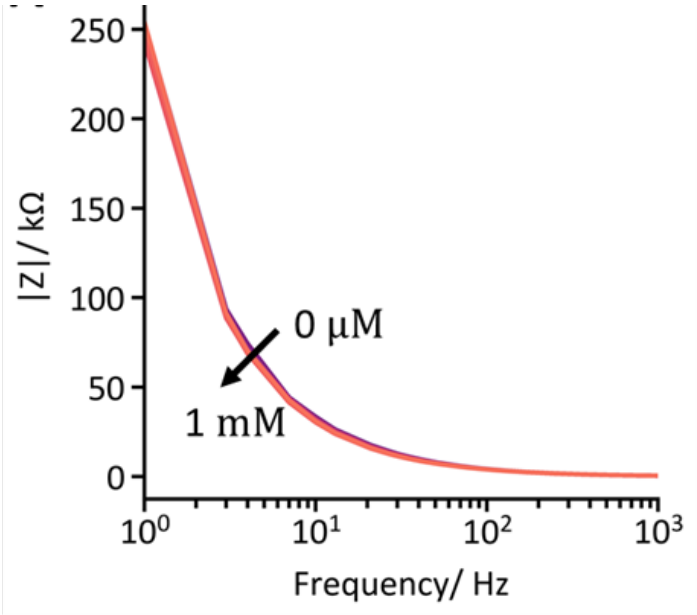

Figure 5.9: Bode |Z| plots collected from a vancomycin-detecting EAB immersed in whole bovine blood at 37°C and challenged with increasing concentrations of vancomycin (the same 18 concentrations as Figure 5.1D and 5.2B in the main text; here, all curves overlap). The modulus of the impedance does not change significantly at any frequency as a function of target concentration, despite the observed phase shifts (Figure 5.2A).

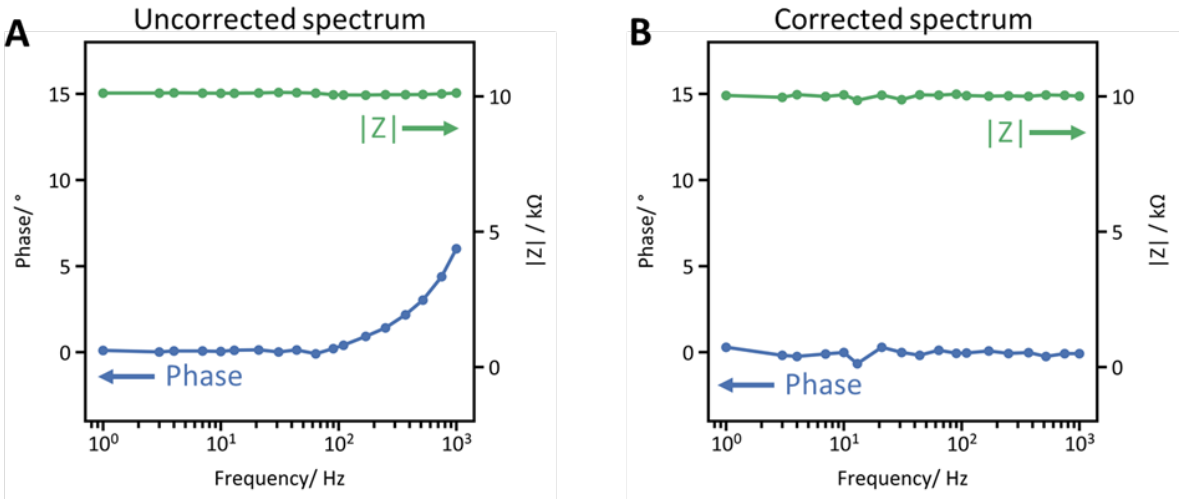

Figure 5.10: Phase (blue) and modulus (green) Bode plots of a 10 kΩ resistor. (A) The spectrum without filter corrections. |Z| is the expected 10 kΩ from 1 Hz to 1 kHz, but the phase is nonzero at high frequencies. (B) After correction, phase is zero across the frequency spectrum.

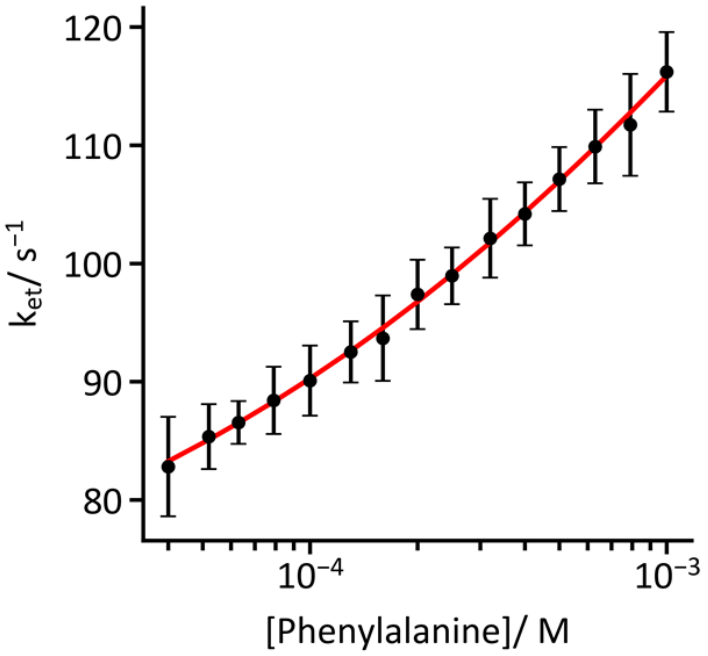

Figure 5.11: The binding curve of a phenylalanine-detecting EAB sensor interrogated using EIS can be used to determine phenylalanine concentration from k_{et}. To record this curve, we immersed the sensor in whole, freshly-collected rat's blood at 37°C. The endogenous concentration of phenylalanine in the blood (52 μM) was determined using a fluorescent assay kit. Aliquots of phenylalanine dissolved in PBS-BSA were then added to the blood to increase the phenylalanine concentration. Values of k_{et} (black points, error bars represent the standard deviation across four independently fabricated and tested sensors) fall on a Langmuir isotherm (Equation 5.9) where $k_{et,0}$ is the value of k_{et} in the absence of phenylalanine, $k_{et,max}$ is the value of k_{et} at saturating phenylalanine, K_D is the dissociation constant, and n is the Hill coefficient.[39] Fitting to this equation yielded $k_{et,0}$ = 62.9 s^{-1}, $k_{et,max}$ = 225.8 s^{-1}, K_D = 6.89 mM, and n = 0.38.

References

[1] G. T. Tucker, *Pharmaceutical Research* **2017**, *34*, 1539–1543.

[2] C. Fan, K. W. Plaxco, A. J. Heeger, *Proceedings of the National Academy of Sciences of the United States of America* **2003**, *100*, 9134–9137.

[3] Y. Xiao, A. A. Lubin, A. J. Heeger, K. W. Plaxco, *Angewandte Chemie - International Edition* **2005**, *44*, 5456–5459.

[4] Y. Xiao, B. D. Piorek, K. W. Plaxco, A. J. Heegert, *Journal of the American Chemical Society* **2005**, *127*, 17990–17991.

[5] A. A. Lubin, K. W. Plaxco, *Accounts of Chemical Research* **2010**, *43*, 496–505.

[6] L. R. Schoukroun-Barnes, F. C. Macazo, B. Gutierrez, J. Lottermoser, J. Liu, R. J. White, *Annual Review of Analytical Chemistry* **2016**, *9*, 163–181.

[7] N. Arroyo-Currás, J. Somerson, P. A. Vieira, K. L. Ploense, T. E. Kippin, K. W. Plaxco, *Proceedings of the National Academy of Sciences of the United States of America* **2017**, *114*, 645–650.

[8] P. Dauphin-Ducharme, K. Yang, N. Arroyo-Currás, K. L. Ploense, Y. Zhang, J. Gerson, M. Kurnik, T. E. Kippin, M. N. Stojanovic, K. W. Plaxco, *ACS Sensors* **2019**, *4*, 2832–2837.

[9] A. Idili, N. Arroyo-Currás, K. L. Ploense, A. T. Csordas, M. Kuwahara, T. E. Kippin, K. W. Plaxco, *Chemical Science* **2019**, *10*, 8164–8170.

[10] Y. Xie, S. Wu, Z. Chen, J. Jiang, J. Sun, *Analytica Chimica Acta* **2022**, *1207*, 339742.

[11] A. Idili, J. Gerson, T. Kippin, K. W. Plaxco, *Analytical Chemistry* **2021**, *93*, 4023–4032.

[12] B. Wang, C. Zhao, Z. Wang, K. A. Yang, X. Cheng, W. Liu, W. Yu, S. Lin, Y. Zhao, K. M. Cheung, H. Lin, H. Hojaiji, P. S. Weiss, M. N. Stojanović, A. J. Tomiyama, A. M. Andrews, S. Emaminejad, *Science Advances* **2022**, *8*, 1–16.

[13] C. Parolo, A. Idili, G. Ortega, A. Csordas, A. Hsu, N. Arroyo-Currás, Q. Yang, B. S. Ferguson, J. Wang, K. W. Plaxco, *ACS Sensors* **2020**, *5*, 1877–1881.

[14] A. Idili, C. Parolo, R. Alvarez-Diduk, A. Merkoçi, *ACS Sensors* **2021**, *6*, 3093–3101.

[15] M. A. Pellitero, S. D. Curtis, N. Arroyo-Currás, *ACS Sensors* **2021**, *6*, 1199–1207.

[16] N. Arroyo-Currás, P. Dauphin-Ducharme, G. Ortega, K. L. Ploense, T. E. Kippin, K. W. Plaxco, *ACS Sensors* **2018**, *3*, 360–366.

[17] S. Zhao, W. Yang, R. Y. Lai, *Biosensors and Bioelectronics* **2011**, *26*, 2442–2447.

[18] H. Li, P. Dauphin-Ducharme, G. Ortega, K. W. Plaxco, *Journal of the American Chemical Society* **2017**, *139*, 11207–11213.

[19] M. Santos-Cancel, R. A. Lazenby, R. J. White, *ACS Sensors* **2018**, *3*, 1203–1209.

[20] M. A. Pellitero, A. Shaver, N. Arroyo-Currás, *Journal of The Electrochemical Society* **2020**, *167*, 037529.

[21] B. S. Ferguson, D. A. Hoggarth, D. Maliniak, K. Ploense, R. J. White, N. Woodward, K. Hsieh, A. J. Bonham, M. Eisenstein, T. E. Kippin, K. W. Plaxco, H. T. Soh, *Science Translational Medicine* **2013**, *5*, DOI `10.1126/scitranslmed.3007095`.

[22] A. Chamorro-Garcia, J. Gerson, C. Flatebo, L. Fetter, A. M. Downs, N. Emmons, H. L. Ennis, N. Milosavić, K. Yang, M. Stojanovic, F. Ricci, T. E. Kippin, K. W. Plaxco, *ACS Sensors* **2023**, *8*, 150–157.

[23] T. Bertok, L. Lorencova, E. Chocholova, E. Jane, A. Vikartovska, P. Kasak, J. Tkac, *ChemElectroChem* **2019**, *6*, 989–1003.

[24] B. Y. Chang, S. M. Park, *Annual Review of Analytical Chemistry* **2010**, *3*, 207–229.

[25] N. T. Kemp, *IEEE Sensors Journal* **2021**, *21*, 22232–22245.

[26] J. Niroula, G. Premaratne, S. Krishnan, *Biosensors and Bioelectronics: X* **2022**, *10*, 100114.

[27] A. J. Bard, L. R. Faulkner, *Electrochemical Methods: Fundamentals and Applications*, 2nd ed., John Wiley & Sons, **2001**.

[28] S. M. Park, J. S. Yoo, *Analytical Chemistry* **2003**, *75*, 455–461.

[29] M. E. Orazem, B. Tribollet, *Electrochemical Impedance Spectroscopy*, John Wiley & Sons, Inc., **2008**.

[30] E. Rahbarimehr, H. P. Chao, Z. R. Churcher, S. Slavkovic, Y. A. Kaiyum, P. E. Johnson, P. Dauphin-Ducharme, *Analytical Chemistry* **2023**, *95*, 2229–2237.

[31] A. M. Downs, J. Gerson, K. L. Ploense, K. W. Plaxco, P. Dauphin-Ducharme, *Analytical Chemistry* **2020**, *92*, 14063–14068.

[32] G. S. Popkirov, R. N. Schindler, *Review of Scientific Instruments* **1992**, *63*, 5366–5372.

[33] G. S. Popkirov, R. N. Schindler, *Electrochimica Acta* **1993**, *38*, 861–867.

[34] J. E. Garland, C. M. Pettit, D. Roy, *Electrochimica Acta* **2004**, *49*, 2623–2635.

[35] B. Roehrich, E. Z. Liu, R. Silverstein, L. Sepunaru, *The Journal of Physical Chemistry Letters* **2021**, *12*, 9748–9753.

[36] A. Lasia, *Electrochemical Impedance Spectroscopy and its Applications*, Springer New York, **2014**.

[37] G. S. Popkirov, R. N. Schindler, *Review of Scientific Instruments* **1993**, *64*, 3111–3115.

[38] S. E. Creager, T. T. Wooster, *Analytical Chemistry* **1998**, *70*, 4257–4263.

[39] A. M. Downs, J. Gerson, K. K. Leung, K. M. Honeywell, T. Kippin, K. W. Plaxco, *Scientific Reports* **2022**, *12*, 1–10.

[40] J. Chung, L. Sepunaru, K. W. Plaxco, *ECS Sensors Plus* **2022**, *1*, 011604.

[41] E. Laviron, *Journal of Electroanalytical Chemistry* **1979**, *105*, 35–42.

[42] E. F. Douglass, P. F. Driscoll, D. Liu, N. A. Burnham, C. R. Lambert, W. G. McGimpsey, *Analytical Chemistry* **2008**, *80*, 7670–7677.

[43] K. K. Leung, J. Gerson, N. Emmons, B. Roehrich, E. Verrinder, L. C. Fetter, T. E. Kippin, K. W. Plaxco, *The Analyst* **2023**, *148*, 1562–1569.

[44] K. K. Leung, A. M. Downs, G. Ortega, M. Kurnik, K. W. Plaxco, *ACS Sensors* **2021**, *6*, 3340–3347.

[45] K. M. Cheung, K. A. Yang, N. Nakatsuka, C. Zhao, M. Ye, M. E. Jung, H. Yang, P. S. Weiss, M. N. Stojanović, A. M. Andrews, *ACS Sensors* **2019**, *4*, 3308–3317.

[46] S. Terrettaz, J. Cheng, C. J. Miller, R. D. Guiles, *Journal of the American Chemical Society* **1996**, *118*, 7857–7858.

[47] P. Dauphin-Ducharme, K. W. Plaxco, *Analytical Chemistry* **2016**, *88*, 11654–11662.

[48] L. M. Fischer, M. Tenje, A. R. Heiskanen, N. Masuda, J. Castillo, A. Bentien, J. Émneus, M. H. Jakobsen, A. Boisen, *Microelectronic Engineering* **2009**, *86*, 1282–1285.

[49] N. Arroyo-Currás, K. Scida, K. L. Ploense, T. E. Kippin, K. W. Plaxco, *Analytical Chemistry* **2017**, *89*, 12185–12191.

[50] S. Trasatti, O. A. Petrii, *Pure and Applied Chemistry* **1991**, *63*, 711–734.